Search for the Pentaquark via the Decay $P^0_{\bar{c}s} \to \phi\pi p$

THESIS SUBMITTED FOR THE DEGREE
"DOCTOR OF PHILOSOPHY"

by

Sharon May-Tal Beck

SUBMITTED TO THE SENATE OF TEL-AVIV UNIVERSITY

December 1997

This work was carried out under the supervision of

Prof. Daniel Ashery

Acknowledgements

I would like to take the opportunity and thank all the people who were with me along the way and to the people who helped me to reach graduation.

To Prof. Danny Ashery, for being my advisor for so many years. Under your supervision I became an experimental physicist. Most of all I would like to thank you for working with me like a friend, for replacing me in collaboration talks when I was not able to travel and for defending my work in the same passion that I felt for it. I greatly appreciate also the many hours you spent listening and correcting my "public" talks over and over again.

I would like to thank Prof. Zvi Lipkin who conceived the idea of the pentaquark and gave me the opportunity to search for it. I also thank him for many fruitful discussions during the analysis.

I would like to thank the members of the E791 collaboration at all times who made this project possible and with whom I had the pleasure to work. Special thanks to the spokesman Dr. Jeff Appel who gave me the feeling that I can consult with him at any time. Many thanks to the members of the "pentaquark committee" who refereed my analysis and by their endless comments made the results better established. Special thanks to Jean Slaughter who always helped me to find details about the software or the hardware of the experiment and made endless efforts to provide data for various checks. Very special thanks to Lucien Cremaldi and Simon Kwan especially for the warm words who supported me in some of the most difficult debates. Many special thanks to my friends at the collaboration: Sudeshna Banerjee who was a great friend during the lonely moments abroad, Tom Carter who always brought in a cheerful atmosphere, and Scott Radesztky that beside the philosophical conversations taught us how to cook with a wok. Special thanks to Lisa for always welcoming me with a smile and a hug and for successfully taking care of the "tape-flow" in Fermilab and to Israel.

I would like to thank the staff in the nuclear physics department of Tel-Aviv university, Riki Cohen and Moshe Zilca for their good spirit, for creating a pleasant atmosphere in the department and for taking care of all the details in the daily work. Thanks to the system managers of our computer system, Eli Comai and Michael Cordonsky. To the professors in the department many thanks for patiently hearing our (the students') complaints and trying their best to solve our problems. Many thanks to Haim, Gilad and Dror, my buddies and colleagues working on the master and doctorate projects, and to Ronit and Daphne that became my friends before they left the nuclear department and remained so. Many and very special thanks to my "room mates", Iris and Ruty, with whom I shared many moments of laughs, chats and changing moods.

I would like to thank my dear friends, Roni and Rami Ben-David, for the great hospitality and joint trips during my stay at Fermilab. Many special thanks and wishes to my best friends, Yael and Israel Mardor, being also my colleagues at the university, for continuing friendship along the years and for becoming our supportive neighbors, even if only for a single year.

Last, but not at all least, I would like to thank my family. To my parents who taught me that through putting enough efforts I could achieve anything. To my brother and sister and the extended family who helped many times babysitting while I had to finish some special projects. Very very special thanks to my dear husband for supporting me at all times and for putting my needs at the top of his priorities. And finally, most of all, I appreciate and love my sons, Lior and Raz, who brought a lot of joy to my life.

I dedicate this thesis to my beloved late grandmother. She was very important to me just as I and my way were important to her.

Abstract

This work reports results of the first search for the pentaquark, which is predicted to be a doublet of states: $P^0_{\bar{c}s} = |\bar{c}suud\rangle$ and $P^-_{\bar{c}s} = |\bar{c}sddu\rangle$. The color hyperfine interaction between their constituent quarks results in a maximal binding potential of 150 MeV. Calculations done using other models predict that the pentaquark is either bound or is a near-threshold resonance. A bound pentaquark would have a mass below 2.907 GeV/c^2 and its lifetime would be like that of other charm particles, of the order of 10^{-13} s. Crude estimates of the pentaquark production cross section predict values of the order of 1% of that of the D_s. Observation of the pentaquark is interesting for its unusual structure and would contribute to the understanding of QCD and the concept of confinement.

We searched for the pentaquark in the framework of Fermilab experiment E791, in which a π^- beam of 500 GeV/c interacted with a segmented nuclear target. The decay products of the produced hadrons were detected in a spectrometer capable of measuring production and decay vertices in great precision and of identifying charged hadrons. During the experiment 2×10^{10} events were recorded. In off-line analysis over 200,000 charmed particles were fully reconstructed.

We have searched for the pentaquark in its expected decay mode $P^0_{\bar{c}s} \rightarrow \phi\pi p$, where the ϕ subsequently decays to K^+K^-. We normalize the sensitivity of our search to $D_s^\pm \rightarrow \phi\pi^\pm$ decays which are similar enough that several systematic errors are common to both decay modes and cancel in the measured ratio of cross sections and branching fractions. The large number of events collected in the experiment made it possible to reach the desired sensitivity for the search.

Topological, kinematic, and other criteria were imposed to reject background and improve the statistical significance of a pentaquark signal in the $\phi\pi p$ mass spectrum. The optimal selection criteria have selected 24 $\phi\pi p$ candidates, out of which 11 with masses between 2.75 to 2.91 GeV/c^2, the region where the pentaquark is predicted to exist. Seven of these 11 events are grouped near 2.86 GeV/c^2. However, because of the low statistics in the final spectrum we conclude that there is no convincing evidence for the existence of the pentaquark in our data. We present a mass dependent upper limit at 90% confidence level for the ratio:

$$\frac{\sigma_P \cdot B_{P\rightarrow\phi\pi p}}{\sigma_{D_s} \cdot B_{D_s\rightarrow\phi\pi}},$$

where σ_P and σ_{D_s} are the cross sections for production of the pentaquark and the D_s, respectively, and B is the branching fraction for the listed decay modes. The upper limits are 0.022, 0.032, 0.025 and 0.046 for $M(P^0_{\bar{c}s}) = 2.75$, 2.79, 2.83 and 2.87 GeV/c^2, respectively, assuming a $P^0_{\bar{c}s}$ lifetime of 0.4 ps. The values of the upper-limit depend upon the pentaquark lifetime due to dependence of the acceptance on lifetime. For

$M(P^0_{\bar{c}s}) = 2.83$ GeV/c^2, the upper-limit is a rapidly decreasing function of lifetime, from an upper-limit close to 1 for 0.1 ps, to the value listed above for 0.4 ps, and remaining about the same for larger lifetime values.

The upper-limits are approaching the theoretically estimated ratio of production cross-sections if we assume the same branching fraction for the two decays and a pentaquark lifetime of 0.4 ps or greater. This search provides a good starting point for future searches in experiments that will collect larger samples of charm particles.

Contents

1 Theoretical Introduction **13**
1.1 Predictions of the pentaquark mass 14
1.1.1 The color-hyperfine interaction (CHI) 14
1.1.2 Other models 16
1.2 Characteristics of the pentaquark 21
1.3 Signature of the pentaquark 24
1.4 Production cross section of the pentaquark 25
1.4.1 Full production 25
1.4.2 Coalescence model 26
1.5 Summary: What kind of pentaquark do we search for ? 27

2 The Experiment **28**
2.1 Fermilab E791 experiment 29
2.1.1 Beam and target 31
2.1.2 Silicon Microstrip Detector (SMD) 32
2.1.3 Proportional Wire Chambers (PWCs) 34
2.1.4 Drift Chambers (DCs) 35
2.1.5 Magnets 36
2.1.6 Čerenkov counters 36
2.1.7 Calorimetry 44
2.1.8 Muon detection system 45
2.1.9 The trigger 46
2.1.10 Data Acquisition (DA) system 47
2.1.11 My own contribution to E791 49

3 Data Processing **51**
3.1 Reconstruction of tracks and vertices 51
3.1.1 Tracking 51
3.1.2 Vertexing 53
3.2 Data reduction 54
3.2.1 Analysis parameters 55
3.2.2 Filter requirements 57
3.2.3 Stripping processes 59

4 The Monte Carlo Simulation **61**
4.1 Generation of pentaquarks 62
4.2 Reliability of the MC 62
4.2.1 Study of x_F and p_T distributions 62
4.2.2 Distributions of decay variables 65

5 Analysis **76**
5.1 Method of analysis 76
5.2 The optimization procedure 78
5.3 Four-prong vertex definition cuts 80
5.4 Particle identification cuts 84
5.4.1 Kaon Čerenkov cut optimization 84
5.4.2 Proton Čerenkov cut optimization 88
5.4.3 Pion Čerenkov cut 89
5.5 The Pt2dk kinematical cut 89
5.6 General cleaning cuts 91
5.6.1 Secondary interactions 91
5.6.2 Ghost tracks 91
5.6.3 The "mirror gap" cut 93
5.6.4 Double entries 93
5.7 Summary: The chosen set of cuts, "UL96" 95

6 Misidentification Studies **97**
6.1 Misidentification of particles 98
6.1.1 A reflection as a peak 100
6.1.2 A flat reflection of a known particle 101
6.2 Misidentification of vertices 105
6.2.1 The subgroup of ϕs - Do they point back to the primary vertex? 105
6.2.2 The πp subgroup - Is it a $\Lambda \to \pi p$ decay? 106
6.2.3 Phase space and thresholds 107
6.3 Generic Monte Carlo 109
6.4 Summary: Understood background 114

7 Efficiencies of Selection Criteria and their Systematic Uncertainties **116**
7.1 Efficiencies 116
7.2 Systematic uncertainties 121
7.2.1 Vertex definition variables 123
7.2.2 Kinematical variable - the Pt2dk 124
7.2.3 Particle identification cuts 124
7.2.4 DIP(ϕ) 125
7.2.5 The effect of General cleaning and Misidentification cuts . . . 126
7.2.6 The effect of erroneous production characteristics 126
7.2.7 Summary 127

8 Results and Conclusions **129**
8.1 Final spectra of $\phi\pi p$ and $\phi\pi$ 129
8.2 Results 131
8.2.1 A mass dependent upper-limit for the decay $P^0_{\bar{c}s} \to \phi\pi p$ 131
8.2.2 Upper-limit dependence on the pentaquark lifetime 132
8.3 Summary 136

List of Figures

1.1 Binding potential of the H and $P_{\bar{c}s}$ corrected for the SU(3)$_{flavor}$ symmetry breaking. 15
1.2 Binding potential of the $P_{\bar{c}s}$ corrected for the SU(3)$_{flavor}$ symmetry breaking (the X-axis is $\delta = 1 - m_u/m_s$) and for the finite mass of the charm quark, using the parameter $\eta = m_u/m_c = 0.1$ and 0.3 16
1.3 A possible decay diagram of the pentaquark. The $\bar{c}$ quark decays to $\bar{s}$ while the other quarks are spectators. The $\bar{c}$ decay involves a W^- intermediate state which decays to $\bar{u}$ and d quarks. The quarks combine to form hadrons in the final state ($\pi\phi p$). 22
1.4 Cabibbo allowed and suppressed diagrams. Left: direct annihilation diagram. Right: exchange diagram. 23
1.5 Decay diagrams from the molecule-like parts of the pentaquark wave function. Two decay processes are shown. Left: from the term $\Psi_{D_s^- - p}$, where "D_s" decays to $\phi\pi$ and the proton remains stable. Right: from the term $\Psi_{D^- - \Sigma^+}$, where "D^-" decays to $K^0\rho^-$ with Σ^+ being a spectator. In the second step Σ^+ decays to $n\pi^+$. 25

2.1 $KK\pi$ invariant mass from $\phi\pi$ and $K^{0*}K$ decays. The spectrum shows the signals of D_s (right) and $D^\pm$ (left). 29
2.2 The Tagged Photon Spectrometer (TPS) used within Fermilab experiment 791. 30
2.3 E791 target configuration. One platinum foil followed by four carbon foils, separated by gaps of approximately 1.5 cm. 31
2.4 The E791 coordinate system showing the X, Y, U, V, W and W' views, with the beam directed into the page. 32
2.5 A schematic picture of a Silicon wafer. 33
2.6 Number of photons per unit length in Č1 and Č2 assuming the efficiency is one for wavelength between 1600 and 5000 Å and zero otherwise. 39
2.7 Mirror arrays in Č1 and Č2. 40
2.8 Probabilities assigned to tracks from simulated pentaquark decays, given the proton mass hypothesis. 42
2.9 Threshold curves showing the light response of the two Čerenkov counters to pion tracks passing through them (Č1 at the top and Č2 at the bottom). The X axis shows the track momenta in units of GeV/c, and the Y axis is the measured number of photoelectrons per track divided by the gains of the mirrors detecting the light from that track. The curves follow the expression $(1 - p_{th}^2/p^2)$. 43
2.10 Beam counters and the Interaction counter used in the trigger. 47
2.11 Schematics of data flow from electronic channels of the TPS, through FIFO buffers and event arranging buffers into 8 mm Exabyte tapes. . 50

3.1 Block diagram showing the data reduction process used to select pentaquark and D_s candidate events. The number of events selected by each stripping level is listed. 52
3.2 Scematics of an event with the production and decay of a pentaquark through the channel $P^0_{\bar{c}s} \rightarrow \phi\pi^{\mp}p^{\pm} \rightarrow K^+K^-\pi^{\mp}p^{\pm}$. 54

4.1 Distributions of x_F and p_T^2 at production from pentaquark and D_s MC simulations. The solid lines are the fit results of the functions $A(1-x_F)^n$ and $Be^{-bp_T^2}$. 63
4.2 Distributions of x_F for events accepted in the D_s mass peak from (a) MC and (b) data. The events in the D_s peak are defined by vertex cuts and by the D_s mass window, where the background is subtracted from the distributions. (c) The ratio between these x_F distributions, when the number of data events is normalized to the number of MC events. 64
4.3 D_s mass spectra from data with all cuts (top left), and with all cuts except for those that belong to the stated "family". 66
4.4 Distributions of C($K1$) for D_s signals from MC and data (left), and for the pentaquark signal from MC (right). 67
4.5 Distributions of χ^2_{sec}, for the D_s MC and data signals, for the pentaquark MC signal and for the $D^0 \rightarrow K\pi\pi\pi$ signal from data. 68
4.6 Ratios of χ^2_{sec} distributions from the data signal and from the normalized MC signal, for: (a) 3-prong decays of D_s, (b) 4-prong decays. The χ^2_{sec} distribution of the 4-prong decay $D^0 \rightarrow K\pi\pi\pi$ from data is divided by the normalized distribution for the pentaquark MC signal. (c) The double ratio of the distributions in (a) and (b). (d) The Yield(D_s *Signal*)/ε_{D_s} as a function of a "running" cut value on χ^2_{sec}. 69
4.7 Distributions of Pt2dk for: (a) the decay $D_s \rightarrow \phi\pi$ from Monte Carlo, (b) the same decay from data, (c) the decay $D^0 \rightarrow K\pi\pi\pi$ from Monte Carlo, (d) the same decay from data, (e) the decay $P^0_{\bar{c}s} \rightarrow \phi\pi p$ from Monte Carlo. 70
4.8 Momentum distributions of protons from data ($\Lambda \rightarrow \pi p$ sample) and from MC($P^0_{\bar{c}s}$). 71
4.9 (a) A distribution of C(p) that shows an ambiguity peak for protons from data having momenta between 21 to 40 GeV/c. (b) Momentum distribution of proton candidates in the K/p ambiguity peak from data. (c) Momentum distribution of proton candidates in the K/p ambiguity peak from MC. 72
4.10 A $\Lambda \rightarrow \pi p$ signal from data, for protons in the ambiguity peak having momenta between 21 to 40 GeV/c. 73

5.1 (a) The simulated $P^0_{\bar{c}s} \rightarrow \phi\pi p$ signal. (b) Invariant mass spectrum of $K\pi\pi\pi$ from data, showing the D^0 signal. (c) The simulated signal of $D_s \rightarrow \phi\pi \rightarrow K^+K^-\pi$. (d) Invariant mass spectrum of $\phi\pi p$ from data, showing events that are considered as background by the optimization procedure. (e) Invariant mass spectrum of $\phi\pi \rightarrow K^+K^-\pi$ from data. The right peak is the $D_s^{\pm}$ signal. The left peak arises from Cabibbo-suppressed $D^{\pm}$ decays. 79

5.2 (a) Maxrat$_i$ distributions from the $D^0 \to K\pi\pi\pi$ signal (solid line) and from its background (dashed line). (b) Maxrat$_i$ distributions from the MC signal of $P^0_{\bar{c}s} \to \phi\pi p \to KK\pi p$ (solid line) and from the $KK\pi p$ background spectrum (dashed line). The efficiencies as a function of the "running" cut value on MAXRAT$_i$ are shown in (c) for the D^0, and in (d) for the pentaquark. The sensitivities as a function of this "running" cut value are shown in (e) for the D^0 and in (f) for the pentaquark. The dotted lines on histograms (c) to (f) represent the chosen cut value: MAXRAT$_i$ < 0.45. 81
5.3 Results from a re-optimization process done for the χ^2_{sec}, DIP and RAT parameters, while requiring the additional MAXRAT$_i$ <0.45 cut. On the left: the efficiencies as a function of the "running" cut value on each parameter. On the right: the sensitivities as a function of these "running" cut values. The dashed lines represent the chosen cut values. 82
5.4 D^0 signals from data, plotted with the requirements of (a) "set 1", (b) "set 4" and (c) the combination: "set 1".or."set 4". The yield in the D^0 signal and its sensitivity are printed on each of the histograms. . . 83
5.5 Top: Momentum distributions of the two kaon candidate tracks in the ϕ sample. Bottom: the correlation between the momenta of the two kaon candidates. 85
5.6 Spectra of $\phi \to K^+K^-$ from the $\phi\pi p$ event sample, with different momentum dependent KID cuts, as described in the text. The number of events in the ϕ signal and its sensitivity are printed on each of the histograms. The statistical error on the sensitivity is printed too. . . 86
5.7 Spectra of K^+K^- invariant mass from (a) ϕ–filtered data and (b) $\phi\pi p$ event sample. The histograms are plotted with the optimized KID cut. The dotted lines on (b) demonstrate the ϕ mass cut applied to the $\phi\pi p$ data. 87
5.8 The efficiency (top) and sensitivity (bottom) plotted as a function of a "running" cut on the C(p) variable, where a momentum cut of 22<MOM(p)<75 GeV/c is required. The dotted line represent the chosen cut value. 88
5.9 The $K^+K^-\pi$ invariant mass spectrum, showing $D^\pm$ and $D_s^\pm$ signals, with various Pt2dk cuts. We note the disappearance of the $D^\pm$ peak for tight cuts. 90
5.10 Efficiencies (top) and sensitivities (bottom) plotted as a function of a "running" cut on Pt2dk. The solid and dashed lines represent optimization results using pentaquarks simulated with a mass of 2.83 and 2.75 GeV/c^2, respectively. 90
5.11 Distributions of $\sin(\theta_{ij})$ between each two tracks among the candidate K, K, π, p tracks, plotted with the pentaquark analyser cuts. 92
5.12 Distributions of $\sin(\theta_{ij})$ between each two tracks among the candidate tracks K, K, π, p, plotted with "set1" cuts. 92
5.13 Slopes of proton candidate tracks in the Y-direction. The top histogram is plotted with the pentaquark analyser cuts. The bottom histogram is plotted with the cuts of "set 2". 94

6.1 The $\phi\pi p$ invariant mass plotted from two thirds of E791 data, with the cuts of "set 1". 98

6.2 Ratios of track momenta to total pentaquark momentum, plotted with the pentaquark analyser cuts. 100
6.3 (a) M($K\pi\pi p$) or M($\pi K\pi p$) plotted versus M($\phi\pi p \rightarrow KK\pi p$), as a search for the reflected decay $\Sigma_c \rightarrow \Lambda_c\pi \rightarrow (pK\pi)\pi$. The K and p in the Λ_c candidate decay have opposite charges. (b) An invariant mass distribution of the track combinations ($K\pi\pi p$) or ($\pi K\pi p$), projected from (a). (c) M($KKKp$) plotted versus M($KK\pi p$). (d) One dimensional plot of M($KKKp$). All four histograms are plotted with the cuts of "set 1". 101
6.4 Histograms of M($K\pi\pi\pi$) of the four possible combinations, where $m(K)$ is assigned to different tracks in a cyclic permutation. The cuts are those in "set 1" with the KID and ϕID cuts relaxed. The dashed lines mark the D^0 mass, 1.865 GeV/c^2. 102
6.5 M($\phi\pi p \rightarrow KK\pi p$), plotted with "set 1" cuts for events that are also consistent with M($D^0 \rightarrow K\pi\pi\pi$) in all four possible combinations of tracks. The mass range taken for D^0 is: 1.84 - 1.89 GeV/c^2. 103
6.6 The $KK\pi\pi$ invariant mass, plotted with "set 1" cuts, but with Pt2dk > 0.2. The shaded area shows the events for which Pt2dk > 0.5. The dashed line marks the D^0 mass. 104
6.7 M($K^{\mp}\pi^{\pm}K^{\mp}p^{\pm}$) plotted as a search for the reflected decay $\Xi_c^0 \rightarrow K^{\mp}\pi^{\pm}K^{\mp}p^{\pm}$. The histogram is plotted with the cuts of "set 1", but with Pt2dk $>$ 0.2. The shaded area shows the events selected by the Pt2dk > 0.5 cut. The dashed line marks the Ξ_c mass. 104
6.8 The DIP(ϕ) distribution, calculated for ϕs from ϕ–filtered data that emerged from primary vertices in the target. 105
6.9 Distributions of DIP(ϕ), calculated for D_s signals from data (top) and MC (bottom). The histograms on the left are plotted with the D_s analyser cuts. The histograms on the right are plotted with the cuts of "set 1" and with an additional D_s mass window cut: 1.95 GeV/c^2 $<$ M($\phi\pi$) $<$ 1.99 GeV/c^2. 106
6.10 (a) The invariant mass of the πp subgroup of the $\phi\pi p$ candidates, plotted with the cuts of "set 1". (b) The $\phi\pi p$ invariant mass of the events, in which M(πp) is consistent with the Λ mass. 107
6.11 Phase-space distributions of M($D_s^{\pm} - p$) (solid line) and M($D^{\pm} - p$) (dashed line), where the $D_s^{\pm}$ and $D^{\pm}$ decay to $\phi\pi$ and the proton originates in the primary vertex. 108
6.12 The top plot is a two dimensional histogram of M($\phi\pi \rightarrow KK\pi$) versus M($\phi\pi p \rightarrow KK\pi p$), with loose 4-prong vertex definition cuts and the KID and ϕID cuts of "set 1". The dashed lines show the masses of $D^{\pm}$ and $D_s^{\pm}$. The bottom plot is the projection of the top histogram on the M($KK\pi$) scale. 109
6.13 Two dimensional plots of M(ϕp) versus M($\phi\pi p$). The top histogram shows the distribution with loose 4-prong vertex definition cuts and with the optimal KID cuts of "set 1" and the pID cuts of "set 2". The bottom histogram shows the same distribution, plotted with the cuts of "set 2". The dashed lines mark the Λ_c mass. 110

6.14 Invariant mass distributions of $\phi\pi \rightarrow KK\pi$ and $K\pi\pi\pi$, plotted from Generic MC (top) and from two thirds of E791 data (bottom). The histograms were plotted with those cuts of "set 1" common to the D_s and pentaquark analyses (left) or those common to the D^0 and pentaquark analyses (right). 111
6.15 Invariant mass distributions of $\phi\pi p$, plotted from generic MC (top) and two thirds of E791 data (bottom). The histograms are plotted with the requirements of "set 1" and further background reduction criteria, as described in the text. 112
6.16 An invariant mass distribution of $\pi\pi\pi\pi$ from two thirds of E791 data, plotted with 4-prong vertex definition cuts. The shaded area refers to the events selected by the rest of the cuts in "set 1". The dashed line marks the D^0 mass. 113
6.17 (a) M($\phi\pi p$), plotted from two thirds of E791 data, with the "UL96" cuts but before rejection of misidentified events. These background events (due to misidentification) are shaded. (b) M($\phi\pi p$) of events for which the invariant mass of $\phi\pi$ is consistent with the mass of $D_s^{\pm}$ or $D^{\pm}$. (c) M($\phi\pi p$) of misidentified $D^0 \rightarrow K\pi\pi\pi$ decays, or decays for which the πp invariant mass is consistent with the Λ mass. (d) M($\phi\pi p$) of events in which the ϕ points back to the primary vertex. 115

7.1 Distributions of Pt2dk, plotted from pentaquark Monte Carlo samples with M($P^0_{\bar{c}s}$) equals to 2.83 GeV/c^2 (solid line) and 2.75 GeV/c^2 (dashed line). 120
7.2 All $(K, 3\pi)$ invariant mass combinations calculated for the four tracks in the pentaquark decay vertex from Monte Carlo. The solid and dashed lines are for M($P^0_{\bar{c}s}$) equals to 2.83 and 2.75 GeV/c^2, respectively. The dotted-dashed lines mark the D^0 mass window of the "No D^0 candidates" cut: 1.84-1.89 GeV/c^2. 120
7.3 An invariant mass distribution of ($\phi_{wings}\pi p$), plotted with the optimal cuts of the pentaquark analysis ("UL96"). 121
7.4 (a) The ($\phi_{wings}\pi p$) invariant mass distribution, plotted with the optimal cuts ("UL96") when the criterion on the Pt2dk is released. (b) The events rejected by the Pt2dk>0.5 cut. (c) The ($\phi_{wings}\pi p$) invariant mass distribution, plotted with the cuts of "UL96", but when the criterion "no $D^0 \rightarrow K\pi\pi\pi$ candidates" is not required. (d) The events rejected by the "no $D^0 \rightarrow K\pi\pi\pi$ candidates" cut. 122
7.5 Distributions of χ^2_{sec} for 4- and 3-prong decays ((a) and (b), respectively). The solid and dashed lines in (a) represent the distributions from pentaquark MC and D^0 signal from data, respectively. The solid and dashed lines in (b) represent the distributions for D_s signals from MC and data, respectively. 123

8.1 (a) The $\phi\pi p$ invariant mass spectrum from the E791 data for the optimized selection criteria. Events in which the $\phi\pi$ invariant mass is consistent with the D$^{\pm}$ or $D_s^{\pm}$ masses are shaded. (b) Spectrum of $\phi_{wings}\pi p$ for the optimized selection criteria; see text for a full description. (c) The same spectrum as in (a), with a tighter proton identification criterion. (d) $\phi\pi$ invariant mass spectrum for the $D_s^{\pm}$ normalization sample. The left peak arises from Cabibbo-suppressed $D^{\pm}$ decays. 130

8.2 (a) Decay time distribution of all simulated pentaquarks with M($P^0_{\bar{c}s}$)=2.83 GeV/c^2. The solid line is the function fitted to the distribution: $\mathcal{F}(t) = C_0 \cdot e^{-t/\tau_0}$. The fitted parameters, C_0 (P1) and τ_0 (P2), and the χ^2 of the fit are listed in the top right corner of the histogram. (b) Decay time distribution of pentaquarks with M($P^0_{\bar{c}s}$)=2.83 GeV/c^2, plotted with the final cuts ("UL96"). 133
8.3 (a) The acceptance as a function of the pentaquark simulated lifetime. (b) The resulted upper-limit dependence upon pentaquark lifetime. The solid and dashed lines refer to a pentaquark mass of 2.83 and 2.75 GeV/c^2, respectively. 135

List of Tables

1.1 Major decay modes of the color-singlet components of the pentaquark and their branching fractions (B) for the on-shell particles. 23

2.1 Characteristics of target foils 32
2.2 Characteristics of SMD planes. In some of the SMD planes the spacing between the central strips is smaller than the spacing between the outer strips. The column "Strip pitch Inner ; Outer" lists the different spacings. 34
2.3 Characteristics of PWC planes 35
2.4 Characteristics of DC planes 36
2.5 Characteristics of the magnets 36
2.6 Characteristics of the two Čerenkov counters. 37
2.7 Threshold momenta for e, μ, π, K and p in the Čerenkov counters. . . 38
2.8 The light response of Č1 and Č2 to charged hadrons in momentum bins of the particles. The + or − signs refer to whether light is emitted or not, respectively. 38
2.9 Characteristics of the SLIC 44
2.10 Characteristics of the Hadrometer. 45
2.11 Characteristics of the steel wall placed downstream of the Hadrometer. 45
2.12 Characteristics of the X and Y muon walls. 46
2.13 Characteristics of the scintillating paddles of the trigger system. . . . 46

3.1 Resolutions of primary vertices reconstructed from $D^{\pm}$ data and Monte-Carlo simulation, in the Platinum and four Carbon targets. 53
3.2 Selection criteria required by the pentaquark and D_s filter and strip routines. C($K1, K2$) stands for a cut on the Čerenkov probability assigned to each of the two kaon candidate tracks. C($K1$ or $K2$) refers to a cut applied either to the first or to the second kaon. C($K1 \bullet K2$) stands for the product of the Čerenkov probabilities assigned to the two kaons. 59

4.1 Number of pentaquark and D_s generated events and the number of events selected by the Filter and Strip stages of analysis. 62
4.2 Efficiencies and their errors in brackets calculated for different cuts on C(p) in four momentum regions. The numbers listed in the first line are the number of events in the signal with the requirement of C(p)>0.038. The three numbers in each box are related to Λs decaying within 20cm from the targets, in farther location, and to pentaquarks in the MC signal. 74

5.1 Efficiencies (upper raws) and sensitivities (lower raws), calculated in momentum bins of $K2$. For the "Analyser cuts" line only the sensitivity is listed. 84
5.2 Values of parameters related to two combinations of four tracks (entries) in two events. All four entries were selected by the optimal set of selection criteria ("UL96"). The variables characterizing the pion candidate track are listed in the top part of the table, and those characterizing the four-prong decay vertex are listed in its bottom part. . 95
5.3 Selection criteria applied in the pentaquark and D_s analyses. C($K1, K2$) stands for the cuts applied to the Čerenkov probabilities of each of the kaons. "set 1" includes the originally optimized selection criteria. "Set 2" and "set 3" are identical to "set 1" except for the additional requirement of proton ID cut. "Set 4" is a result of the re-optimization process, and the "UL96 set" is the final set used. It results from combining "set 1" and "set 4" and includes all general cleaning and misidentification cuts. 96

6.1 Ratios between the yield in $D^{\pm}$, $D_s^{\pm}$ and D^0 signals from Generic MC and two thirds of E791 data. 112

7.1 The reduction factors caused by each of the "UL96" cuts, calculated as the ratio between the yield in a peak after a cut is applied and the yield in the peak produced by the analyser. These reduction factors were calculated using signals of the decays $D_s^{\pm} \to \phi\pi^{\pm} \to K^+K^-\pi^{\pm}$ from Monte Carlo and data, and the Monte Carlo signal of the decay $P^0_{\bar{c}s} \to \phi\pi p \to K^+K^-\pi p$. The numbers in parentheses are the statistical errors. 117
7.2 Efficiencies of the optimal cuts ("UL96" set), calculated from the Monte Carlo samples of pentaquarks with M($P^0_{\bar{c}s}$)=2.75 and 2.83 GeV/c^2, and from the Monte Carlo sample of D_s. 118
7.3 Ratios between efficiencies calculated from the two pentaquark Monte Carlo samples, with M($P^0_{\bar{c}s}$)=2.83 and 2.75 GeV/c^2, for the optimal cut values of the "UL96" set. The numbers is parentheses are the statistical errors. 119
7.4 Cut values applied to C($K1, K2$) together with the difference between the ratio $R_1 = \frac{\varepsilon_{P^0}}{\varepsilon_{D_s}}$ and the value of this ratio for the optimal cut value: C($K1, K2$) > 0.2 (R_0). 125
7.5 Systematic uncertainties in the ratio of pentaquark and D_s efficiencies. The total systematic uncertainty is taken as the square root of the quadratic sum of these contributions. The maximal possible systematic effects expected due to the general cleaning and misidentification cuts are listed in the lower part of the table. 128

8.1 Values of $UL(N_{P\to\phi\pi p})$, ratio of efficiencies for $P \to \phi\pi p$ and $D_s \to \phi\pi$, and $N_{D_s\to\phi\pi}$ used to calculate the upper-limit on the ratio of cross section times branching fraction for the decays $P^0 \to \phi\pi p$ and $D_s^{\pm} \to \phi\pi^{\pm}$, as defined in Eq. 8.2. The relative error σ and the correction factor f_{SYS} are listed too. Four values of pentaquark mass are used. The pentaquark lifetime used to calculate efficiencies is 0.4 ps. . . . 132

Chapter 1

Theoretical Introduction

The spectrum of observed hadrons fits into multiplets of two- and three-quark states. The mass differences within these multiplets can be explained by effective quark masses and the color-hyperfine interaction (CHI) in the QCD Hamiltonian [1]. Calculations done using the CHI predict the existence of particles made of more than three quarks. Jaffe [2] predicted the existence of the H dibaryon, $H = |uuddss\rangle$, and extensive efforts have been made to find it experimentally [3]. Lipkin [4] and Gignoux *et al.* [5] have proposed that a doublet of states, the $P^0_{\bar{c}s} = |\bar{c}suud\rangle$ and the $P^-_{\bar{c}s} = |\bar{c}sddu\rangle$, and their charge conjugate states, may exist and be stable against strong decays. These were named pentaquarks ("$P_{\bar{c}s}$"). The predictions made using CHI interaction predict a pentaquark binding potential which varies from 150 MeV/c^2 to few tens of MeV/c^2, depending on how SU(3)$_{flavor}$ symmetry breaking and the mass of the charm antiquark are taken into account [5]. Contributions to the binding energy from other components of the Hamiltonian are even more model dependent. Calculations done using bag models [6, 7], an Instanton model [8], and Skyrme models [9, 10] conclude that, depending upon the choice of parameters, the pentaquark is bound or is a near-threshold resonance.

Observation of the pentaquark is interesting for its unusual structure and would have far-reaching consequences for quantum chromo-dynamics (QCD) and for the concept of confinement. This work describes in detail the first published search for the pentaquark and report its results.

In this chapter I present the pentaquark. Section 1.1 describes the pentaquark mass predictions by different models. Section 1.2 discusses the structure of the pentaquark and the resulting possible decay modes and lifetime. Section 1.4 describes possible mechanisms for pentaquark production and show rough estimates of the cross section to produce the pentaquark.

1.1 Predictions of the pentaquark mass

1.1.1 The color-hyperfine interaction (CHI)

Color-hyperfine interaction (CHI) is a short range interaction. It describes one gluon exchange between quarks as given by the expression:

$$V_{CHI} = -\alpha \sum_{i<j} \lambda_i \lambda_j \vec{\sigma}_i \vec{\sigma}_j / m_i m_j \ , \tag{1.1}$$

where α measures the strength of the interaction, λ is a color matrix of an interacting quark, σ is its Pauli spin matrix and m_i are the constituent quark masses in a non-relativistic quark model. The sum in the expression is over all possible pairs of interacting quarks. The differences in hadron masses within the multiplets are well reproduced by the CHI splitting [1]. When α is small enough at near-separation of quarks in order for QCD hyperfine splitting to be relevant, and the only symmetry breaking arises from the different quark masses, the hadron masses can be expressed as [11]:

$$\begin{aligned} m(\ mesons:\ |q_1\bar{q}_2\rangle\ ) &= m_1 + m_2 + \left[a\frac{\vec{\sigma_1}\cdot\vec{\sigma_2}}{m_1 m_2}\right] \\ m(\ baryons:\ |q_1 q_2 q_3\rangle\ ) &= m_1 + m_2 + m_3 + \left[\frac{a'}{2}\sum_{i<j}\frac{\vec{\sigma_i}\cdot\vec{\sigma_j}}{m_i m_j}\right], \end{aligned} \tag{1.2}$$

where m_i are the constituent quark masses, and a and a' are constants which include the appropriate color factors (-4/3 for mesons and -2/3 for baryons), and the strength of the interaction α.

In the $SU(3)_{flavor}$ symmetry limit, and under the assumption that the $\bar{c}$ quark does not contribute due to its large mass, the expression in Eq. 1.1 reduces to [2]:

$$V_{CHI} \cong (\alpha/m^2)[4N_q + \frac{2}{3}S(S+1) - \frac{1}{4}C_6^{CS} + \frac{1}{4}C_3^C], \tag{1.3}$$

where m is the quark mass assuming $SU(3)_{flavor}$ symmetry ($m(u) = m(d) = m(s) \simeq$ 336 MeV/c^2), N_q is the number of active quarks, S is the total spin, and C_6^{CS} and C_3^C are eigenvalues of Casimir operators of SU(6)$_{Color-Spin}$ and SU(3)$_{color}$, respectively. The coefficient α is calculated from the $\Delta - N$ mass splitting of 300 MeV which is attributed to the CHI. Using for the Δ: $N_q = 3$, $S = \frac{3}{2}$, $C_6^{CS} = 42$, $C_3^C = 0$, and for the nucleon: $N_q = 3$, $S = \frac{1}{2}$, $C_6^{CS} = 66$, $C_3^C = 0$, the resulting splitting is $m(\Delta) - m(N) = 8(\alpha/m^2)$. The binding potential of a system is given approximately by the difference between the expectation value of V_{CHI} acting on this system and on the lightest color-singlet combination of quarks into which it can be decomposed. In the case of the H this lightest combination is a $(\Lambda - \Lambda)$ system and for the $P_{\bar{c}s}$ it is the $(D_s^- - N)$ system (see sec. 1.2). Using for the H: $N_q = 6$, $S = 0$, $C_6^{CS} = 144$, $C_3^C = 0$, and for each Λ: $N_q = 3$, $S = \frac{1}{2}$, $C_6^{CS} = 66$, $C_3^C = 0$, the resulting mass splitting is $m(\Lambda - \Lambda) - m(H) = 4(\alpha/m^2)$, half of the $\Delta - N$ mass splitting, i.e. about 150 MeV. Similarly, in the case of the pentaquark, if the $\bar{c}$ contribution is neglected, and the state considered for the four remaining quarks is of spin zero and a color

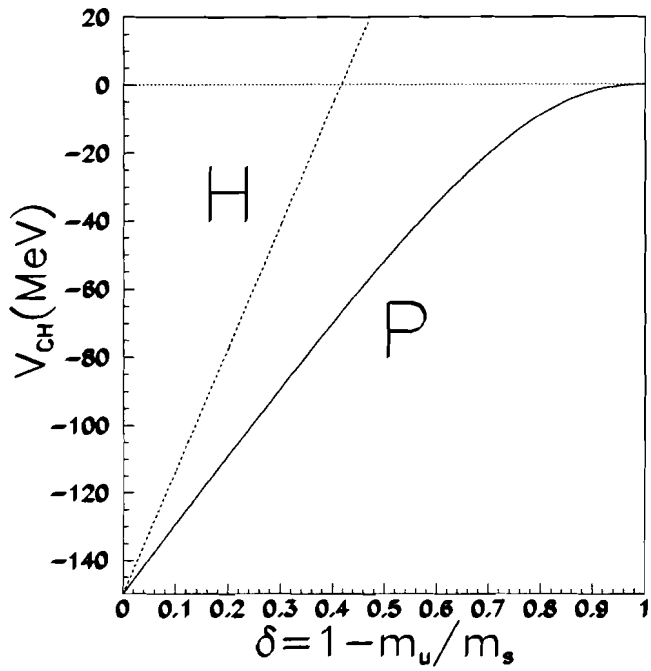

Figure 1.1: Binding potential of the H and $P_{\bar{c}s}$ corrected for the SU(3)$_{flavor}$ symmetry breaking.

triplet, then $N_q = 4$, $S = 0$, $C_6^{CS} = \frac{304}{3}$, $C_3^C = \frac{16}{3}$, yielding $V_{CHI} = -8(\alpha/m^2)$. As for the $D_s - N$ system only the nucleon has a CHI (because the $\bar{c}$ does not contribute to the interaction within the D_s) and it is $-4(\alpha/m^2)$ as discussed above. The mass splitting between the pentaquark and the threshold $D_s - N$ system is therefore $m(D_s - N) - m(P_{\bar{c}s}) = 4(\alpha/m^2)$, the same as for the H particle, ~ 150 MeV. These calculations were corrected for the SU(3)$_{flavor}$ symmetry breaking and for the finite mass of the $\bar{c}$ quark [5]. The results are shown in Figs. 1.1 and 1.2. The parameters $\delta = 1 - m_u/m_s$ and $\eta = m_u/m_c$ express the sensitivity of the calculation to the masses of the s and c quarks being different from the masses of the light u and d quarks. It can be seen that the $P_{\bar{c}s}$ retains always a larger binding potential than the H and for reasonable values of the two parameters ($\delta \leq 0.3$ and $\eta \sim 0.2$) the binding potential can be several tens of MeV.

However, the V_{CHI} potential is only a part of the Hamiltonian which describes the binding energy of a particle. The standard non-relativistic quark Hamiltonian is given by [6]:

$$H = \sum_i \left(\frac{p_i^2}{2m_i}\right) - \frac{3}{16}\sum_{i<j} \lambda_i \lambda_j V_c(r_{ij}) - \frac{3}{16}\sum_{i<j} \frac{\vec{\sigma}_i \cdot \vec{\sigma}_j \lambda_i \lambda_j}{m_i m_j} V_{ss}(r_{ij}), \qquad (1.4)$$

where the first term represents the kinetic energy, the second stands for the color-electric central potential and the third is the spin-spin interaction which includes the

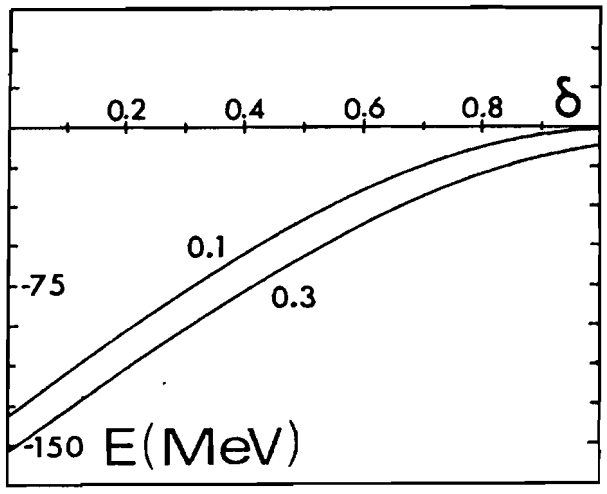

Figure 1.2: Binding potential of the $P_{\bar{c}s}$ corrected for the $SU(3)_{flavor}$ symmetry breaking (the X-axis is $\delta = 1 - m_u/m_s$) and for the finite mass of the charm quark, using the parameter $\eta = m_u/m_c = 0.1$ and 0.3

CHI potential. The massive c quark makes the kinetic energy term much smaller in the pentaquark than in the H if the same form factor (internal momentum) is assumed. The complete mass evaluation is more model dependent. Over 20 calculations of the H mass were performed using a variety of models [12]. Most of the results cluster around the $\Lambda - \Lambda$ threshold, with exceptions of very deep binding of over 1 GeV/c^2 or a state unbound by 0.5 GeV/c^2. This indicates that most likely the H is either bound or unbound by a few MeV/c^2. Much fewer model calculations were done for the pentaquark. They are described in the following section.

1.1.2 Other models

Bag model

The bag-model picture adopted by Zouzou and Richard [7] has quarks moving inside a cavity, and chromo-electric as well as chromo-magnetic interaction between them. In the original MIT bag-model ground state mesons and baryons are described with u, d, s quarks in a static cavity. The quark wave functions are given by the free Dirac equation inside a sphere of radius R. For a given radius, the hadron energy,

$$E(R) = \frac{4}{3}\pi B R^3 + \sum_i \omega_i - \frac{Z_0}{R} + \delta E_e + \delta E_m, \tag{1.5}$$

combines the volume energy (first term), the kinetic energy (second term), the zero-point energy which includes other corrections in an effective way (third term), and chromo- electric and magnetic corrections (fourth and fifth terms). The zero point energy ($\frac{Z_0}{R}$) is an empirical correction needed for simultaneously fitting the meson and baryon masses, but it prevents proliferation of multiquark states in the bag model. The chromo-electric term is:

$$\delta E_e = \frac{\alpha_c}{2R} \sum_{i,j} \lambda_i \cdot \lambda_j f_{i,j} \tag{1.6}$$

where $f_{i,j}$ is the color-electric strength, calculated from quark densities. The chromo-magnetic term is:

$$\delta E_m = -\frac{3\alpha_c}{R} \sum_{i<j} \vec{\sigma_i} \cdot \vec{\sigma_j} \lambda_i \cdot \lambda_j g_{i,j} \tag{1.7}$$

where the strength $g_{i,j}$ is expressed in terms of magnetic moments and densities. As a result of non-linear boundary conditions, the bag energy is minimized with respect to R, and the results correspond to the following set of parameters and masses:

$$\begin{gathered} B^{1/4} = 0.145\ GeV, \quad Z_0 = 1.81, \quad \alpha_c = 0.55, \\ m_{u,d} = 0, \quad m_s = 0.279\ GeV. \end{gathered} \tag{1.8}$$

In reference [7] the MIT bag-model was adopted to include heavy quarks, and was proposed as "adiabatic" bag-model. For fixed interquark separations, the shape and size of the bag were adjusted to minimize the energy of the gluon field. This minimum was used as the interquark potential and was inserted into the Schrödinger equation. In the case of hadrons with one heavy quark it was assumed that the heavy quark stayed at the center of the bag. The parameter α_c was defined as a running coupling constant depending on the radius R of the bag:

$$\alpha_c = \frac{\pi}{18 ln(1 + 1/(\Lambda R))}. \tag{1.9}$$

The radius R was adjusted in the approximation where only the volume, kinetic and zero-point energies were included. The chromo-electric and -magnetic terms, modified to include the heavy quark, were then computed with this radius already fixed. A reasonable description of the spectrum of ordinary, charm and beauty hadrons was achieved with the following set of parameters (Table 1. in ref. [7]):

$$\begin{gathered} B^{1/4} = 0.1383\ GeV, \quad \Lambda = 0.400\ GeV, \quad Z_0 = 0.574, \\ \bar{x}_{u,d} = x_{u,d} = 2.042, \quad \bar{x}_s = 2.3, \\ m_{u,d} = 0, \quad m_s = 0.273\ GeV, \quad m_c = 2.004\ GeV, \quad m_b = 5.360\ GeV \end{gathered} \tag{1.10}$$

with x/R being the wave number of a quark. The agreement between calculated and measured masses of hadrons demonstrates that the model does not overestimate the strength of the magnetic forces, which are a potential source of collective binding.

The calculation of $|\bar{Q}qqqq\rangle$ states was done in the same model. Details of the chromo-electric and -magnetic terms, and the spin-color wave functions can be found in reference [7]. The study was made on pentaquarks: $|\bar{Q}udss\rangle$ and $|\bar{Q}suud\rangle$ and their charge conjugate states, with total spin and parity $J^p = \frac{1}{2}^-$. The results are that the pentaquark is bound in the limit where $m(\bar{Q}) = \infty$ and $m_s = m_{u,d}$, but the stability does not survive the heavy quark mass being finite and the $SU(3)_{flavor}$ symmetry breaking. With these conditions the pentaquark is predicted to be a resonance, with a mass of about 8 MeV above the threshold.

In other non-relativistic bag-model calculation, authors tried to extrapolate the quark-antiquark potential of mesons towards the multiquark sector [6]. An interesting result

of these calculations is that the short-range 2-body correlation is generally smaller in a multiquark system than in ordinary hadrons. This tends to reduce the binding of multiquark states.

Instantons model

It is possible to learn about the ground state of a quantum mechanical system by solving the corresponding classical problem in the Euclidean space (where $-x_\mu x_\mu = x_4^2 + \vec{x}^2$) [13]. Since it is not known how to solve directly for the true ground state of quantum chromodynamics (QCD), the classical chromodynamics equations are solved in Euclidean space with energy $E = 0$. These are called the *instanton* solutions. Their presence reveals the degeneracies and accompanying tunneling in the real-world QCD. The appropriate superposition of these states yields the true structure of the ground state - called the "θ-vacuum".

The H and pentaquark binding energies are significantly reduced by the instanton effect [8]. The coupling between instantons and flavor-singlet groups of light quarks induces an effective interaction between quarks, denoted as V_{III}, which is known to give a main contribution to the large $\eta - \eta'$ mass difference. V_{III} gives an overall shift in the $S-$wave baryon mass spectrum when the model parameters are readjusted to give the observed hyperfine splitting. At the same time V_{III} reduces the value of α_s to about (60-70)% of its original value, which is a highly welcome feature since the best fit value of α_s obtained in the CHI of valence-quarks is too large for perturbative treatment. V_{III} generates a longer range attraction and a short range 3-body repulsion in multihadron systems (if the three quarks are in color singlet). The quark-quark interaction is represented by three terms:

$$OGE + V_{III} + confinement \quad potential. \tag{1.11}$$

These represent the perturbative effects of the gluon field (OGE), the short-range nonperturbative effects (V_{III}), and the long-range nonperturbative effects. The terms that give the mass splitting are the color-hyperfine interaction part of OGE and V_{III}. V_{III} consists of 2- and 3-body parts (V_{III2} and V_{III3}) and is operative only in flavor-singlet quark states.

In order to take into account the threshold energy properly, an extra flavor-dependent effective potential between $s - s$ and $s - c$ quarks was introduced in ref. [8]:

$$V_{th} = \sum_{i<j} \frac{1}{4} \varsigma_{ij} (\lambda_i \cdot \lambda_j) \delta(\vec{r}_{ij}), \tag{1.12}$$

where $\varsigma_{ij} \equiv \frac{m_i}{m_j}$. The total quark Hamiltonian becomes:

$$H = K + (1-p)V_{OGE} + pV_{III} + V_{th}, \tag{1.13}$$

where K is the kinetic energy and the parameter p specifies the relative importance of V_{III} in the splitting. For V_{III} - the interaction between light quarks only was considered since it originated from the zero energy mode of massless quarks. For CHI - the interaction between u and $\bar{c}$ quarks was also considered as it had been the one which gave rise to the large $D - D^*$ mass difference. The effect of confinement was simulated by using gaussian ground state configurations with size parameter $b = 0.5$

fm. The corresponding quark core was rather strong. The overall strength of OGE and V_{III2} was chosen as to give the $\Delta - N$ mass difference, where V_{III2} accounted for 40% of this splitting. The various parameters in the Hamiltonian were adjusted to fit the mass splitting of other known particles.

The allowed symmetries in color, spin and flavor of the u, d, s quarks ($[21]_c \times [21]_s \times [1^3]_f$) imply that the three body repulsion in the pentaquark is one third of that in H. The originally predicted pentaquark [4, 5] has its four light quarks with spin zero and $[211]_f$ symmetry. The original H was predicted to have spin zero and $[222]_f$ symmetry [2]. These two states satisfy the "flavour antisymmetry" hypothesis, by which quark systems characterized by the maximum possible antisymmetry of quark flavors are the most strongly bound. For these two states, the binding energy predicted by the instanton model is -44 or -28 MeV for the pentaquark, and -35 or -45 MeV for the H, where the two values refer to the parameter $p = 0$ or $p = 0.4$, respectively. Pentaquark and H states with other symmetries in flavor are predicted to be unbound by up to 276 MeV and 342 MeV, respectively. The pentaquark state with $[211]_f$ symmetry is not a good energy eigenstate though. The bound state in this model is mainly a mixture of $[211]_f$ and $[22]_f$ states.

Effects of quark clustering inside the H and the pentaquark were studied also since energetics of various cluster channels could exhibit different symmetry breaking effects. A schematic quark-cluster model (QCM) was employed, where meson exchange potential between the clusters of quarks was taken into account. It included only a spin-flavor-independent attraction, $V_\sigma(R)$. For the pentaquark the strength $V_\sigma(R)$ has been taken to be 2/3 of that of $N - N$ system as this is the ratio between qq and $q\bar{Q}$ clusters in the two systems. The resulted binding energy of the pentaquark was small - few MeV, almost independent of the parameter p. The calculation of binding energy, however, involved considerable uncertainties since neither the meson contribution nor V_{th} were well known. Since the intermediate attraction for $p > 0$ was overestimated in the model, the conclusion was made that the pentaquark is not likely to be bound.

As for the H - two bound states are expected. Using the same model, the original H state with $[222]_f$ symmetry is predicted to be bound by 43 MeV at $p = 0$. The other state, with $[42]_f$ symmetry is only weakly bound. Around $p = 0.4$ the binding energies of the two states are almost degenerate. When the strength of the meson exchange potential is readjusted as a function of p to reproduce the two-nucleon scattering data, the H particle is shifted from a bound state to a low-lying resonance state for $p > 0.25$.

Skyrme model

Many properties of the large N_c limit of QCD (where N_c is the number of colors) are satisfied by the meson sector of the sigma model [13]. In a simple case of only two flavors, where the underlying symmetry is $SU(2)_L \times SU(2)_R$, the Langrangian of a non-linear sigma model for $m_\pi = 0$ is:

$$\mathcal{L}_0 = \frac{f_\pi^2}{4} Tr[(\partial_\mu U)(\partial^\mu U^\dagger)], \tag{1.14}$$

with U being the meson fields, and f_π the pion decay constant (being inversely proportional to the $\pi - \pi$ coupling). Skyrme showed that when a quartic term involving

the derivatives ($\partial_\mu U$) was added to the meson Langragian, this self-interacting system possessed a static classical solution of finite size and energy, and with a conserved topological number q. Such solutions are called *solitons*. Skyrme proposed that the soliton in the $q = 1$ sector be identified with the nucleon. He also showed that two solitons in his model interacted strongly, the same as two baryons do in the large N_c limit of QCD. It appeared plausible that a sigma model, with quartic and higher order terms added to it, may be the effective Lagrangian of QCD at low energies. The effective Skyrme Lagrangian density in the SU(2)×SU(2) sector is given by:

$$\mathcal{L} = \frac{f_\pi^2}{4} Tr(\partial_\mu U \partial^\mu U^\dagger) + \frac{1}{32 g_\rho^2} Tr[U^\dagger \partial_\mu U, U^\dagger \partial_\nu U]^2, \tag{1.15}$$

with $f_\pi = 93$ MeV, and g_ρ the coupling constant $f_{\rho\pi\pi}$. This effective Lagrangian contains only the physical meson fields in which the baryons appear as solitons and interact strongly. The whole approach is nonperturbative, allowing to bypass the problem of using perturbation theory even when the quark-gluon coupling α_s is large (recall the calculation of the hyperfine splitting that is valid only for small α_s). In contrast to a nucleon, a soliton with a topological charge $q = A$ cannot be considered to be a nucleus since its energy is larger than an assembly of A solitons. Even though the Lagrangian in Eq. 1.15 contains only bosonic fields it describes fermions in the $q = 1$ sector. It has been shown in various ways that Skyrme's soliton with $q = 1$ may admit double valued wave function under rotation of 2π and behaves like a spin-$\frac{1}{2}$ system.

The bound state version of the soliton model describes strange hyperons as bound states of heavy flavor mesons and a topological soliton [9]. This approach succeeded to predict both the spectra and magnetic moments of the charm and bottom hyperons. It was natural to use the soliton model to obtain further insight into the possibility for stable exotic baryons that cannot be formed of three quarks alone. Two sets of parameters (SetI with $f_\pi = 64.5$ MeV and $m_\pi = 0$, and setII with $f_\pi = 54$ MeV and $m_\pi = 0.139$ GeV) lead to the correct mass values for the nucleon and the Δ resonance. With these two sets the calculation predicted that a meson with $c = (-1)$ (an anti-charmed meson like: $D^0 = |\bar{c}u\rangle$) should be bound at 1.831 GeV (setI) or 1.751 MeV (setII). The 80 MeV difference between the two values provided a measure of the uncertainty of the prediction.

The pentaquarks in this model are hyperons formed of 5-quark configurations $|\bar{Q}qqqq\rangle$, where Q refer to the heavy charm or beauty quarks and q to the light u, d or s quarks. The isospin states of the non-strange $c = (-1)$ hyperon are $I = 0, 1, 2$, corresponding to the possible isospin values of the four light non-strange quarks that form the soliton. When the hyperfine splitting is taken into account, the mass formula for such hyperons is:

$$M_{HYP} = M_{SOL} + \omega + \frac{1}{2\Omega}[aJ(J+1) + (1-a)I(I+1) + a(a-1)J_M(J_M+1)] \tag{1.16}$$

where J is the spin of the hyperon, I is its isospin and J_M is the total angular momentum of the heavy meson (D). The soliton mass, energy and moment of inertia are denoted M_{SOL}, ω and Ω, respectively. The hyperfine structure coefficient a depends upon the state energy and the ratio between the decay constants of a heavy meson and a pion f_D/f_π. With both sets of parameters (setI and setII) a=0.16, and the

non-strange hyperon with $I = 0$ is bound by 180 MeV to 100 MeV below the $D - N$ threshold.

If one of the light quarks is a strange quark, then the pentaquark is described in this model as a two-meson state formed by a soliton and a $s = (-1)$ kaon and a $c = (+1)$ meson. The $P_{\bar{c}s}$ baryon has isospin values of $\frac{1}{2}$ and $\frac{3}{2}$. For $I = \frac{1}{2}$ the pentaquark mass prediction varies between 2860 MeV - 47 MeV below the $D_s - N$ threshold, and 2949 MeV - 42 MeV above this threshold.

In another soliton model calculation [10] high derivative terms are neglected in the Lagrangian and the pentaquark is considered to be a bound state of a heavy meson and an anti-soliton. An investigation was made in the $SU(2)_L \times SU(2)_R$ symmetry, in which the states have zero strangeness. When SU(3) flavor symmetry was incorporated into the model, in order to take the strange quark into account, a large number of degenerate pentaquark states were produced, which were weakly bound. They could be destabilized by higher order corrections. When, however, SU(3) symmetry breaking was taken into account it was shown that the most stable states should be the doublet $|\bar{Q}suud\rangle$ and $|\bar{Q}sudd\rangle$, and the state $|\bar{Q}ssud\rangle$. In the bound state picture the masses of these states were estimated to be:

$$|\bar{Q}suud\rangle = |\bar{Q}sudd\rangle \sim 2857\ MeV, \qquad |\bar{Q}ssud\rangle \sim 3009\ MeV. \tag{1.17}$$

1.2 Characteristics of the pentaquark

The pentaquark is predicted to be a doublet of states, $P^0_{\bar{c}s}$ and $P^-_{\bar{c}s}$, being constructed of $|\bar{c}suud\rangle$ and $|\bar{c}sddu\rangle$, respectively. Their spin and parity $J^p = \frac{1}{2}^-$. The quarks can be combined to form subgroups within the pentaquark, which are color singlets, or they can form a state which has a substructure of color octets and is only an overall color singlet. The substructure of color singlets in the $|\bar{c}suud\rangle$ state can be associated with well known mesons and baryons (being off-mass shell), such as $(D_s - N)$: $|\bar{c}s\rangle|uud\rangle$, $(\bar{D}^0 - \Lambda)$: $|\bar{c}u\rangle|uds\rangle$ and $(D^- - \Sigma^+)$: $|\bar{c}d\rangle|uus\rangle$. The same combinations of quarks can be associated also with other particles (a $|uds\rangle$ state can be either Λ or Σ^0) or with resonances. The wave function of the $P^0_{\bar{c}s}$ and $P^-_{\bar{c}s}$ should include all these possibilities and hence can be written schematically as:

$$\begin{aligned} \Psi_{P^0_{\bar{c}s}} &= \alpha_1 \Psi_{D_s^- - p} + \beta_1 \Psi_{\bar{D}^0 - \Lambda} + \gamma_1 \Psi_{D^- - \Sigma^+} + \delta_1 \Psi_{5q} + \ \dots\ , \\ \Psi_{P^-_{\bar{c}s}} &= \alpha_2 \Psi_{D_s^- - n} + \beta_2 \Psi_{\bar{D}^0 - \Sigma^-} + \gamma_2 \Psi_{D^- - \Lambda} + \delta_2 \Psi_{5q} + \ \dots\ . \end{aligned} \tag{1.18}$$

The first three terms represent the substructure of color-singlet components within the $P_{\bar{c}s}$ and the fourth term represents the color-octet contribution. The three dots represent all other possible terms in the wave function (other states or resonances). The notation $\Psi_{D_s^- - p}$ stands for $\Psi_{D_s^-}(\mathbf{R})\Psi_p(\text{-}\mathbf{R})$ and denotes the spatially separated off shell $D_s^- - p$ system. The coefficients α_1, β_1 etc. represent the overlap amplitudes, which depend on quantum numbers of the states and their radial overlap:

$$\alpha_1 \equiv \langle \Psi_{P^0_{\bar{c}s}} | \Psi_{D_s^- - p} \rangle, \quad \beta_1 \equiv \langle \Psi_{P^0_{\bar{c}s}} | \Psi_{\bar{D}^0 - \Lambda} \rangle, \ \dots \tag{1.19}$$

The lightest mass combination among the meson-baryon pairs is that of the $D_s - N$ (2.907 GeV/c^2). If the pentaquark has a larger mass it would decay strongly to these

particles. If it is a bound particle its structure can be that of a molecule formed of an off-shell meson and a baryon, or it can have a tight structure where the five quarks are in very short distances from one another.

The lifetime and decay modes of the pentaquark depend upon its (unknown) mass and internal structure. The pentaquark would decay strongly to its constituent particles if its mass is above threshold. As the mass of $P^0_{\bar{c}s}$ increases more decay channels are open: $\bar{D}^0 - \Lambda$ (above threshold of 2.981 GeV/c^2) and $D^- - \Sigma^+$ (above threshold of 3.058 GeV/c^2). If, on the other hand, the pentaquark mass is below threshold, it would decay weakly with lifetime of the order of 10^{-13} s (see below). Like decays of other charm hadrons, it is expected that the decay of the pentaquark would be a spectator decay [15]. In that picture, the anti-charm quark decays while the four other quarks, forming a spin zero state, are spectators in the decay process. The quarks in the final state are combined to form different decay products. Fig. 1.3 shows one of the possible decay diagrams.

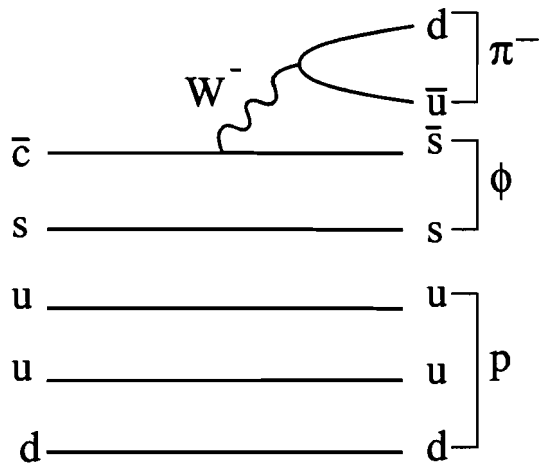

Figure 1.3: A possible decay diagram of the pentaquark. The $\bar{c}$ quark decays to $\bar{s}$ while the other quarks are spectators. The $\bar{c}$ decay involves a W^- intermediate state which decays to $\bar{u}$ and d quarks. The quarks combine to form hadrons in the final state ($\pi\phi p$).

For small binding energies of the pentaquark it is more likely that the pentaquark would have a molecular structure, with the off-shell meson and baryon being loosely bound together. In that picture it is expected that the off-shell charm mesons decay via the same decay modes as of the corresponding on-mass-shell mesons. The baryons remain spectators in the decay process because they are more stable. Table 1.1 lists some decay modes of the on-shell particles together with their branching fractions (B) [14]. Since the pentaquark decay in that picture is dominated by the decay of the off-shell meson we assume that the relative branching fraction for a specific meson is similar to that of the free meson. For example, for a pentaquark which decays via the $D_s^- - p$ part of the wave function, we expect to have twice as many decays to $\phi\pi^- - p$ than to $\phi\pi^+\pi^-\pi^- - p$.

D_S^-		D^-		Σ^+		$\bar{D}^0$		Λ	
Decay	B(%)	Decay	B(%)	Decay	B(%)	Decay	B(%)	Decay	B(%)
$\phi\pi^-$	3.6	$K^+\pi^-\pi^-$	9.1	$p\pi^0$	51.6	$K^+\pi^-\pi^-\pi^+$	7.5	$p\pi^-$	63.9
$\bar{K}^{*0}K^-$	3.4	$K^0\rho^-$	6.6	$n\pi^+$	48.3	$K^+\pi^-$	3.8		
$\phi\pi^+\pi^-\pi^-$	1.8	$K^0\pi^-$	2.7			$K^+\pi^-\pi^0$	13.9		
$K^+K^-\pi^-$	0.9								

Table 1.1: Major decay modes of the color-singlet components of the pentaquark and their branching fractions (B) for the on-shell particles.

The masses of the off-shell mesons are reduced when they are bound within the pentaquark, relative to the masses of the free mesons. As a result the available phase space for the decaying particles is reduced and consequently, the partial width for any decay mode is smaller, making the total lifetime longer.

The decay through the color-octet component can be a spectator decay of the anti-charm quark, as described above, which result in the same decay products as these of the molecule-like pentaquark. This component would allow also direct annihilation of the $\bar{c}$ quark on the s and d quarks via the Cabibbo allowed and suppressed transitions and other ways of quark final state interactions [15]. This will lead to decays of the pentaquark into the $p - K^-$ and $p - \pi^-$ systems. The Cabibbo allowed and suppressed exchange diagrams lead, via annihilation of the $\bar{c}$ on the u quark, to the $\Sigma^- - K^+, \Sigma^- - \pi^+$ and $\Xi^- - K^+$ decays. The diagrams in Fig. 1.4 give an example of the annihilation and exchange processes.

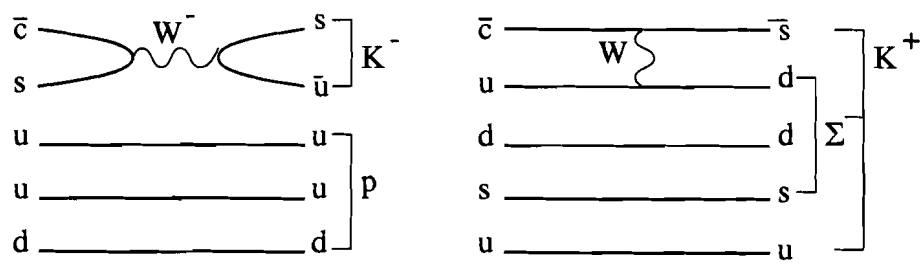

Figure 1.4: Cabibbo allowed and suppressed diagrams. Left: direct annihilation diagram. Right: exchange diagram.

The effect of having more decay channels on the pentaquark lifetime is to reduce it, but it is hard to estimate the branching fractions of these decays.

In summary, the decay modes of the pentaquark and its lifetime carry information about its internal structure. We expect that the lifetime of the pentaquark is somewhat longer or shorter than that of the D_s, in the range of 10^{-13} to 10^{-12} seconds.

1.3 Signature of the pentaquark

As discussed above, the decay of the $\bar{c}$ quark with the other quarks being spectators, or the decay of the off-shell meson in a molecule-like pentaquark result in the same decay products. The expected decay processes from the molecule-like pentaquark are therefore general and characterize many of the expected decays from the tight-structure part of the wave-function as well. Some of the decay processes expected from the molecule-like terms are listed below. Fig. 1.5 shows decay diagrams of two of these possible decay processes.

$\underline{\Psi_{D_s^- - p}}$

- $P^0_{\bar{c}s} \rightarrow \phi\pi^- p \rightarrow (K^+K^-)\pi^- p$
- $P^0_{\bar{c}s} \rightarrow K^{*0}K^- p \rightarrow (K^+\pi^-)K^- p$

$\underline{\Psi_{\bar{D}^0 - \Lambda}}$

- $P^0_{\bar{c}s} \rightarrow K^+\pi^-\pi^-\pi^+\Lambda \rightarrow K^+\pi^-\pi^-\pi^+(p\pi^-)$
- $P^0_{\bar{c}s} \rightarrow K^+\pi^-\pi^0\Lambda \rightarrow K^+\pi^-\pi^0(p\pi^-)$

$\underline{\Psi_{D^- - \Sigma^+}}$

- $P^0_{\bar{c}s} \rightarrow K^+\pi^-\pi^-\Sigma^+ \rightarrow K^+\pi^-\pi^-(p\pi^0)$
- $P^0_{\bar{c}s} \rightarrow \bar{K}^0\rho^-\Sigma^+ \rightarrow (\pi^+\pi^-)(\pi^-\pi^0)(p\pi^0)$

Here, the brackets stand for secondary decay process. The resonance particles ϕ, K^{*0} and ρ decay strongly in the decay vertex of the pentaquark. The baryons decay further downstream because of their relatively long lifetime (approximately 10^{-10} s), except for the proton which does not decay at all. Thus, the $\Psi_{D_s^- - p}$ term contributes decay modes that are characterized by a single decay vertex. The decays arising from the terms $\Psi_{\bar{D}^0 - \Lambda}$ and $\Psi_{D^- - \Sigma^+}$ involve two-step decays, with two separate decay vertices (as demonstrated in Fig. 1.5). When the off-shell meson decay involves a long-lived daughter particle, like the $\bar{K}^0$ in the decay $P^0_{\bar{c}s} \rightarrow \bar{K}^0\rho^-\Sigma^+$, the signature of the decay is even more complicated, with three decay vertices.

In an experiment that can detect charged particles efficiently, the preferable decay modes to search for are those with only charged particles in the final state. Among the decay modes listed above the expected decay modes from the $\Psi_{D_s^- - p}$ term are preferable for experimental search since it is more efficient to detect one decay vertex rather than two or three vertices. In these decay processes the momentum distribution of the emitted protons can provide information about the internal structure of the pentaquark. It will have a Fermi momentum distribution for a molecule-like pentaquark but could get higher momenta for a tight 5-quark state.

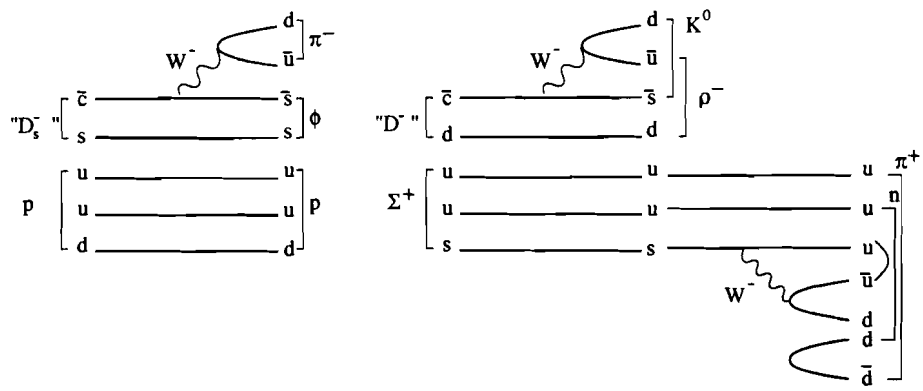

Figure 1.5: Decay diagrams from the molecule-like parts of the pentaquark wave function. Two decay processes are shown. Left: from the term $\Psi_{D_s^- - p}$, where "D_s" decays to $\phi\pi$ and the proton remains stable. Right: from the term $\Psi_{D^- - \Sigma^+}$, where "D^-" decays to $K^0\rho^-$ with Σ^+ being a spectator. In the second step Σ^+ decays to $n\pi^+$.

1.4 Production cross section of the pentaquark

Various mechanisms for pentaquark production have been discussed by H. Lipkin [16]. For the central hadron-nucleus charm production at several hundred GeV/c, the elementary process is often associated with the transitions $q\bar{q} \rightarrow c\bar{c}$ or $gg \rightarrow c\bar{c}$ (g refers to a gluon). The produced charm quarks propagate and hadronize. Mesons and baryons are formed according to the probability for the charm quarks to join together with appropriate quarks and antiquarks in the developing color field. Only crude estimates of the pentaquark production cross-section exist in the literature [17, 18, 19]. One mechanism considers a production of all five quarks in the interaction [17, 19] and is based on an empirically motivated equation which predicts reasonably well the production cross-section of other charm particles. Another mechanism is the coalescence model, where pentaquark components such as the $D_s^{\pm}$ and a nucleon are produced in the reaction and fuse into one particle while in overlapping regions of phase-space [17, 18]. Typically, the estimated pentaquark production cross-section is of the order of 1% that of the $D_s^{\pm}$.

1.4.1 Full production

The cross section for full production of the five quarks that form the $P_{\bar{c}s}$ can be estimated using an empirical formula [20, 21] which reasonably describes the production cross section of a mass M hadron for low p_t in central collisions:

$$d\sigma/dp_t^2 \sim exp\left(-B\sqrt{M^2 + p_t^2}\right) \tag{1.20}$$

where B is $\sim$ 5 - 6 (GeV)$^{-1}$. The cross section of the full production of the five quarks that form the pentaquark can be expected to obey this formula too. After integrating over p_t^2 the ratio between the cross section to produce pentaquark and D_s can be estimated:

$$\sigma(P_{\bar{c}s})/\sigma(D_s) \sim \exp[-5[m(P_{\bar{c}s}) - m(D_s)]] \sim 10^{-2}. \tag{1.21}$$

1.4.2 Coalescence model

The coalescence mechanism is expected to be the main mechanism for central production through the long-range (molecular) components of the pentaquark wave function (Eq. 1.18). The weakly bound $P_{\bar{c}s}$ can be produced for example by coalescence of a proton or a neutron with a D_s, analogous to the production of a deuteron by coalescence of a neutron and a proton. For this to happen the two coalescing hadrons must move within a small volume of phase space so that they can interact. The probability for that was calculated by a coalescence integral over the relevant space and momentum variables [20]. The integrand involves the space-momentum distribution functions of the two coalescing hadrons and a coalescence function that determines the overlap of these distributions. In a simplified description, if we assume that the tail of the pentaquark wave-function is dominated by the $D_s^- - N$ (N refers to a nucleon) combination, the coalescence probability to produce the pentaquark is:

$$C(P^0_{\bar{c}s}) = \frac{N(P^0_{\bar{c}s})}{N(D_s^-)N(p)}. \tag{1.22}$$

The numbers N stand for the number of particles produced in the region of central rapidity, in which the D_s mesons and protons are produced primarily. This region corresponds to the region of low positive x_f for the produced pentaquark. The coalescence probability for an antiproton and antineutron to produce an antideuteron is:

$$C(\bar{d}) = \frac{N(\bar{d})}{N(\bar{p})N(\bar{n})}. \tag{1.23}$$

If the pentaquark binding energy is of the order of few MeV, like that of the deuteron, it can be assumed that: $C(P^0_{\bar{c}s}) = C(\bar{d})$. When the yield ratios are written in terms of cross section ratios, the ratio between the cross section to produce the pentaquark and that to produce the D_s can be written as:

$$\frac{\sigma(P^0_{\bar{c}s})}{\sigma(D_s^-)} = \frac{\sigma(\bar{d})}{\sigma(\bar{p})} \cdot \frac{\sigma(p)}{\sigma(\bar{n})}. \tag{1.24}$$

The ratio $\frac{\sigma(\bar{d})}{\sigma(\bar{p})}$ was measured to be approximately 2.0×10^{-4} [22, 23]. The ratio $\frac{\sigma(p)}{\sigma(\bar{n})}$ was estimated to be 1.5 [18]. The ratio $\frac{\sigma(P^0_{\bar{c}s})}{\sigma(D_s^-)}$ was then estimated to be 3.0×10^{-4}. Since the coalescence integral depends on k^3, where k is the relative momentum between the components of the produced particle, the ratio $\frac{\sigma(P^0_{\bar{c}s})}{\sigma(\bar{d})}$ depends on $[k_{P^0}/k_{\bar{d}}]^3$. The result 3.0×10^{-4} was calculated for a very loosely bound particle with a Fermi motion of its components, of $k \simeq 150$ MeV/c. For a more tightly bound pentaquark, with $k_{P^0} \sim 250 - 350$ MeV/c, $\frac{\sigma(P^0_{\bar{c}s})}{\sigma(D_s^-)}$ would be 5 to 10 times higher. It was therefore estimated that:

$$\frac{\sigma(P^0_{\bar{c}s})}{\sigma(D_s^-)} \sim 3.0 \times (10^{-4} - 10^{-3}). \tag{1.25}$$

Other components in the wave function of the pentaquark, which describe pairs of color-singlet systems, can also contribute to the production cross section. The total cross section to produce the pentaquark through a coalescence process is therefore larger than the value in Eq. 1.25 and can reach the order of 1% relative to the cross section to produce the D_s.

1.5 Summary: What kind of pentaquark do we search for ?

In summary, based on the limited knowledge of the pentaquark structure and on the rough estimates of its production cross section, we searched for a pentaquark with the following characteristics:

- Mass between 2.75 and 2.91 GeV/c^2. The former is the lowest mass predicted by the CHI potential, and the latter is the threshold for strong decay.
- Lifetime ranging between 0.1 to 1.0 ps. As discussed in sec. 1.2 the lifetime should be somewhat longer or shorter than that of the D_s (0.47 ps). The lower limit on the lifetime was set by the acceptance of the experimental setup which was very poor for short-lived particles (as discussed in section 8.2.2).
- Production cross section of the order of 10^{-2} that of the D_s. We measured the cross section times branching fraction of a pentaquark decay relative to the cross section times branching fraction of a similar decay of the D_s, as discussed in more details in section 5.1.

We used the schematic pentaquark wave function of Eq. 1.18 to choose what decay modes of the pentaquark to search for. Since we decided to measure the pentaquark cross section relative to that of the D_s we naturally looked for decay modes expected to arise from the Ψ_{D_s-N} part of the wave function. These decay modes were also preferable from experimental point of view (see sec. 1.3). We chose to search for the pentaquark in its expected decay mode $P^0_{\bar{c}s} \rightarrow \phi\pi p$, where the ϕ subsequently decays to K^+K^-. This, and the similar decay $D_s^{\pm} \rightarrow \phi\pi^{\pm} \rightarrow K^+K^-\pi^{\pm}$, are convenient decay modes to detect because all decay products are charged, and because the narrow ϕ signal allows a rejection of K^+K^- background. Moreover, if the pentaquark is observed, the proton momentum can be measured and provide information about the pentaquark structure. If it is a molecular state, the proton is a spectator in the decay process and therefore has a Fermi momentum, but if it is a tight 5-quark state the proton momentum distribution may be harder.

Chapter 2

The Experiment

A search for a charm particle requires either knowledge of its production mechanism or some educated guess of its possible decay processes. For example, if the production mechanism of the pentaquark were known one could ideally plan a special search experiment. In such an experiment the pentaquark would be produced in an associated production with another charm particle (whos identity depends on the center of mass energy available in the interaction). By detecting the other charm particle one could tag the pentaquark (if exists) and measure its mass and the cross section to produce it. However, the more common way to search for a charm particle is via its decay modes. We looked for an experiment that was expected to produce many charm particles and we searched for the pentaquark via its expected decay mode to $\phi\pi p$. In such a search one should be able to detect the production and decay vertices in great precision and to identify the particles emerging from the decay vertex. We chose to participate in experiment E791 at Fermilab. The choice was made for the following reasons:

1. The goal of E791 was to study charm physics with high statistics.

2. E791 used an upgraded spectrometer which had been used in three previous experiments that studied charm physics (E516, E691 and E769). Thus, the ability of the experimental setup to provide good measurements of charm decays was already proven. In particular, in a previous stage of the experiment (E769), the D_s was measured via the $\phi\pi$ and K^*K decays. The resulted spectrum is shown in Fig. 2.1.

The D_s signal (S) shown in Fig. 2.1 consists of about one hundred events, over about one hundred background (BG) events. E791 was expected to collect fifty times more statistics than E769, meaning that a similar D_s signal would consist of about 5000 events. The measured ratio between the branching fractions for the $\phi\pi$ and K^*K is 0.93 ± 0.09 [24]. Thus, we could expect to see about 2300 events in a signal of the decay $D_s \rightarrow \phi\pi$, with the same cuts. A better ratio of $S/\sqrt{BG}$ would leave less events in this signal. This could make it possible to observe the pentaquark in the framework of E791 if a few assumptions would be fulfilled:

- The pentaquark is produced with a cross section being $\sim 1\%$ relative to that of the D_s (according to the theoretical estimates described in section 1.4).

- The pentaquark decays via channels similar to those of the D_s, with similar branching fractions.

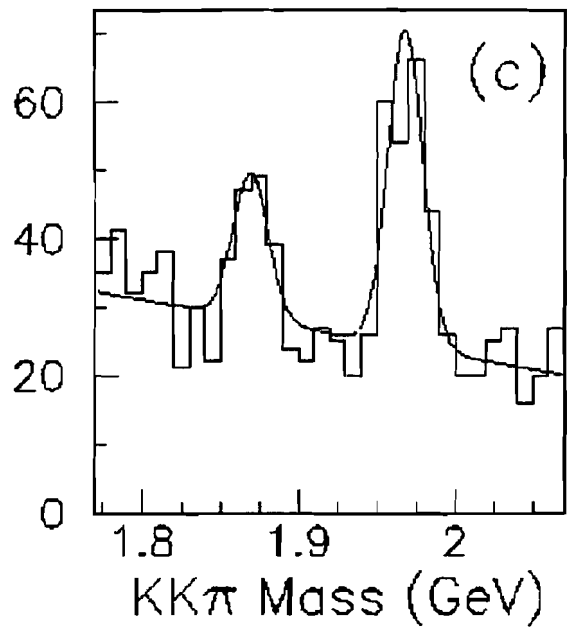

Figure 2.1: $KK\pi$ invariant mass from $\phi\pi$ and $K^{0*}K$ decays. The spectrum shows the signals of D_s (right) and $D^{\pm}$ (left).

- The efficiency to detect a pentaquark is similar to that to detect the D_s via the similar decay channels.

Based on these assumptions, we expected to measure up to about 20 events in the decay channel $P^0_{\bar{c}s} \rightarrow \phi\pi p$.

In this chapter I describe Fermilab experiment E791. Sections 2.1.1-2.1.8 describe the spectrometer and the targets. Sections 2.1.9 and 2.1.10 describe the trigger and the data acquisition system.

2.1 Fermilab E791 experiment

The goal of Fermilab E791 experiment was to collect enough data to cover many aspects of charm physics. The spectrometer, the target configuration, the trigger requirements and the data acquisition system were designed to fulfil this goal.

E791 used a 500 GeV/c π^- beam that interacted with a segmented target. Beam and target configuration are discussed in section 2.1.1. The particles that emerged from the interaction were detected by the Tagged Photon Spectrometer (TPS). The name was given to it in previous experiments, where photon beams were used for charm production. It included Silicon Micro-strip Detectors (SMDs), that allowed very precise reconstruction of production and decay vertices. Two magnets bended the particle tracks and allowed measurement of their charge and momentum. The hit information from ten Proportional Wire Chambers (PWCs) and four Stations of Drift Chambers was combined with the hit information from the SMD to reconstruct

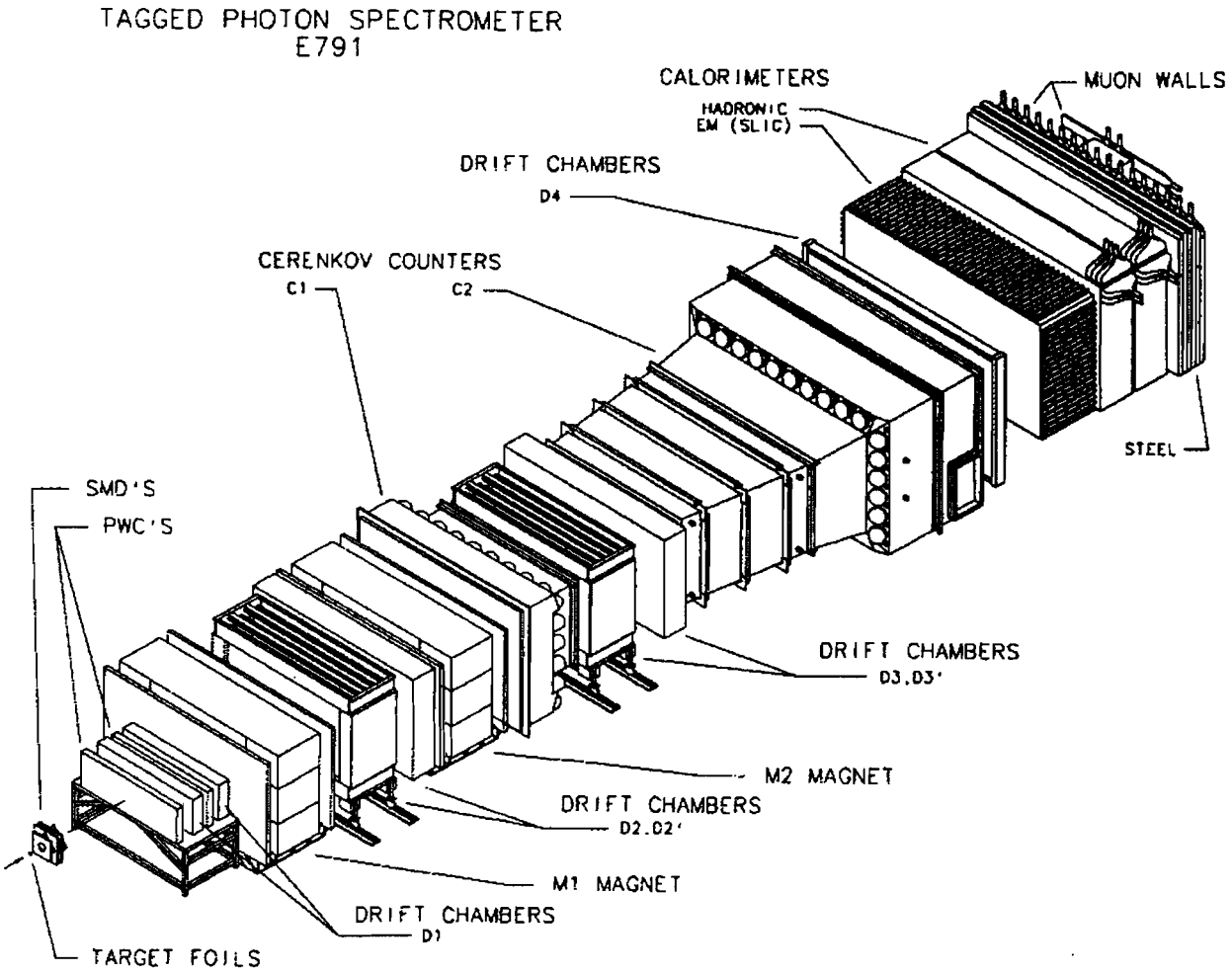

Figure 2.2: The Tagged Photon Spectrometer (TPS) used within Fermilab experiment 791.

the trajectory of particles within the spectrometer. Two multicell threshold Čerenkov counters were used for π, K and p identification. Electrons were identified by electromagnetic calorimeter. The energy deposited in the electromagnetic calorimeter and in an hadronic calorimeter, was used as part of the trigger requirements. Two walls of scintillators were located in the downstream end of the spectrometer, behind a shielding material, and were used for μ identification. Fig. 2.2 shows the TPS, and Sections 2.1.2-2.1.8 describe its components.

E791 used a minimal-bias trigger, described in section 2.1.9, with the aim not to reject charm decays of any type. The fast Data Acquisition (DA) system, described in section 2.1.10, collected about 9000 events per spill-second. In total, during its six months running time E791 selected and recorded about 2×10^{10} events to tapes, for off-line analysis.

2.1.1 Beam and target

The 500 GeV/c secondary π^- beam used by E791 was created from the primary proton beam that interacted with a 30 cm long Beryllium target. The 2×10^{12} protons per beam spill, originating from the Fermilab Tevatron main ring, produced about 10^7 pions per spill. A complete beam cycle was 57 seconds, and was split into two parts; the spill and the interspill. During the 22 second spill, pions were sent to the E791 targets, and during the interspill the accelerator ramped back up for the next spill cycle.

The target configuration was designed with two purposes in mind:

1. To maximize the number of interactions in the target material.
2. To keep the target thin in order to allow charm decays outside the target, such that clean measurement of decay vertices would be possible. Thin target would also minimize multiple scattering.

Fig. 2.3 shows E791 target.

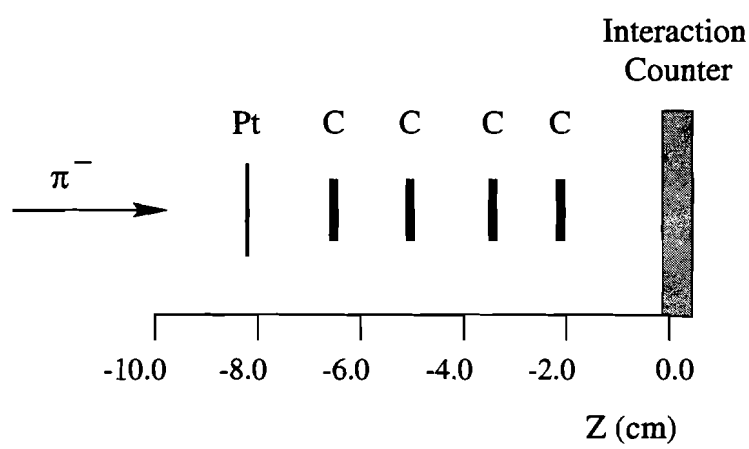

Figure 2.3: E791 target configuration. One platinum foil followed by four carbon foils, separated by gaps of approximately 1.5 cm.

It was built from five thin foils with spacing of roughly 1.5 cm between them. The foils were housed in a Lexan holding case. The first foil was a $50 Australian Platinum coin. The next four foils were made from industrial diamond drill bits (Carbon). The Platinum foil was placed upstream to the carbon foils to minimize multiple scattering effects (multiple scattering is inversely proportional to the number of protons in the nucleus). The total interaction length of the target foils was 3%. Spaces between them were determined to be slightly larger than a typical decay length of a charm particle. For example, the decay length of a $D^{\pm}$ meson, with a lifetime value of 1. ps and momentum equal to 70 GeV/c, is about 1.1 cm. Table 2.1 lists the characteristics of the target foils.

Target characteristics				
Foil number	Material	Z position (cm)	Thickness (cm)	Interaction length (%)
1	Pt	-8.191	0.052	0.584
2	C	-6.69	0.157	0.59
3	C	-5.154	0.157	0.585
4	C	-3.594	0.153	0.582
5	C	-2.060	0.154	0.587

Table 2.1: Characteristics of target foils

The Z positions of the target foils are given within the apparatus coordinate system. In this system the Z axis is directed along the beam, and the origin is defined to be the location of the "Interaction counter" scintillator (see section 2.1.9), downstream of the targets. X and Y axes are centered around the Z axis and follow a right handed coordinate system. For three dimensional reconstruction of particle tracks, the detectors measured hits in four additional directions transverse to the Z axis: U, V, W and W'. Their direction relative to the X axis are shown in Fig. 2.4.

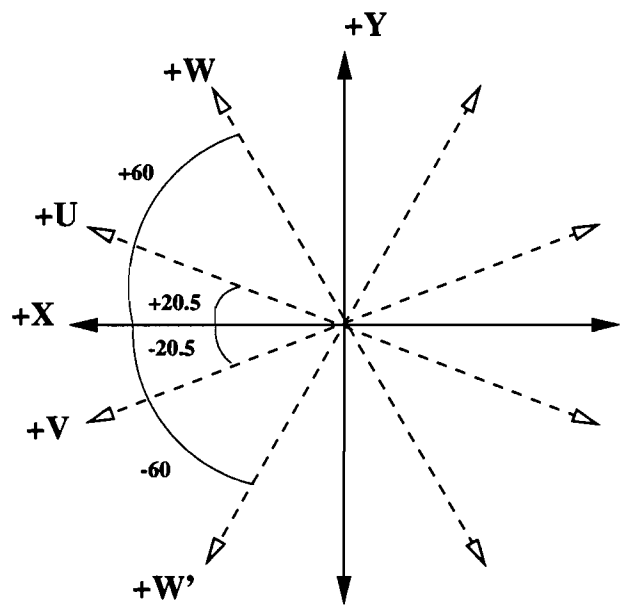

Figure 2.4: The E791 coordinate system showing the X, Y, U, V, W and W' views, with the beam directed into the page.

2.1.2 Silicon Microstrip Detector (SMD)

The SMD detector consisted of 23 planes of silicon microstrips, 300 μm thick. Schematics of a silicon wafer is shown in Fig. 2.5. The silicon wafers were ion implanted on both sides. P-type strips were formed by implanting boron in strips of silicon. A layer of aluminum was deposited over the boron doped silicon to serve as ohmic contact. The opposite side of the wafer was doped with a continuous n-layer of arsenic. Aluminum was deposited over the arsenic for good ohmic contact. The resulting p-i-n junction diodes were reverse biased at 60 to 90 V. A charged particle that traversed

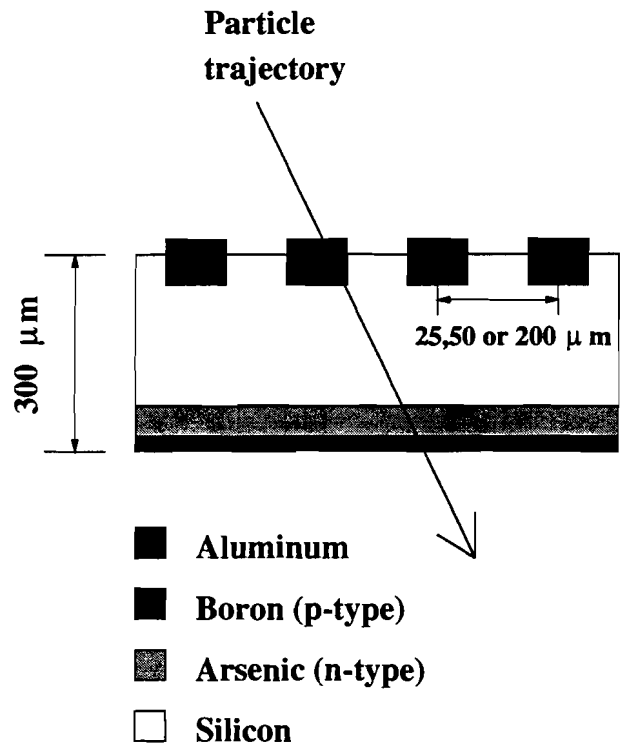

Figure 2.5: A schematic picture of a Silicon wafer.

the silicon strips caused on average 23,000 electron-hole pairs to be excited into the conduction band. These signals were amplified and read out through discriminators, raising a bit for each strip that was hit. The average efficiency of the silicon microstrips planes was approximately 90%, and their noise level about 0.1%.

Table 2.2 lists the characteristics of the SMD planes. Six of the 23 planes were located upstream of the target for beam tracking. The other 17 planes were located downstream of the target and were used in reconstructing the production and decay vertices and tracks. The resolution of each plane was determined by the spacing between its wires. It varied between 7 μm and 58 μm for wire spacing of 25 μm and 200 μm, respectively. Two tracks were resolvable if they were separated by more than 300 μrad. Resolution in Z for primary vertices ranged from 400 μm in the platinum foil to 240 μm in the most downstream foil [25]. The average resolution for a vertex of a charm decay was 350 μm in Z, and 6 μm in X and Y.

More detailed information about the SMD and its readout system can be found in references [26],[27] and [28].

SMD characteristics					
Plane number	Z position (cm)	Size (cm^2)	Strip pitch Inner ; Outer (μm)	Number of strips	View
1	-80.250	1×1	25 ; 50	384	Y
2	-79.919	1×1	25 ; 50	384	X
3	-74.429	1×1	25 ; 50	448	W
4	-33.163	1×1	25 ; 50	448	W
5	-30.133	1×1	25 ; 50	416	X
6	-29.483	1×1	25 ; 50	416	Y
7	0.670	1.6×1.6	25 ; 50	688	Y
8	1.000	1.6×1.6	50 ; 50	688	X
9	1.931	2.6×2.6	50 ; 50	512	X
10	3.015	2.6×2.6	50 ; 50	512	Y
11	6.684	2.6×2.6	50 ; 50	512	V
12	11.046	5×5	50 ; 50	768	Y
13	11.342	5×5	50 ; 50	768	X
14	14.956	5×5	50 ; 50	768	V
15	19.915	5×5	50 ; 50	1000	X
16	20.254	5×5	50 ; 50	1000	Y
17	23.878	5×5	50 ; 50	1000	V
18	27.558	10×10	50 ; 200	864	V
19	31.848	10×10	50 ; 200	864	X
20	34.548	10×10	50 ; 200	864	Y
21	37.248	10×10	50 ; 200	864	X
22	39.948	10×10	50 ; 200	864	Y
23	45.508	10×10	50 ; 200	864	V

Table 2.2: Characteristics of SMD planes. In some of the SMD planes the spacing between the central strips is smaller than the spacing between the outer strips. The column "Strip pitch Inner ; Outer" lists the different spacings.

2.1.3 Proportional Wire Chambers (PWCs)

Hit information from ten PWCs was used, together with the SMD, for beam and downstream tracking. Table 2.3 lists the characteristics of the PWCs. An extra view, X', was present in the PWC (and DC) system. It was a traditional X view plane with its cells shifted by half a cell width relative to the X view plane.

The PWC consisted of sense wires suspended in a gas mixture of 82.7% Argon, 17% CO_2 and 0.3% Freon. Charged particles that passed through a chamber ionized the gas mixture. The resulting free electrons, affected by an electric field, traveled towards one of the sense wires ionizing more molecules on their way and forming an avalanche of electrons on the wire. The pulse of electrons was collected within 4 ns. It was amplified by a Proportional Charge Operational System (PCOS), that set a bit for each wire from which the pulse was collected. The fast pulse collection made the PWCs tolerate high rates and hence they could be placed in the beam. The small

PWC characteristics		
	Upstream stations	Downstream stations
Planes	8	2
Z position (cm)	-3117 and -1212	118.5 and 161.1
Size (cm^2)	6.4×3.2	53.0×28.8
Wire spacing (cm)	0.1	0.2
Views	X,X' and Y,W	X,Y

Table 2.3: Characteristics of PWC planes

wire spacing in the PWCs together with the readout method allowed a fast measurement of a particle's hit position with the same resolution as the DCs (see sec. 2.1.4). However, due to their small size relative to DCs, they could be used for downstream tracking only in the region where the tracks were not yet affected by the magnets.

Eight PWCs, with the small wire spacing and resolution of 300 μm, were placed in two stations upstream of the target. The farthest station was placed at a distance of about 31 meters, with a resulting angular resolution of 10 μrad. Two PWCs, with the large wire spacing and resolution of 580 μm, were placed downstream to the target, beyond the SMD planes and alternating with the Drift Chambers in the first set before the magnets (see Fig. 2.2).

2.1.4 Drift Chambers (DCs)

Downstream tracking and momentum analysis were accomplished by fitting information from 35 DCs grouped in four stations: D1,D2,D3 and D4. Table 2.4 lists the characteristics of the Drift Chambers [29]. The DCs consisted of alternating sense and high-voltage planes in gas. The wires of the sense planes alternated between field shaping and sense wires. For D1, D2 and D3 the high-voltage planes were held at -2.1 kV to -2.6 kV, the field shaping wires at 0.4 – 0.6 kV higher, and the sense wires were grounded. D4 had its high-voltage planes at ground, a small positive high-voltage on its field shaping wires, and a large positive high-voltage on its sense wires. As for PWCs, a particle that passed through the DCs ionized the gas and the free electrons drifted towards the sense wires. The distance (d) of a particle hit from the closest sense wire could be determined by the relation: $d = \Delta t \cdot V_d$, where Δt and V_d were the electron's drift time and velocity, respectively. The drift velocity is determined by the gas mixture in the chambers and by the electric field strength. All the chambers were filled with 90% Argon, 10% CO_2 and ≈1% CF_4. They were operated with electric fields in the plateau regions, such that small changes in voltage would not affect the drift velocity. The resulted drift velocity was 50 μm/ns. Signals from the sense wires were read by Time to Digital Convectors (TDCs). The TDCs were operated in a common stop mode, meaning that the trigger was delayed and stopped the counting of all channels at the same time. They measured the drift time from the wire using the appropriate calibration [28]. By combining the distance of the hit position from the closest sense wire and the position of that wire in the plane, we could get the particle hit position in the detector coordinate system.

DC characteristics				
	D1	D2	D3	D4
Z position (cm)	142.5 - 183.7	381.4 - 500.8	928.1 - 1047.1	1738.0 - 1749.2
Number of channels	1536	2400	1952	416
Number of planes	8	12	12	3
Number of assemblies	2	4	4	1
Views	X, X', U, V	U, X, V	U, X, V	U, X, V
U,V cell size (cm)	0.476	0.892	1.487	2.97
X,X' cell size (cm)	0.446	0.953	1.588	3.18
Size (cm^2)	126×71	285×143	323×143	511×259
Resolution (μm)	400	300	300	450

Table 2.4: Characteristics of DC planes

2.1.5 Magnets

Two magnets located downstream of D1 and D2 stations, bent the particle trajectories in the $\pm X$ direction by a magnetic field in the $\pm Y$ direction. The magnetic fields in the two magnets were directed opposite to one another and hence caused to an opposite bend of a charged particle passing through them. This feature kept the particle trajectories in a forward direction. Table 2.5 lists the magnet characteristics.

Magnet characteristics		
	M1	M2
Z position (cm)	222.5 - 324.1	566.9 - 668.5
Front aperture (cm^2)	154×73	154×69
End aperture (cm^2)	183×91	186×86
Current (amps)	2500	1800
p_t kick (GeV/c)	0.212	0.320
$\int B \cdot d\ell$ (T-m)	0.711	1.077

Table 2.5: Characteristics of the magnets

The upstream magnet M1 had two coils as opposed to M2 that had 4 coils. It allowed operation of M2 with lower current than M1 but with larger bend in the transverse momentum (p_t kick) of a charged track. The resolution in momentum (p) was given by the expression ([30]):

$$\frac{\delta p}{p} = \frac{3.33(\delta x)p}{r \int B dl}, \tag{2.1}$$

where δx is the resolution in X and r is the lever arm to the Drift Chambers. The information from the magnets was used during reconstruction of the particle tracks.

2.1.6 Čerenkov counters

Two Čerenkov counters, located downstream of M2, provided information with which hadrons (π,K,p) could be identified. The search for the pentaquark required specifically a good hadronic particle identification (ID). Hence, as part of this thesis I

worked on the software related to the Čerenkov counters. I describe here in more details the Čerenkov counters, what information they gave and how did we use it for particle identification. Table 2.6 lists the characteristics of the Čerenkov counters. More detailed technical description of the design and construction of the Čerenkov detectors can be found elsewhere [31].

Čerenkov counter characteristics		
	Č1	Č2
Z position (cm)	534.1-866.0	1063.6-1653.4
Number of mirrors	28	32
Gas mixture	100% N_2	80% He 20% N_2
$(n-1)$	290×10^{-6}	86×10^{-6}

Table 2.6: Characteristics of the two Čerenkov counters.

The Čerenkov effect occurs when the velocity (v) of a charged particle exceeds the velocity of light in a dielectric medium (c/n), where n is the index of refraction for the medium and c is the speed of light in the vacuum [30]. Excited atoms in the vicinity of the particle become polarized and coherently emit radiation. The radiated light is confined to a cone around the particle's path. Due to constructive interference of the emitted wave front this cone is defined by an angle θ, such that $\cos(\theta) = c/vn$. Since $|\cos(\theta)| \leq 1$ a threshold momentum p_{th} must be exceeded in order for light to be emitted:

$$p_{th} = \frac{\gamma mc}{n}, \tag{2.2}$$

where $\gamma = (1 - (\frac{v_{th}}{c})^2)^{-\frac{1}{2}}$, m is the mass of the particle, and v_{th} is the threshold velocity $v_{th} = c/n$. Substituting v_{th} gives:

$$p_{th} = \frac{mc}{\sqrt{(n^2-1)}}. \tag{2.3}$$

The number of emitted photons, N, per unit length, ℓ, and wavelength, λ, is

$$\frac{dN}{d\ell d\lambda} = \frac{2\pi\alpha}{\lambda^2}(1 - \frac{p_{th}^2}{p^2}) \tag{2.4}$$

where p is the momentum and α is the fine structure constant (1/137). Based on the momentum measurement, a mass hypothesis, and the known index of refraction, a prediction can be made for the number of emitted photons.

Because Č1 and Č2 were filled with different gas mixtures, a particle began to emit Čerenkov radiation at a different threshold momentum for each counter. This feature allowed to identify particles in different momentum regions with a high probability. Table 2.7 lists the threshold momentum values for e, μ, π, K and p in Č1 and Č2.

	Threshold momenta, p_{th}				
Particle	e	μ	π	K	p
Č1 (GeV/c)	~ 0.03	~ 4	~ 6	~ 21	~ 40
Č2 (GeV/c)	~ 0.04	~ 8	~ 11	~ 39	~ 74

Table 2.7: Threshold momenta for e, μ, π, K and p in the Čerenkov counters.

The different threshold momenta of the particles resulted in different signatures at certain momentum regions. Table 2.8 shows the light response of Č1 and Č2 to the charged hadrons π, K, p in momentum bins. Muons give a similar signature to that of the pions since they have similar masses. The threshold momentum of electrons is very low and hence they always produce Čerenkov radiation in both counters. Muons and electrons were identified using information from the calorimeters in addition to their radiation emission in the Čerenkov counters.

Čerenkov counters light response						
Momentum	π		K		p	
(GeV/c)	Č1	Č2	Č1	Č2	Č1	Č2
<6	-	-	-	-	-	-
6 - 11	+	-	-	-	-	-
11 - 21	+	+	-	-	-	-
21 - 40	+	+	+	-	-	-
40 - 75	+	+	+	+	+	-
>75	+	+	+	+	+	+

Table 2.8: The light response of Č1 and Č2 to charged hadrons in momentum bins of the particles. The + or − signs refer to whether light is emitted or not, respectively.

The table shows that π,K and p have separable signatures between 21 to 40 GeV/c. Pions with these momenta radiate in both Č1 and Č2, while kaons radiate only in Č1, and protons do not radiate at all. Pions can be identified easily also in momenta between 6 to 21 GeV/c, since they radiate either only in Č1 or both in Č1 and Č2, while kaons and protons do not radiate at all. In the same manner, protons can be identified in momenta between 40 to 75 GeV/c since they radiate only in Č1, while kaons and pions having these momenta radiate in both Čerenkov counters. There are ambiguities in defining particles if they have the same signature in certain momentum bins. For example, identification between kaons and protons with momenta between 6 to 21 GeV/c is impossible since neither radiate in any of the Čerenkov counters. It should be mentioned that the response of the detectors is not a step function but rather a smooth rising function from zero to maximal response, as shown in Fig. 2.6. The curves in that figure are called *threshold curves* and they follow from Eq. 2.4.

Čerenkov light was projected on an array of mirrors, located transverse to the beam direction in the rear end of the two counters. There were 28 mirrors in Č1 and 32 in Č2. The light from a single track was usually projected on one to four mirrors. The mirror segmentation was chosen to minimize the number of cases where two or more particles in one event strike the same mirror. Therefore, the mirrors at the central

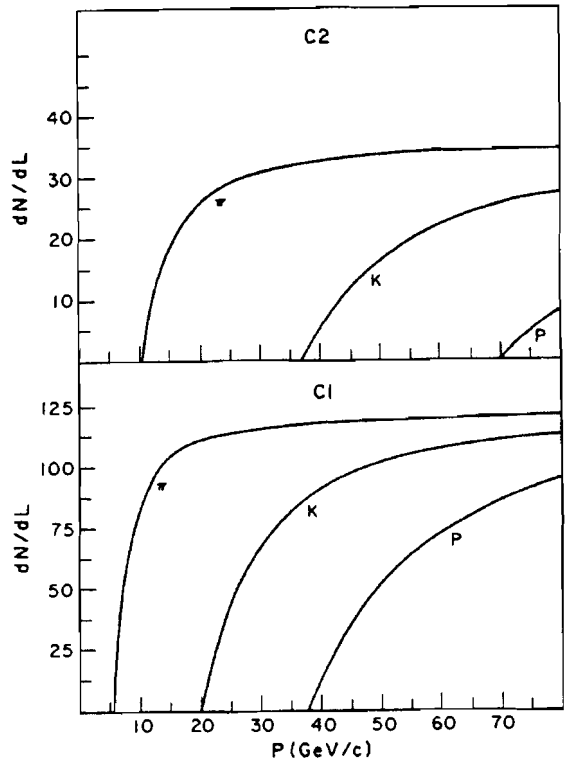

Figure 2.6: Number of photons per unit length in Č1 and Č2 assuming the efficiency is one for wavelength between 1600 and 5000 Å and zero otherwise.

region of the apparatus (near the beam) were smaller than the outer mirrors, as can be seen in Fig. 2.7. Because the spectrometer was originally designed for detecting photon induced reactions, a series of baffles were placed in the horizontal midplane of Č1 and Č2. Their role was to keep the Čerenkov radiation of electron-positron pairs (which were produced by photons from the beam) from reaching the reflecting mirror planes. The mirrors in the two arrays reflected the Čerenkov light to Winston cones that funneled light into phototubes. Each mirror directed the light to a separate phototube. Light with an angle of incidence greater than 20° bounced back out of the cones. RCA8854 phototubes were used to collect light. They produced pulse heights proportional to the number of photoelectrons, and the pulses were digitized by LRS 2249 ADCs. The fact that the output signal was linear with the number of photoelectrons was important when it was necessary to count how many photoelectrons were measured for a certain track, based on the calibrated signal hight representing a single photoelectron. Due to the good resolution of the phototubes at low photostatistics, it was possible to calculate the probability for a certain track to be of a certain particle using not only the fact that there was radiation emitted above the threshold momentum.

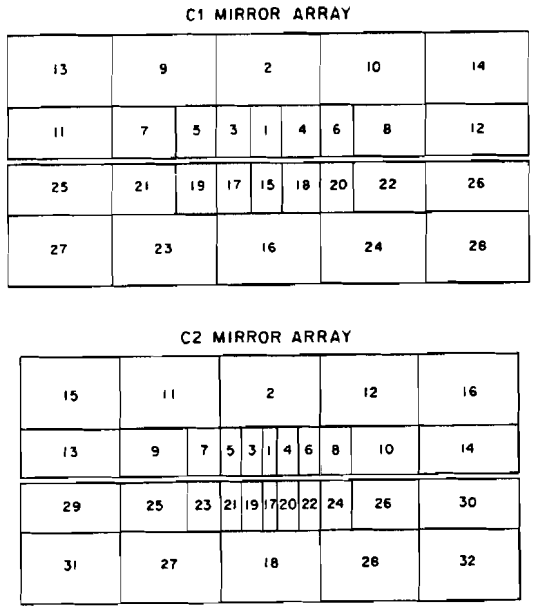

Figure 2.7: Mirror arrays in Č1 and Č2.

The Čerenkov particle ID algorithm compared between the amount of light collected for each reconstructed particle trajectory and that expected for each mass hypothesis for the measured momentum. The algorithm proceeded in three stages:

1. Calculate the measured amount of radiation in each mirror.
2. Predict the number of photoelectrons expected in that mirror from a particle of a given mass and with the measured momentum.
3. Determine the particle identification probability.

Each reconstructed track in an event was extrapolated in both Čerenkov counters. At selected intervals along the track's path, radiation was generated (if the momentum was above threshold) at the angle predicted by its measured momentum. This radiation was projected to the mirror plane, integrated over the track's path and a prediction was made for the average number of photoelectrons in each mirror:

$$\mu_{i,j,k} = F^{geo}_{i,j,k} \times F^{rad}_{i,j}(\beta) \times \overline{PE}_k \,. \tag{2.5}$$

The indices i, j, k stand for mass hypothesis, track number in the event, and mirror number, respectively. The factors $F^{geo}_{i,j,k}$ and $F^{rad}_{i,j}(\beta)$ indicate the geometrical fraction of the generated radiation that is collected by a given mirror, and the velocity dependent prediction of the fractional amount of radiation produced relative to $\beta = 1$ particle. $\overline{PE}_k$ is the calibrated average number of photoelectrons measured in a specific phototube (see in the description of the **calibration**). The predicted number of photoelectrons was summed over all mirrors that were expected to get Čerenkov radiation from a specific track. The sum did not include mirrors that collected light also from other tracks. For each Čerenkov counter a *consistency probability* was computed. It was a compound Poisson distribution that compared between the predicted

and measured number of photoelectrons:

$$PC_{i,j}(N,\mu,b) = \frac{\mu^N}{N}(1+b\mu)^{-N-1/b} \times \prod_{m=1}^{N-1}(1+mb)\,. \tag{2.6}$$

The quantities μ and N are the predicted number of photoelectrons (see Eq. 2.5) and the measured number from the specific track. The parameter b is the width of the distribution, averaged over the mirrors in the sum. μ and b were calibrated quantities related to the response of the mirrors in the two detectors, as discussed below. The overall likelihood that the measured number of photoelectrons in Č1 and Č2 could be generated by an hypothesized particle was given by the expression:

$$CPROB_{i,j} = PC1_{i,j} \times PC2_{i,j} \times A_i \tag{2.7}$$

with the demand that

$$\sum_{i=1}^{5} CPROB_{i,j} = 1 \tag{2.8}$$

The parameter A_i is the a priori likelihood to produce each one of the particles in the collision, as found from the data of Fermilab experiment E691 [31] ($A_e = 0.02$, $A_\mu = 0.01$, $A_\pi = 0.81$, $A_K = 0.12$, and $A_p = 0.04$). $PC1$ and $PC2$ were set to zero for tracks which were expected to produce light for an hypothesized mass, but no light was actually detected, or vice versa. If the simulation predicted the same result for more than one mass hypothesis then $PC1$ and $PC2$ were set to one for each of these hypotheses. In all other cases $PC1_{i,j}$ and $PC2_{i,j}$ had the form of the compound Poisson distribution as written in Eq. 2.6.

An example of CPROB distribution for a proton mass hypothesis is shown in fig 2.8. The tracks included in the peak at zero probability are definitely not protons. The peak at 0.04 is the a priori peak, where the program can not distinguish between π, K, and p. The peak at 0.25 is the ambiguity peak and it occurs due to undefined choice between K and p. ($PC1 = PC2 = 1$ for K and p, but zero for π, therefore the probability for proton hypothesized mass is: 0.04/(0.12+0.04)=0.25.) A cut in the analysis on the CPROB(M) spectrum served as a tool to choose tracks according to their associated mass probability.

Calibration

First, each phototube was calibrated. The phototubes were illuminated with a highly attenuated laser light. The output, digitized by the ADCs, showed the photoelectron peaks, where the first one was the most visible, but peaks of two and three photoelectrons were shown as well. The response of the phototubes was assumed to be linear and thus the measured number of photoelectrons could be expressed in terms of the measured ADC channels in which photopeaks were observed.

$$N_{measured} = \frac{(ADC - PED)}{SPEP} \tag{2.9}$$

where ADC is the raw ADC channel, PED is the pedestal: the lowest ADC channel in which counts are observed, and SPEP is the ADC channel of the single photoelectron peak corrected for the pedestal.

In order to predict how many photoelectrons would be detected from a track with a certain momentum and mass it was necessary to calibrate two quantities:

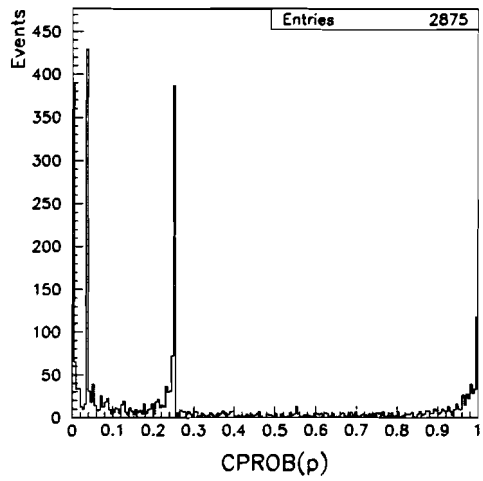

Figure 2.8: Probabilities assigned to tracks from simulated pentaquark decays, given the proton mass hypothesis.

1. The gains of the mirrors, that is, the average number of photons detected by the mirror+phototube for a track of infinite momentum.

2. The threshold curves of the hadrons π, K, p.

Multiplication of a mirror gain by the expression describing the threshold curve for a given mass hypothesis, would give the expected amount of light in that mirror due to that type of particle having the certain momentum ($\overline{PE}$).

For calibration of mirror gains we used a set of "isolated" tracks, whos simulated light ellipse was not interfering with light ellipses from any other track. These tracks were given the electron mass hypothesis since electrons produce the largest Čerenkov light cone. For each mirror we selected tracks that were centered on that mirror, such that the measured number of photoelectrons would represent its maximal response. The response of the phototube to the predicted number of photons was approximated by a compound Poisson probability distribution function (same expression as in Eq. 2.6). For each mirror+phototube, we compared the distributions of the measured and predicted number of photoelectrons by examining the ratio between their mean values (μ_{meas} and μ_{pred}, respectively). The gain was adjusted in five iterations using the expression: $GAIN = GAIN \cdot \frac{\mu_{meas}}{\mu_{pred}}$.

The final step was to accumulate the light projected from a single track and find the threshold curves for pion tracks in the two detectors. For this purpose we used the set of "isolated" tracks and assumed that these tracks were largely pions. The detected number of photoelectrons was plotted as a function of the momentum for each track. A fit was performed over a momentum range below the kaon momentum threshold, thus excluding kaon or proton contaminations. The fit near the pion radiation threshold ($p \leq p_{th}$) took the form $(1 - p_{th}^2/p^2)$, following Eq. 2.4. The threshold for kaons and protons follows from the ratio of their mass to the pion mass. Fig. 2.9 shows an example of the pion threshold curve for π tracks from Č1 and Č2.

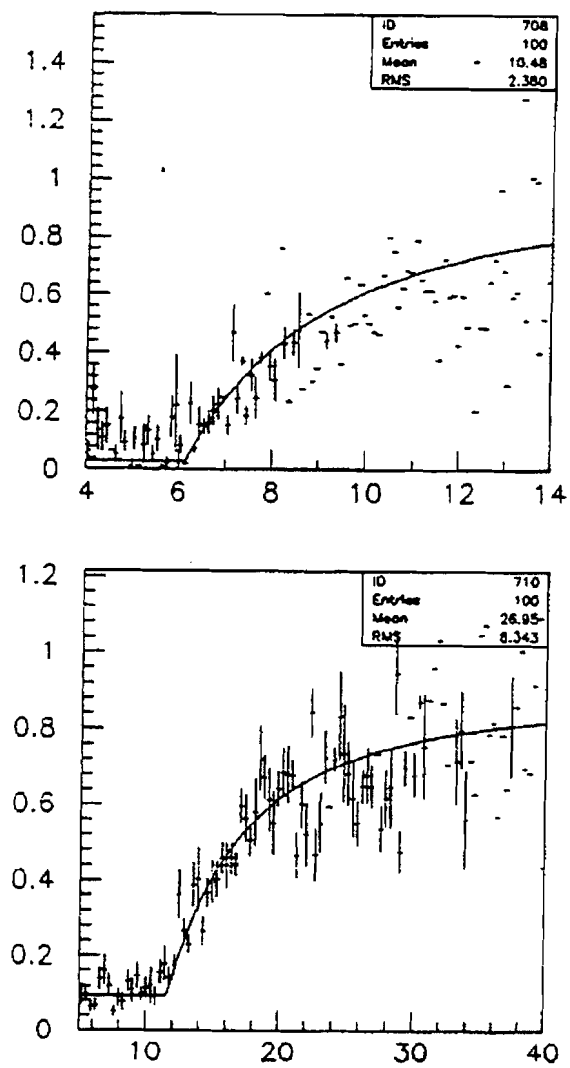

Figure 2.9: Threshold curves showing the light response of the two Čerenkov counters to pion tracks passing through them (Č1 at the top and Č2 at the bottom). The X axis shows the track momenta in units of GeV/c, and the Y axis is the measured number of photoelectrons per track divided by the gains of the mirrors detecting the light from that track. The curves follow the expression $(1 - p_{th}^2/p^2)$.

2.1.7 Calorimetry

The TPS contained electromagnetic and hadronic calorimeters. They were used to identify electrons and photons through observation of electromagnetic showers, and to identify neutral hadrons. The hadronic calorimeter also helped in muon identification since the signature of muons in it was unique relative to that of hadronic showers (muons deposit low energy and cause a small opening angle in what otherwise would be a shower). The probability calculated by the Čerenkov software for a muon hypothesis was increased if this signature was detected. The information from the calorimeters played a role in the trigger, as discussed in section 2.1.9.

Electromagnetic showers were reconstructed using information from the Segmented Liquid Ionization Calorimeter (SLIC). The SLIC was used to discriminate the relatively narrow electron showers from the wide charged hadron showers. Also the photon showers from π^0s and η's were reconstructed in the SLIC.

Table 2.9 lists the characteristics of the SLIC. It was constructed of 60 layers of oil-based scintillator, NE235H. Aluminum sheets coated with teflon were pressed to form corrugations 3.17 cm wide and 1.27 cm deep, forming one layer. Lead sheets, 0.63 cm thick, coated with aluminum, were placed over the corrugations to form one complete enclosure layer filled with the oil-based scintillator. The teflon coating had an index of refraction less than the oil so the light pipe made by the corrugation would be totally internally reflecting for light with an incidence of less than 20°. A total of 109 U and V and 116 Y views formed the entire SLIC. It was equivalent to 35 cm of iron.

When a charged particle hit the scintillating material, light traveled down the corrugations to collector wave bars that converted the ultraviolet light from the scintillators to green light. Mirrors terminated one end of the wave bars, and RCA 4902 phototubes terminated the other for readout of 20 channels. Individual channels in the congested center region were read out by RCA 4900 tubes to increase spacial resolution. Linear pulses from the tubes were then sent to Fast Encoding and Readout ADCs (FERAs) for digitisation. More details about the SLIC operation and the reconstruction procedure of electromagnetic showers can be found elsewhere ([32]).

SLIC characteristics	
Z position (cm)	1866 - 1962
Number of channels	334
Usable area (cm^2)	490×240
Radiation length	20
Absorption length	1.5
Energy resolution $\left(\frac{\Delta E}{E}\right)^2$	$(11.5\%)^2 + \left(\frac{17.4\%}{E}\right)^2$

Table 2.9: Characteristics of the SLIC

Hadronic information was provided by the Hadronic calorimeter (Hadrometer), located downstream of the SLIC. Less than 1% of the energy of electromagnetic showers reached the Hadrometer. Thus, charged hadrons were identified as wide SLIC showers, with significant hadronic energy measured in the Hadrometer. Neutral hadrons were found with the Hadrometer by subtracting energies associated with charged

tracks, then checking remaining energy distributions.

The Hadrometer was a steel-acrylic scintillator calorimeter. It contained 36 layers of 2.5 cm thick steel plates and 0.95 cm thick acrylic scintillator. The scintillator layers consisted of 14.5 cm wide plastic strips, alternating between X and Y views. The entire Hadrometer was equivalent to 102 cm of iron. Table 2.10 lists more characteristics of the Hadrometer.

The hadronic showers were sustained by interactions in the steel plates. The charged particles in the hadronic showers then produced light in the scintillators. The Hadrometer was divided into two modules, separated by a small gap, each consisted of 18 layers. The light from parallel strips in 9 layers was collected together into a single phototube (5 inch EMI9791KB) and the output signal was digitized by FERA. More details about the Hadrometer and how it was calibrated can be found elsewhere ([33]).

Hadrometer characteristics	
Z position (cm)	1973 - 2131
Number of channels	142
Usable area (cm^2)	490×270
Interaction length	6
Energy resolution $\left(\frac{\Delta E}{E}\right)^2$	$\frac{75\%}{\sqrt{E}}$

Table 2.10: Characteristics of the Hadrometer.

2.1.8 Muon detection system

The muon detection system of E791 consisted of a steel wall, used to range out hadrons, and two arrays of scintillator paddles: the X and Y muon walls. The steel wall, 102 cm thick, was placed downstream of the Hadrometer. Muons with momentum greater than 4 GeV/c passed through the whole spectrometer, a total of 239 cm iron-equivalent including the steel wall, to reach the scintillator walls. Table 2.11 lists the characteristics of the steel wall.

Steel wall characteristics	
Z position (cm)	2134 - 2236
Area (cm^2)	550×300

Table 2.11: Characteristics of the steel wall placed downstream of the Hadrometer.

The muon walls were located at the rear of the TPS with the Y wall being located approximately two meters downstream of the X wall. Between them, centered on the beam line was a concrete block with four paddles mounted on it for better detection of muons in the congested center region. Table 2.12 lists the characteristics of the X and Y muon walls. The X wall consisted of a total of fifteen 3 m long plastic scintillators, placed vertically for measuring the X position of passing charged particles. The twelve paddles in the outer portion of the X wall were 41 cm wide and the three central paddles were 61 cm wide. Light from the scintillators was collected by EMI9791KB

phototubes placed at the top of each paddle. Only latch information was recorded for this wall. The Y wall was smaller than the X wall. It consisted of 16 NE110 plastic scintillators, 3 m long and 14.5 cm wide, placed horizontally to measure Y position. The light was collected by phototubes placed on one end of the paddles. The signals from these phototubes were latched to inform which scintillator fired. They also generated TDC stops which were used to measure the X coordinate, but with a resolution of only 66 cm FWHM [34]. More detailed information on the muon system can be found elsewhere ([34]).

Muon wall characteristics		
	X wall	Y wall
Z position (cm)	2243	2419
Area (cm^2)	550×300	300×224

Table 2.12: Characteristics of the X and Y muon walls.

2.1.9 The trigger

The philosophy of E791 was to take data with a very open trigger in order to reduce bias in selection of charm events. Trigger decisions were based on information from a set of scintillators showing that interaction occurred, and on transverse energy deposited in the calorimeters.

Information from three scintillator paddles was considered in the trigger decision. They were located near the target and centered on the beam. Table 2.13 lists the paddle parameters, and Fig. 2.10 shows their location relative to the target.

Scintillating paddle characteristics			
	Beam Spot	Beam Halo Hole dia. = 1.0 cm	Interaction counter
Z position (cm)	-22.7	-16.3	0.0
Thickness (cm)	0.3	0.6	0.3
Height (cm)	1.3	7.6	4.0
Length (cm)	1.3	7.6	4.0

Table 2.13: Characteristics of the scintillating paddles of the trigger system.

A Beam Spot counter was used to determine whether one and only one beam pion was incident on the target. A Beam Halo counter, with a 1 cm hole at its center, was used to veto events where the beam particle did not come from the beam direction. Downstream of the target, an Interaction counter was used to detect charged particles from the interaction. A pulse height equivalent to more than four minimum ionizing particles in that counter ensured that interaction took place.

Demands on the energy deposit in the calorimeters were also part of the trigger requirements. Each calorimeter phototube had its last dynode signal sent to an amplifier that attenuated the pulses in a way that reflected their distance from the center, giving more weight to signals further from the beam axis. The sum of these signals

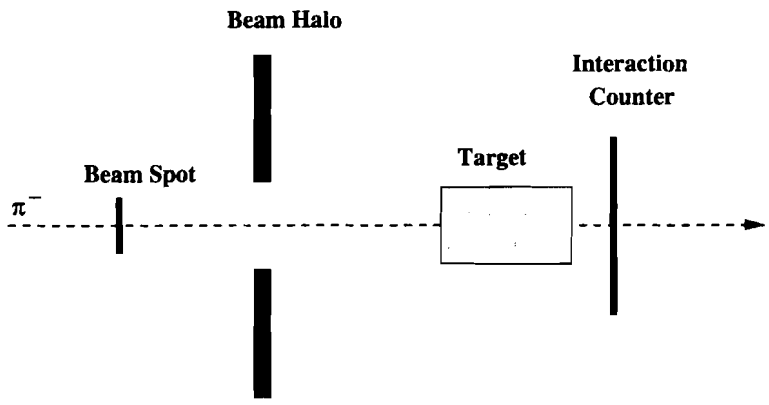

Figure 2.10: Beam counters and the Interaction counter used in the trigger.

gave a crude transverse energy (E_t) measurement during the run. The E_t deposited in the SLIC and Hadrometer had to be above a certain threshold to enrich the collected events with charm particles. The total energy (E_{tot}) in the calorimeters had to be below an upper boundary to reject events that contained multiple beam pion interactions.

Finally, the trigger requirement was:

$$\text{Clean beam} \bullet \text{.NOT.Halo} \bullet \text{Interaction} \bullet E_t \bullet E_{tot}$$

Clean beam was set to true if the signal in the Beam Spot counter was above threshold of a minimum ionizing particle but below a value which indicated that there was more than one pion in the beam. Halo was set to true if the signal in the Beam Halo counter was above threshold, meaning there was a particle not coming from the beam direction. Interaction was set to true if the signal in the Interaction counter was larger than four times a signal of a minimum ionizing particle. E_t and E_{tot} were set to true if the collected energy from the calorimeters was above and below a certain energy, respectively, as discussed above.

2.1.10 Data Acquisition (DA) system

The open trigger philosophy of E791 caused a very high rate of accepted events. Thus, a sophisticated high-speed DA system was developed. It is described in detail in reference [35]. The DA system read out approximately 2500 bytes per event with a dead-time of 50 μs. Events arrived at the DA system at an average rate of 26 Mb/s during the beam spill, and were recorded at 9.6 Mb/s, or 4000 events/s, during both spill and interspill using 42 Exabyte-8200 tape drives.

The DA system, shown schematically in Fig 2.11, was composed of five main parts. Event FIFO (First In First Out) Buffers (EFB) were used to store all digitized data from detector systems. Event Buffer Interface (EBI) controlled access to data by VME-based ACP-I computers. The CPUs packed digitized data into complete event records which were sent to Exabyte tape drives. A VAX 11/780 ran the user interface for the entire system.

Event FIFO Buffers (EFBs)

There were eight EFBs, each stored 80 Mb of data. Each EFB consisted of an I/O card, a FIFO controller card, five 16 Mb memory cards and a custom backplane. The EFBs maintained four status lines: Full, Near-full, Near-empty and Empty. The threshold for the Near-full or Near-empty were set by the I/O card's processor. The Near-full outputs were used in the E791 trigger logic to inhibit triggers whenever any EFB was in danger of overflowing. The Near-empty status was used by the event building processors, as described below.

Event Buffer Interface (EBI)

Data were distributed through EBIs to processors housed in six VME crates. Each VME crate held one EBI for every EFB in the system, so that every CPU had access to the output data path from every buffer. The EFB status lines were sent to EBIs so that the CPUs could determine how much data was available in the buffers. At any moment in time, only one CPU was granted control of a particular EFB. When a CPU in one crate finished to read data from EFB it passed control of the buffer to the next crate using the EBIs.

VME CPUs

The CPUs read event segments from the buffers, compressed them into formatted events and recorded them on tape through a SCSI Magnetic Tape Controller (MTC). The CPUs contained a 16 Mhz Motorola 68020 processor, a 68881 coprocessor and 2 Mb of memory. There were 8 event handler CPUs in each VME crate, plus a boss CPU.

The VAX-11/780

The VAX-11/780 was used to download and start the VME system through a low speed link between them. The DA system operator's console and status displays were also connected to the VAX.

Magnetic Tape Controller (MTC) and Drives

The tape drives were Exabyte-8200s writing single-density, 2.3 Gigabyte 8mm cassettes. The writing was handled by a VME to SCSI interface, the Ciprico RF3513. Two MTCs were used per VME crate, and were connected to 3 and 4 Exabyte drives. Thus, there were 7 Exabytes controlled from each VME crate, for a total of 42 drives in the DA system.

The two MTCs in a VME crate were managed by themselves and by one CPU in that crate. The MTC performed the actual transfer of a block of complete events from an event building CPU onto a single tape. The tape handling software was written to ensure that all 7 Exabyte drives on a VME crate were filling their tapes at about the same rate. During data taking, it took 3 hours to fill all 42 tapes.

Software

The DA software was comprised of three main programs. At the top VAX, which ran in the VAX-11/780. It accepted user commands, generated status displays and error logs, and fetched a tiny fraction of the incoming data to be monitored for data quality. Next was Boss, a program that ran in one CPU in each VME crate. It managed the other CPUs in its crate, and controlled the crate's MTC. Finally was Event Handler (EH) program which ran in several CPUs in each VME crate. Event Handlers read and checked events, formatted and compressed events, and assembled blocks of events for eventual output to tape.

Finally, the E791 Data Acquisition system successfully collected 20 billion events on 24,000 8mm tapes, twice the number estimated in the original E791 proposal.

2.1.11 My own contribution to E791

I participated in the setup stage of the experiment, in the test-run and in the data collection stage. I helped in the electronic setup of the Silicon Microstrip Detector, in control on the trigger logic and in tuning scintillators. My main contribution was to modify the software of the Čerenkov detector and to calibrate it to meet E791 needs as a service to the collaboration.

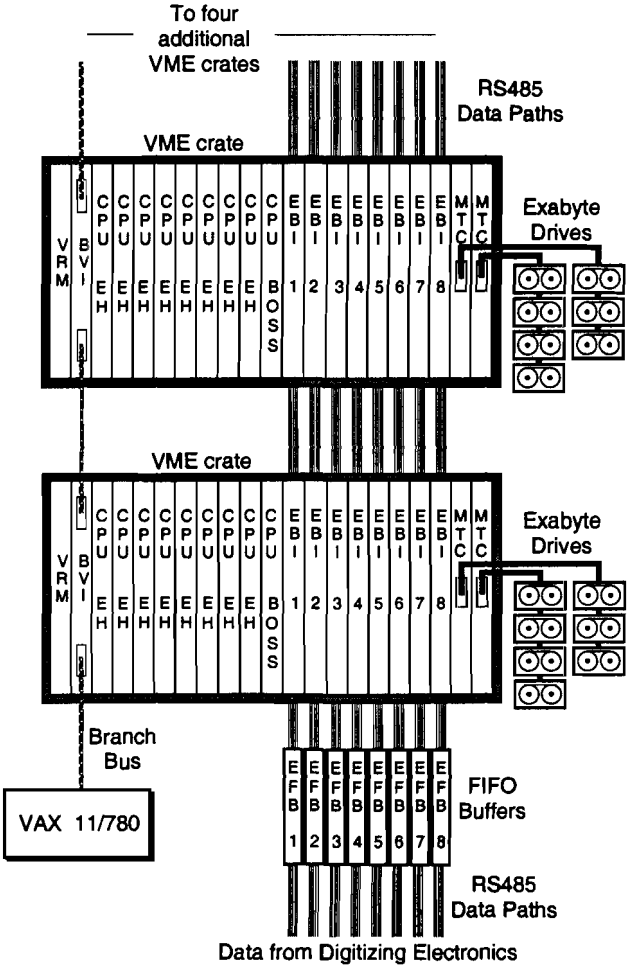

Figure 2.11: Schematics of data flow from electronic channels of the TPS, through FIFO buffers and event arranging buffers into 8 mm Exabyte tapes.

Chapter 3

Data Processing

During the E791 run in 1991, we filled with raw data approximately 24,000 2.3 Gb 8mm tapes. It was one of the E791 collaboration challenges to reduce this amount of data to a manageable size for physics analysis, without loosing the charm physics information buried in these tapes. The first stages of event reconstruction and data filtering were performed on "computer farms", large arrays of computers working in parallel, located at Kansas State University (KSU), The University of Mississippi (UMISS), The Centro Brasileiro de Fisicas (CBPF) and at Fermilab. All together these "farms" had about 7500 MIPS of computing power. Stripping processes, which further reduced the data size and narrowed the physics focus to a specific analysis, were performed on single workstations as they were I/O rather than CPU bound. Three years were required to reduce the data to the final sample used for the pentaquark search. Figure 3.1 shows data flow through the filter and stripping processes and the reduction in number of events at each level.

The reconstruction of tracks and vertices is described in section 3.1. The filter, strip and analysis routines used this information and calculated parameters on which selection criteria were applied. A short description of each of these parameters appears in section 3.2.1. Sections 3.2.2 and 3.2.3 describe the filter and strip programs which selected events in early stages of the analysis according to several physics goals. The selected events were packed, together with the tracks, vertices and Čerenkov information, on Data Summary Tapes (DSTs) for further analysis.

3.1 Reconstruction of tracks and vertices

Raw data hits in the detectors of the E791 spectrometer (TPS) were translated to physics information by the reconstruction program. In the first stage it reconstructed beam tracks, decay tracks and vertices, using the hit information from the SMD detector. If the interaction vertex was found, tracks were reconstructed using the information from the Drift Chambers and were matched with the SMD tracks.

3.1.1 Tracking

Charged particle tracks were reconstructed first in the SMD region. The reconstruction program performed two dimensional tracking in each SMD view $(X, Y, V\text{-}Z)$. Seed tracks were straight lines passing through at least two hits in a view, and then

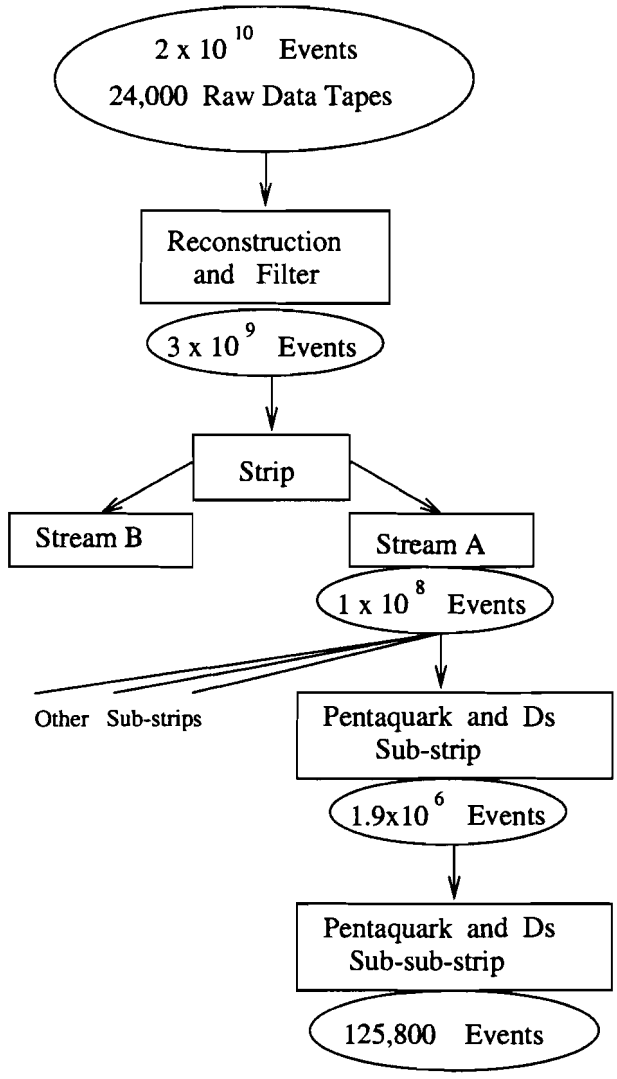

Figure 3.1: Block diagram showing the data reduction process used to select pentaquark and D_s candidate events. The number of events selected by each stripping level is listed.

additional hits were added. A good two-dimensional track candidate had to have at least four hits in X and Y views, and three in V view. Once all two-dimensional candidate tracks were found, they were combined to form three-dimensional tracks. The track hit position in a DC station was obtained from the hit information in its three views (see sec. 2.1.4). Downstream to the SMD region tracks were bended by the analysing magnets in the $X - Z$ plane. Thus, only Y intercepts of tracks on Drift Chambers were used to associate SMD tracks with DC hits. The DC hits which were not matched with the SMD tracks were used to reconstruct tracks in the Drift Chamber region only.

The quality of a reconstructed track was measured by the χ^2 per degree of freedom (χ^2/dof) that was calculated from the difference between the track's projected position at each detector and the actual hit. Tracks found in the SMDs and DCs with $\chi^2/dof < 10$ were kept.

3.1.2 Vertexing

Using the tracks found in the SMD region it was possible to reconstruct the interaction point (primary vertex) from the pion beam track intersection with at least two downstream tracks. The intersection of the three tracks was required to be in or near a target foil. Once a good candidate primary vertex was found, additional tracks were added to it as long as the χ^2/dof, calculated from tracks' impact parameters, was smaller than fifteen. Table 3.1 lists primary vertex resolutions as determined from $D^{\pm}$ data and MC simulation for the different target foils [25].

Primary resolutions	
Target foil	σ_z (μm)
P_t	400
C	320
C	320
C	260
C	240

Table 3.1: Resolutions of primary vertices reconstructed from $D^{\pm}$ data and Monte-Carlo simulation, in the Platinum and four Carbon targets.

The decay (secondary) vertices were reconstructed from the daughter tracks in the downstream SMDs traced back to the target region. The subset of all good tracks with momentum above 2.0 GeV/c was used in the process of secondary vertices reconstruction. Tracks belonging to the primary vertex could be included if their χ^2/dof contribution to the primary vertex was greater than 3.5 . A single track could participate in only one secondary vertex. The reconstruction program first searched for two tracks with a minimal distance between them, intersecting downstream of the primary vertex. Then, other tracks were added to this seed vertex in the same way as done for the primary vertex.

Lists of good tracks and vertices were packed on DSTs and were used in the filter and strip processes. The list of good tracks contained a variety of parameters characterizing them:

- The quality of their reconstruction given by the χ^2/dof (χ^2_{track}).
- Their category (CAT) which defines the TPS regions they reached. (see sec. 3.2.1)
- Their (X, Y) coordinates and slopes at certain Z positions along the spectrometer.
- Their momenta with errors as extracted from the curvature found using the DC information, and momentum projections (p_X, p_Y, p_Z) in the same Z positions as above.
- The Čerenkov probabilities assigned for five hypothesized masses for each track: e, μ, π, K, p (see sec. 2.1.6).

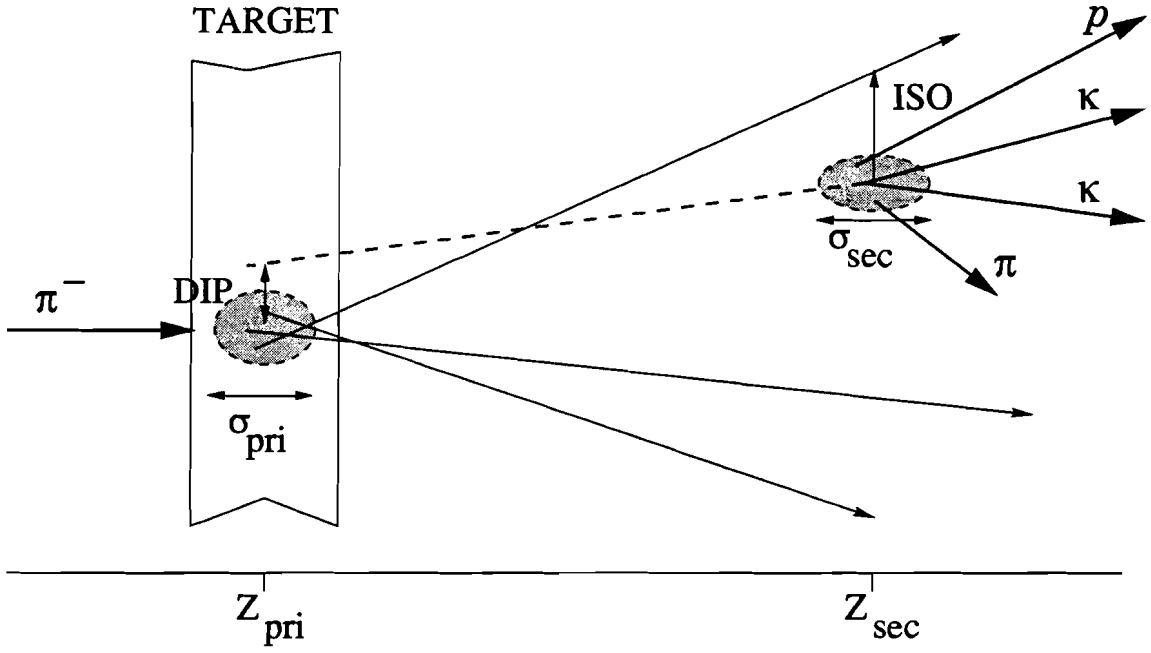

Figure 3.2: Scematics of an event with the production and decay of a pentaquark through the channel $P^0_{\bar{c}s} \rightarrow \phi\pi^{\mp}p^{\pm} \rightarrow K^+K^-\pi^{\mp}p^{\pm}$.

The subset of tracks examined by the pentaquark analysis was selected by applying cuts to these parameters. For the pentaquark search we did not use the list of good vertices but rather designed sub-stripping programs that used a different method to find the good 3- or 4-prong candidate vertices, as described in section 3.2.2.

3.2 Data reduction

After reconstruction, data were filtered in stages to keep charm events of interest to the E791 collaboration. A typical charm particle produced in the interaction flew in the laboratory a distance of approximately one centimeter before it decayed (see section 2.1.1). In the search for the pentaquark decay $P^0_{\bar{c}s} \rightarrow \phi\pi^{\mp}p^{\pm} \rightarrow K^+K^-\pi^{\mp}p^{\pm}$, we expect to detect the four charged tracks in the final state. The four tracks would emerge from the same decay vertex because the ϕ is a resonance which decays strongly. Such a decay is schematically shown in Fig. 3.2. The analysis parameters characterizing decays of charm particles in general, including that of the pentaquark, were subject to cuts in all analysis stages. A short description of each one of them appears below.

3.2.1 Analysis parameters

Track quality

- ⋆ χ^2_{track} : The χ^2/dof value, calculated by the reconstruction program for each track.

- ⋆ Track category (CAT) : Each track was given a category according to the location of Drift Chambers it hit. One bit in a four-bit integer was set for each station of Drift Chambers that the particle passed through, and the integer defined track category. For example, tracks with CAT=3,7,15 were selected for analyses of charm decays. Tracks with CAT=3 reached the second station of Drift Chambers (bits 1 and 2 are set), located right before the second magnet. Many of them were "ghost" tracks because noise in the DCs appeared as false hits that contributed to reconstruction of false tracks due to lack of more information from downstream chambers. Tracks with CAT=7,15 were better defined because they passed a longer way in the spectrometer, out of the magnetic field region and through the downstream Čerenkov counters.

- ⋆ Track new category (NCAT) : In order to reduce the large number of ghosts for category 3 tracks these tracks were fed to an Artificial Neural Network package and were given a new category (NCAT). The value of NCAT was the same as that of CAT except for the "ghost" tracks. Tracks identified as ghosts had NCAT = 28.

- ⋆ MOM_{track} : A track momentum was required to be smaller than a boundary which was large enough to include momenta of all possible decay products, but smaller than 500 GeV/c (the beam momentum), to exclude beam tracks.

Particle ID

- ⋆ C($K1$), C($K2$), C(π), C(p) : Čerenkov probabilities (CPROB(M)) assigned to the four candidate tracks, assuming that the first two were kaons, the third was a pion and the fourth was a proton. The algorithm used to calculate these probabilities is described in section 2.1.6.

Vertex quality

- ⋆ DSTMIN : Minimal distance between the two kaon candidate tracks. A cut on this parameter was required to ensure that the two kaon tracks originated at the same decay point.

- ⋆ χ^2_{pri} : χ^2/dof calculated from tracks' impact parameter to the fitted location of the production (primary) vertex.

* $\underline{\chi^2_{sec}}$: χ^2/dof calculated from tracks' impact parameter to the fitted location of the decay (secondary) vertex.

Vertex topology

* SDZ : The distance between the production (pri) and decay (sec) vertices, measured in units of the error in the measured longitudinal separation:

$$SDZ = \frac{Z_{sec} - Z_{pri}}{\sqrt{\sigma^2_{pri} + \sigma^2_{sec}}} \tag{3.1}$$

Z_{pri} and Z_{sec} are the Z positions of the primary and secondary vertices, and σ_{pri} and σ_{sec} are the errors in these measured positions. The measure of the distance between the two vertices in units of its error reduces the dependence of this parameter on the momentum of a candidate pentaquark or D_s. As the momentum of the candidate particle grows it moves a longer distance, but the error on the production and decay vertices grows too since it moves in a more forward direction.

* SIGMA : The distance of the decay vertex from the closest target surface, measured in units of the longitudinal error in the decay vertex reconstructed Z position :

$$SIGMA = \frac{|Z_{sec} - Z_{target}|}{\sigma_{sec}} \tag{3.2}$$

where Z_{target} is the Z position of the closest edge of the nearest target. This parameter allowed a separation between vertices which occurred within the target material (could be secondary interaction vertices) and those that occurred outside it (decay vertices).

* Decay Impact Parameter (DIP) : The momentum vector of the candidate pentaquark (or D_s) was calculated as the resultant of the four (or three) decay tracks and was extrapolated back to the primary vertex Z position. The DIP is the distance on the (X, Y) plane between the position of the candidate momentum vector to the primary vertex (this is the resultant impact parameter from the primary vertex).

* Ratio (RAT) : The likelihood that tracks belonged to the secondary vertex rather than to the primary vertex. It is defined as:

$$RAT = \prod_{i=1}^{n} \frac{(d_{sec})_i}{(d_{pri})_i} \tag{3.3}$$

where i runs over the n tracks in the decay vertex and $(d_{sec})_i$ and $(d_{pri})_i$ are the distances on the $(X - Y)$ plane of the ith track from the secondary and primary vertices, respectively. As the value of RAT gets smaller it is more likely that all the candidate tracks belong to the secondary vertex.

- ⋆ RAT$_i$/AVGR : The RAT parameter is small if all of the four tracks are closer to the secondary vertex than they are to the primary vertex, but it can be also small, for example, if even only one track is much closer to the secondary position than the others. Alternatively, a RAT parameter calculated for a very good 3-prong vertex with one far track may still be small. In order to get more information about the contribution of individual tracks to the vertex quality we used the ratio:

$$\frac{RAT_i}{\sum_{i=1}^{n}(Rat_i)/n} \tag{3.4}$$

where $Rat_i = (d_{sec})_i/(d_{pri})_i$ is the individual ratio for each of the daughter tracks in the decay vertex (n=4 or 3 in pentaquark or D_s searches), and $\sum_{i=1}^{n}(Rat_i)/n$ is the average of this parameter among these tracks. The ratio in equation 3.4 estimates the contribution of each of the daughter tracks to the total RAT parameter and allows rejection of peculiar vertices.

- ⋆ MAXRAT$_i$: the maximal Rat_i among these parameters calculated for the tracks in the decay vertex.

- ⋆ ISOLATION (ISO) : This parameter measures how well a secondary vertex is isolated from its neighboring tracks. The distance on the $(X - Y)$ plane of tracks not belonging to the chosen secondary vertex is calculated with respect to this vertex. The ISO is defined as the minimal distance.

Kinematics

- ⋆ Pt2dk : The squared transverse momenta ($\sum_i p_t^2(i)$) of the tracks in the decay vertex, calculated relative to the direction of their summed momentum. This parameter is proportional to the Q value of a decay process (Energy$\sim p^2/2m$).

- ⋆ Invariant Mass : Invariant mass is calculated as a function of track momentum p_i and daughter mass m_i (both in units of GeV) for the n tracks in the vertex:

$$M = \sqrt{\left(\sum_{i=1}^{n}\sqrt{\vec{p}_i \cdot \vec{p}_i + m_i^2}\right)^2 - \left(\sum_{i=1}^{n}\vec{p}_i\right)^2}. \tag{3.5}$$

3.2.2 Filter requirements

In the first filtering stage the events selected by all filter programs were written to $\sim$ 8000 DST tapes, retaining roughly one sixth of the data. Two major programs selected events having:

1. At least one secondary vertex, well separated from the primary vertex. Secondary vertices with two tracks were required to be separated by $SDZ > 6$ (see section 3.2.1), and those with three or more tracks were required to be separated by $SDZ > 4$.

2. K_s^0 and Λ candidates reconstructed from tracks in the Drift Chambers' region as well as in the SMD region. These particles are relatively long-lived (of the order of 100 ps) and therefore expected to decay mainly downstream to the SMD.

These two programs, named "secondary vertex filter" and "Vee filter", respectively, selected about 95% of the events passed by the filter. The remaining 5% were selected by dedicated programs, designed for searching events with ϕs, B decays, difractive jets and various charm baryons.

The development of the "ϕ-filter" was part of my work and the Tel-Aviv group contribution to the filter programming. This program selected all events containing a $\phi \rightarrow K^+K^-$ decay without constraining the distance between primary and secondary vertices. Such events could be candidates in the pentaquark search via the decay $P^0_{\bar{c}s} \rightarrow \phi\pi p$, without the limitation of a minimal lifetime driven by the minimal normalized distance limitation (see filter selection (1)). Eventually, as this filter program was not applied to all the data, we did not use it for the selection of $\phi\pi p$ candidates. Nevertheless, we did use the events it selected for tuning the cuts on variables related to ϕs within the $\phi\pi p$ sample (sec. 5.4.1 and 6.2.1). For the pentaquark search we used the events selected by the "secondary vertex filter" in the analysis of 2/3 of E791 data, and for the remaining third I wrote a dedicated candidate driven algorithm to select the candidate decays $P^0_{\bar{c}s} \rightarrow \phi\pi p \rightarrow K^+K^-\pi p$ and $P^0_{\bar{c}s} \rightarrow K^{*0}Kp \rightarrow K^+K^-\pi p$. The "pentaquark filter" and a similar "D_s filter" were included in the filter package instead of the "ϕ-filter" for the remaining third of the data . These two filter programs passed approximately 7% of the selected events.

Pentaquark filter

The "pentaquark filter" was based on a mass driven method. In its first stage it chose a subset of good tracks, characterized by:

- $\chi^2_{track} < 5$.
- Category (CAT) between 3 to 15.
- Momentum between 2. to 400. GeV/c.

In the next stage the program chose ϕ-candidates. It looked for oppositely charged pairs of kaon candidate tracks as potentially arising from ϕ decays. One in each pair of kaon candidates was required to have a Čerenkov probability larger than the a priori value to be a kaon. For the other kaon candidate the criterion was somewhat looser and it could have also an a priory probability value. The product of the two kaon Čerenkov probabilities was required to be greater than 0.05. The two candidate kaons had to pass close to each other, with a distance of closest approach <0.005 cm, and their invariant mass had to be within ± 10 MeV/c^2 of $m(\phi)$.

In the next step a pion and a proton candidates were selected from the list of good tracks. Tracks were identified as protons if their Čerenkov probability for protons had the a priori value or more. All other tracks were assumed to be pions since most of the tracks emerging from the interaction and decays were pions.

For K^{*0} selection the pion candidate was matched with the kaon candidate having an opposite charge. The distance of closest approach between them had to be <0.005 cm, and their invariant mass had to be within ± 50 MeV/c^2 of m(K^{*0}).

Finally, for producing a pentaquark candidate decay, a secondary vertex was reconstructed using the track information of the two kaons, pion and proton candidates. It was required that the invariant mass of the four particles would be between 2.0 to 3.1 GeV/c^2, that their total charge would be zero, and that $\chi^2_{sec} < 20$. The primary vertex was then re-reconstructed using the tracks in the original primary vertex and excluding the pentaquark daughter candidate tracks. It was required that Z_{pri} was in the target region (Z <-0.3 cm), and that $\chi^2_{pri} < 15$. It was further required that the momentum vector of the candidate pentaquark pointed back to the primary vertex with $DIP < 0.016$ cm, and that $RAT < 0.01$ (for definitions of Z_{pri}, χ^2_{pri}, χ^2_{sec}, DIP, and RAT see section 3.2.1). The selection criteria applied to the data by the "pentaquark filter" are listed in table 3.2.

	pentaquark			D_s		
	Filter	Strip	Sub-sub-strip	Filter	Strip	Sub-sub-strip
C($K1, K2$) >	0.12			0.1		0.12
C($K1$ or $K2$) >	0.13			-		0.13
C($K1 \bullet K2$) >	0.05			0.006		0.05
DSTMIN <	0.005 cm			0.005 cm		
ϕ MASS	$\pm$ 10 MeV/c^2			$\pm$ 14 MeV/c^2		$\pm$ 10 MeV/c^2
C(p) >	0.038			-		
C(π) >	-			-		
χ^2_{pri} <	15		5	15		5
χ^2_{sec} <	20		6	15		6
SDZ >	0		6	7		6
DIP <	0.016		0.004 cm	-		0.004 cm
RAT <	0.01		0.003	0.01		0.003
ISO >	-			0.0004 cm		-
INV. MASS	2.0-3.1 GeV/c^2		2.4-3.1 GeV/c^2	-		1.79-2.05 GeV/c^2

Table 3.2: Selection criteria required by the pentaquark and D_s filter and strip routines. C($K1, K2$) stands for a cut on the Čerenkov probability assigned to each of the two kaon candidate tracks. C($K1$ or $K2$) refers to a cut applied either to the first or to the second kaon. C($K1 \bullet K2$) stands for the product of the Čerenkov probabilities assigned to the two kaons.

3.2.3 Stripping processes

After filtering, data were stripped and written to two output streams. One stream selected events using the vertex list that was produced by the "secondary vertex filter", and the same events previously selected by the D_s and pentaquark filter programs. The selected events in this stream were used for the pentaquark search, as well as for production studies, $D^0 - \bar{D}^0$ mixing, doubly Cabibbo suppressed decays, FCNC, and more analyses done by the E791 collaborators. The other stream selected events from

the subset passed by the "Vee filter", which were used for baryon searches. Candidates for B decays and difractive jets events were selected by this stream too.

We further sub-stripped the events in the first stream to pass only pentaquark and D_s candidates. First we used the same programs that were used as part of the filter and strip packages. In later sub-sub-stripping programs we required tighter selection criteria in order to reduce the number of candidate events. Finally, the subset of events which we examined for the D_s and pentaquark searches included approximately 126,000 events. The criteria used to select them are listed in table 3.2.

Chapter 4

The Monte Carlo Simulation

In the framework of E791 analysis the hadroproduction is simulated using string fragmentation as implemented in the Lund model of the PYTHIA Monte Carlo (MC) program [36]. The pentaquark does not appear in the Lund table of particles because it is predicted to be constructed of five quarks, unlike any of the known hadrons. Moreover, there is no easy way to introduce the pentaquark into the table as a new particle since its production mechanism is unknown. Section 4.1 describes how we overcame this problem by substituting the known particle Ξ_c^0 by the pentaquark. The production characteristics of the pentaquark and the normalization sample of the D_s are discussed in section 4.2.1.

Decay processes and their detection by the spectrometer are simulated by the Monte Carlo too. The simulation takes into account noise, inefficiencies and resolution of the various detectors, and smears the simulated variables accordingly. The resulting simulated distributions should be similar to these of real observables. The efficiency calculated from the MC is reliable only to the extent that the simulation reproduces well distributions of the variables. By using ratios of efficiencies, as done in Eq. 5.1, this sensitivity is reduced for quantities that are common to the decays of the pentaquark and the D_s. These include the Čerenkov probabilities assigned for the kaon and pion candidate tracks, and the reconstruction and identification of the ϕ particle. The main differences are:

- Topology: The pentaquark decays into four charged particles, making the vertex a 4-prong vertex, while the D_s decay is a 3-prong vertex.
- Particle identification: The pentaquark has an additional proton track which has to be identified by the Čerenkov detector.
- Kinematics: We look for a pentaquark via a three-product decay (ϕ, π, p), while the D_s decays into two decay products (ϕ, π). Consequently, while the ϕ and π emerging from the D_s decay have an equal momentum in the D_s rest frame, the daughter particles of the pentaquark would carry varying fractions of its momentum.

In section 4.2.2 the distributions from Monte Carlo and data are compared for variables characterizing the decays of the D_s and the pentaquark.

	# Generated	After Filter	After Strip
MC($P^0_{\bar{c}s}$), M($P^0_{\bar{c}s}$)=2.75 GeV/c^2	107000	51360	30561
MC($P^0_{\bar{c}s}$), M($P^0_{\bar{c}s}$)=2.83 GeV/c^2	100000	48643	29004
MC(D_s)	108000	54649	30321

Table 4.1: Number of pentaquark and D_s generated events and the number of events selected by the Filter and Strip stages of analysis.

4.1 Generation of pentaquarks

The pentaquark was introduced into the Lund list of particles by replacing the Ξ^0_c. When a Ξ^0_c was produced it was renamed as the $P^0_{\bar{c}s}$, its mass was redefined to be 2.83 or 2.75 GeV/c^2, and it was forced to decay through the expected decay modes of the pentaquark. The binding energy of the pentaquark was defined to be either $\sim$ 150 or $\sim$70 MeV/c^2. The former is the largest possible binding energy, based on the CHI potential, but a more reasonable value for the binding energy is about half of it (see sec. 1.1). The Ξ^0_c is a good candidate to be replaced by the $P^0_{\bar{c}s}$ as it consists of the c, s and d quarks, which are common to the pentaquark. The heavy quarks are combined together to form the heavy Ξ^0_c baryon, and therefore it is possible to form a somewhat heavier particle with these quarks. The difference between the Ξ^0_c and pentaquark masses ($\sim$0.37 GeV/c^2) can cause violation of energy and momentum conservation when the Ξ^0_c is a decay product of a particle lighter than 2.75 or 2.83 GeV/c^2. In order to avoid such possible violations, all the decay modes containing Ξ^0_c as one of their products were vetoed. The decay chain defined for the pentaquark was: $P^0_{\bar{c}s} \rightarrow \phi\pi p$, where the ϕ decayed to K^+K^-. Since B($\phi \rightarrow K^+K^-$)=0.49, the detection efficiency (ε) was about twice its real value. However, the same decay channel of the ϕ was required in the simulation of D_s. Hence, this factor of two cancels in the ratio of efficiencies. The lifetime of the pentaquark was defined to be 0.4 ps, similar to that of other charm particles.

Table 4.1 lists the number of pentaquark events generated with masses of 2.75 and 2.83 GeV/c^2 and the number of generated D_s events. This table lists also the number of events selected by the filter and strip processes for each of the samples. It is noted that the fraction of events selected by the filter and strip processes is equal for all three samples. It means that the efficiency of the requirements in the filter and strip stages is equal when applied to the pentaquark and D_s MC samples.

4.2 Reliability of the MC

4.2.1 Study of x_F and p_T distributions

An important test of the Monte Carlo is the extent to which the predicted x_F (the longitudinal momentum of the produced particle) and p_T (its transverse momentum) distributions are consistent with the data and known production cross sections. Distributions of Monte Carlo x_F and p_T parameters at the production stage are shown in Fig. 4.1. These distributions are fitted by the functions: A(1-x_F)^n (for $x_F > 0$) and B$e^{-bp_T^2}$. The resulting n and b parameters are: n($P^0_{\bar{c}s}$) = 5.14 $\pm$ 0.04, n(D_s) = 5.15$\pm$0.05, b($P^0_{\bar{c}s}$) = 1.13 $\pm$ 0.01, b(D_s) = 1.24 $\pm$ 0.01. The values fitted for n and b

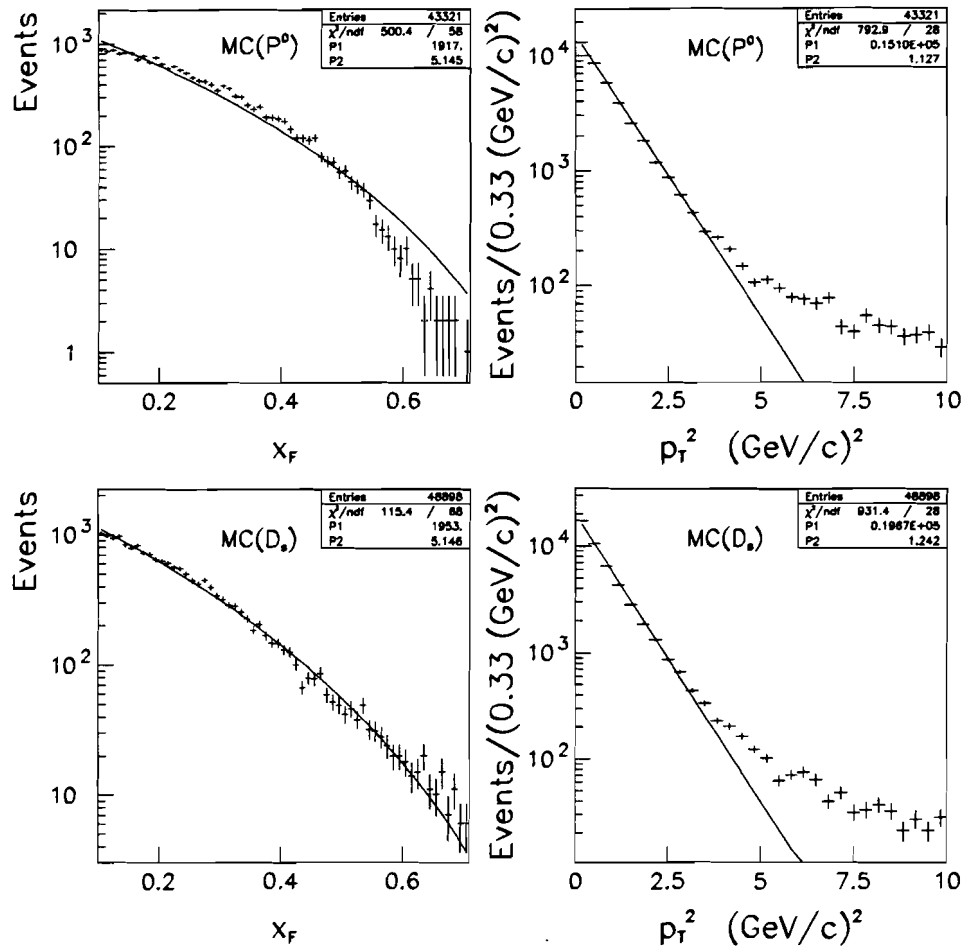

Figure 4.1: Distributions of x_F and p_T^2 at production from pentaquark and D_s MC simulations. The solid lines are the fit results of the functions $A(1-x_F)^n$ and $Be^{-bp_T^2}$.

are consistent with measured values for mesons and baryons [37].

The x_F distributions from MC and data for D_s events are shown in Fig. 4.2(a) and 4.2(b), respectively. The ratio between them, when the number of data events is normalized to the number of MC events, is shown in Fig. 4.2(c). It can be seen that the ratio is approximately one, meaning that the MC reproduces well the production process of D_s.

The similarity between the x_F distributions produced by the MC for pentaquarks and D_ss indicates that they are generated with the same dynamics, both in central production (low x_F). The search for the pentaquark is therefore constrained to its production with low x_F values. A systematic error in the search result due to erroneous simulation of the pentaquark production is discussed in sec. 7.2.6.

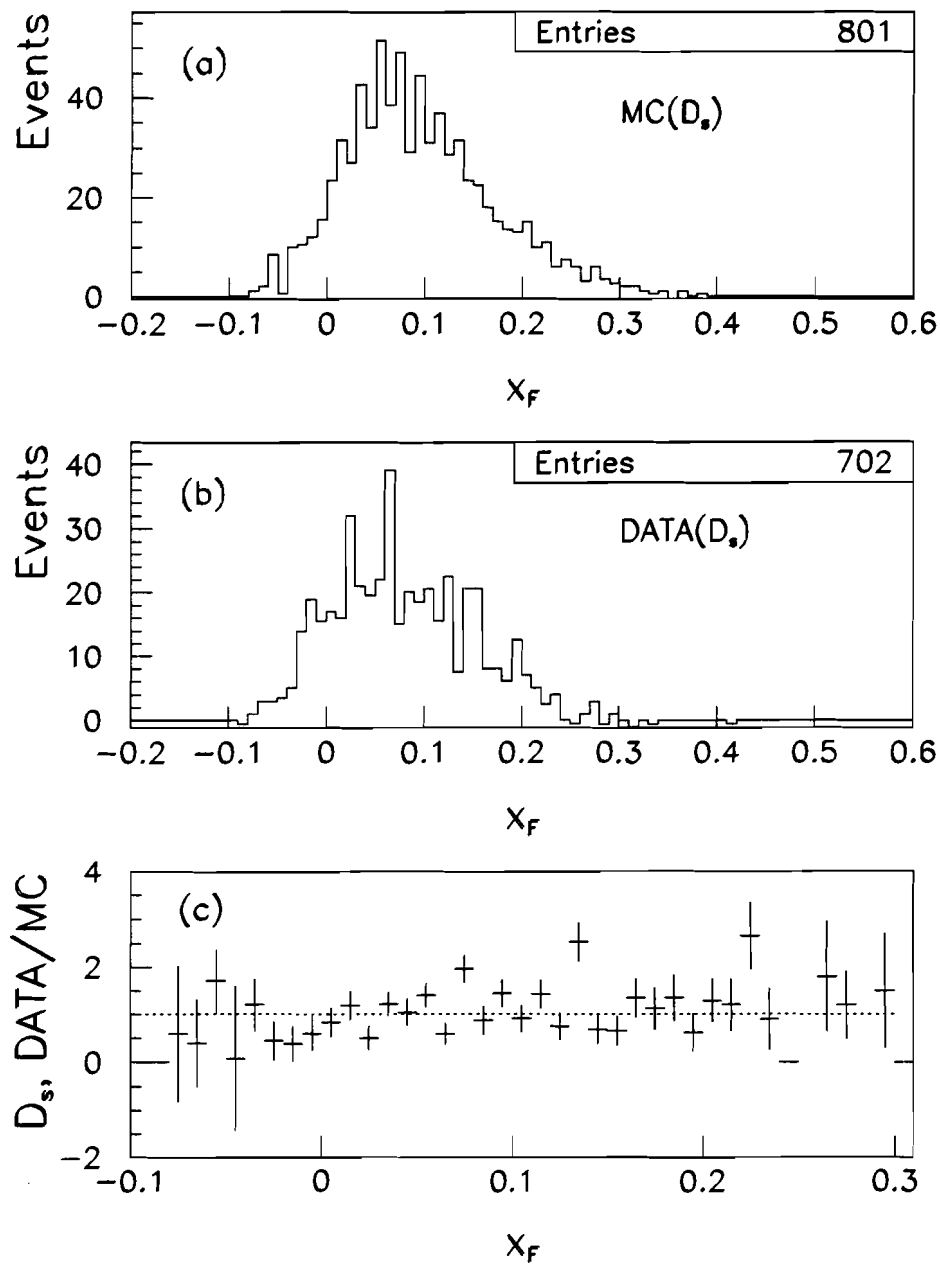

Figure 4.2: Distributions of x_F for events accepted in the D_s mass peak from (a) MC and (b) data. The events in the D_s peak are defined by vertex cuts and by the D_s mass window, where the background is subtracted from the distributions. (c) The ratio between these x_F distributions, when the number of data events is normalized to the number of MC events.

4.2.2 Distributions of decay variables

A comparison of variable distributions between MC and data was done directly for the D_s but not for the pentaquark. For variables characterizing both D_s and pentaquark decays we compared the distributions from D_s MC and data signals to those from the pentaquark MC. Other signals from data were used for comparison of variables for which the pentaquark differs from the D_s (see sec. 5.1). Mainly, for distributions of topological variables characterizing the 4-prong decay, the data from $D^0 \to K\pi\pi\pi$ were compared to the simulated pentaquark decays.

The comparison between variable distributions from MC and data was done in the following steps:

- First, we produced clean signals of $D_s \to \phi\pi \to K^+K^-\pi$ from MC and data, $D^0 \to K\pi\pi\pi$ from data and $P^0_{\bar{c}s} \to \phi\pi p \to K^+K^-\pi p$ from MC. To obtain clean signals we applied cuts to the variables characterizing the decay process. Correlated variables were grouped into "families":

  - Lifetime: SDZ
  - Vertex quality: χ^2_{pri}, χ^2_{sec}
  - Vertex separation: ISO, RAT, DIP
  - Čerenkov: C($K1$), C($K2$), C(π), C(p)
  - Decay kinematics: Pt2dk

  A variable was studied using a signal which was obtained with cuts applied only to variables not belonging to that variable's "family", to minimize correlations. As an example, Fig. 4.3 shows the D_s mass spectrum from data, with all cuts applied within this study (top left), and with the same requirements except for cuts on variables of a different "family" for each plot. It can be seen that in all plots the D_s signal is indeed "clean" with low level of background.

- The variables themselves were plotted with two mass cuts. One on 40 MeV/c^2 around the mass of the particle being tested, as it contains $\sim$ 90% of a mass signal. The other cut was on the background on both sides of the signal. The number of events in the background region was normalized by the ratio of the two mass ranges. The difference between the two distributions ("signal" minus "background") reflects the distribution that characterizes the signal.

Comparison of each of the variables is described in detail below.

Comparison of variables common to D_s and pentaquark analyses.

The C($K1$) is an example of a parameter common to the D_s and pentaquark analyses. Fig. 4.4 shows the C($K1$) distributions obtained from D_s signals from MC and data (top histograms). These signals were plotted with cuts on all variables except for those belonging to the "Čerenkov family". The C($K1$) distribution from the pentaquark signal from MC is shown in the same figure with the same requirements (bottom histogram). The fraction of events in the a-priory and ambiguity peaks (see section 2.1.6), out of the total number of events in each distribution, is the same within errors. In the a-priory peak the fraction is: 0.14±0.03, 0.12±0.01 and 0.15±0.02, in

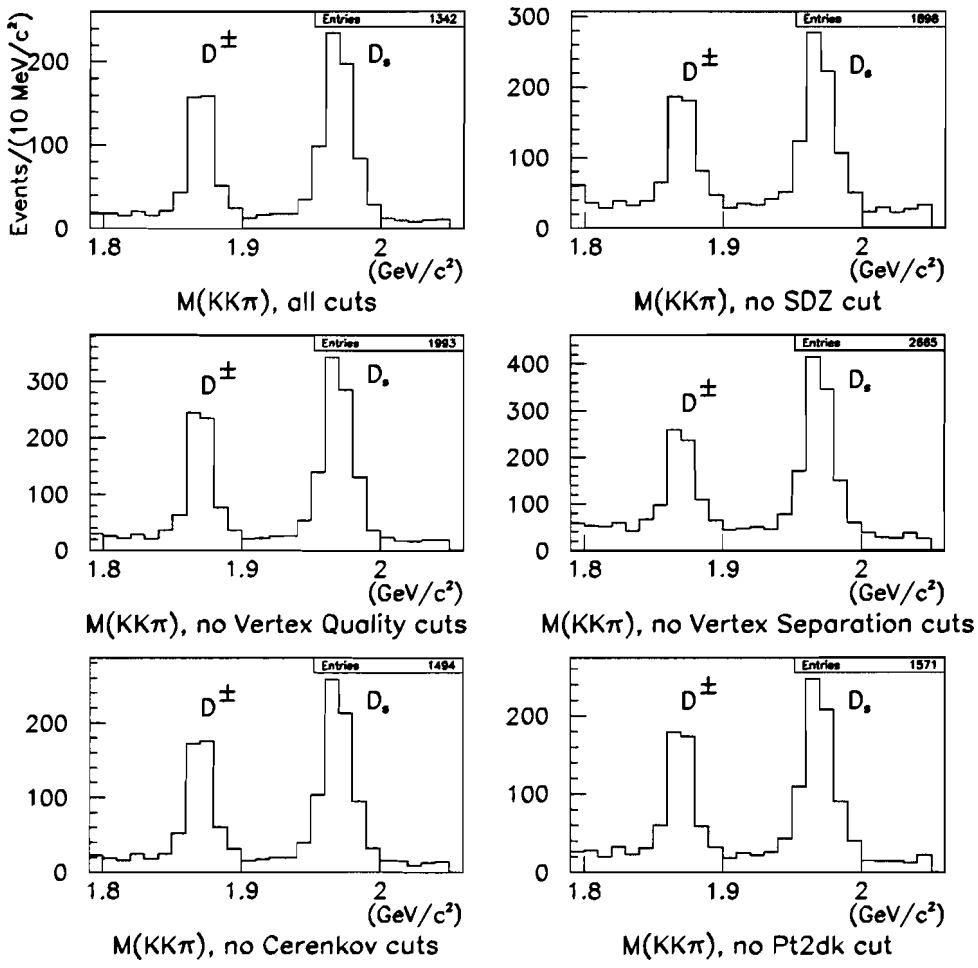

Figure 4.3: D_s mass spectra from data with all cuts (top left), and with all cuts except for those that belong to the stated "family".

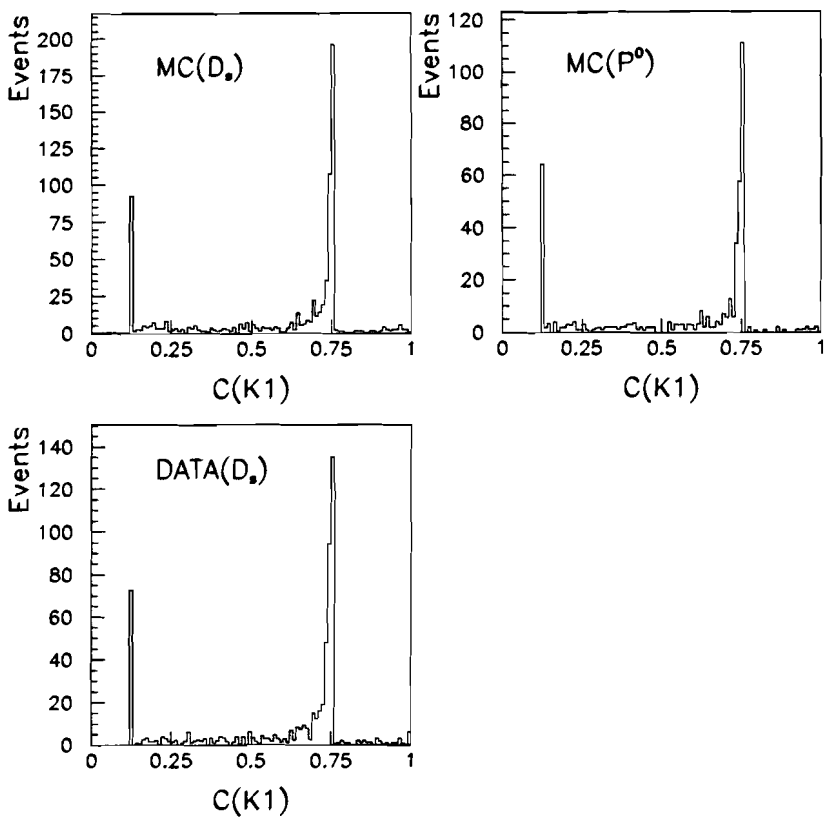

Figure 4.4: Distributions of C($K1$) for D_s signals from MC and data (left), and for the pentaquark signal from MC (right).

the distributions from MC(D_s), DATA(D_s) and MC($P^0_{\bar{c}s}$), respectively. The fraction of events in the ambiguity peaks in the same order is: 0.53±0.07, 0.56±0.03 and 0.52±0.04.

Comparison of topological vertex variables

For the comparison of the 4-prong vertex topology variables I used a sample of $D^0 \rightarrow K\pi\pi\pi$ from data. The D^0 has a lifetime similar to that of the D_s making it possible to apply the same SDZ cut in both analyses while examining other variables. The 4-prong topology variables (belonging to the "vertex quality" and "vertex separation" families) were compared in a process, which is described here for the χ^2_{sec} as an example. Fig. 4.5 shows χ^2_{sec} distributions for D_s signals from MC and data, for the pentaquark MC signal and for the D^0 signal from data. Differences are apparent between the distributions plotted from MC(D_s) or MC($P^0_{\bar{c}s}$) and data of D_s or D^0 decays. Note, however, that the discrepancies between MC and data are in the same direction for both 3- and 4-prong decays; the MC shows a better quality vertex than the data. This is the case for most of the 4-prong topology variables.

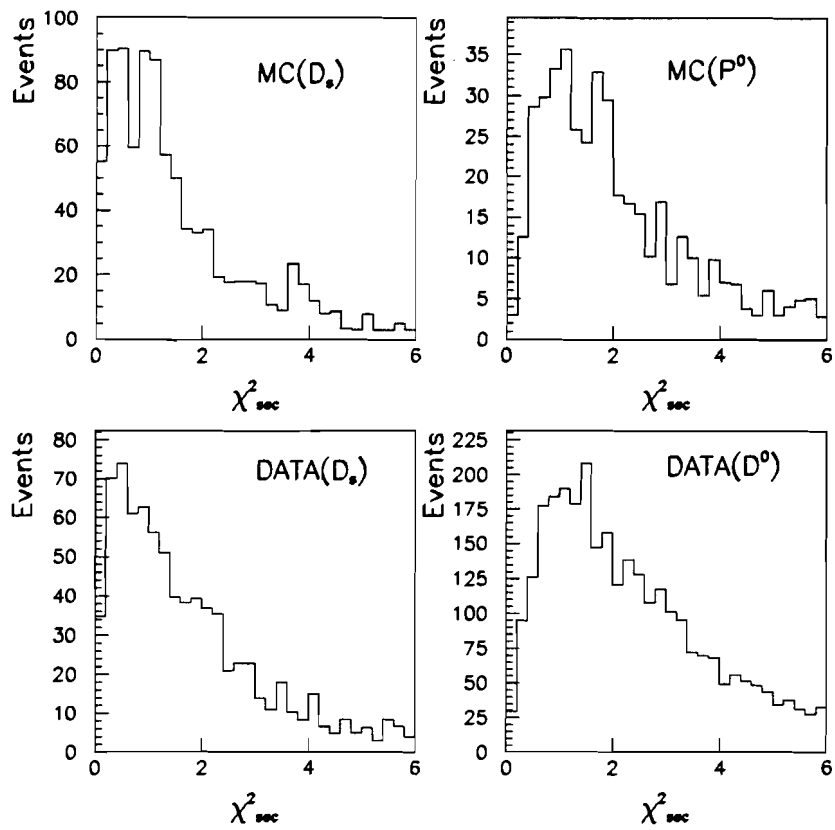

Figure 4.5: Distributions of χ^2_{sec}, for the D_s MC and data signals, for the pentaquark MC signal and for the $D^0 \rightarrow K\pi\pi\pi$ signal from data.

In order to make a more quantitative estimate of the effect on the efficiency, the χ^2_{sec} distributions from MC were normalized to have the same number of events as in the distributions from data. The χ^2_{sec} distributions from data were then divided by the normalized distributions from MC. This was repeated for all variables characterizing the 3-prong decay of the D_s and for the 4-prong decay of the pentaquark from MC in comparison to the D^0 decay from data. These ratios of χ^2_{sec} distributions, for 3- and 4-prong decays, are shown in Fig. 4.6(a) and 4.6(b), respectively. The double ratio, calculated as the ratio between these two distributions and shown in Fig. 4.6(c), gives the sensitivity of the value calculated in Eq. 5.1 to changes in the applied cut on the χ^2_{sec} variable.

The denominator of Eq. 5.1 is essentially the Yield in the D_s signal from data divided by the efficiency to get this signal, as calculated from MC. To check the sensitivity of this expression to changes in cut values I calculated it as a function of a "running" cut value on the variable being tested. Fig. 4.6(d) shows Yield(D_s *Signal*)$/\varepsilon_{D_s}$ calculated for a "running" cut value on χ^2_{sec}. Note that above a certain value the ratio is constant and therefore not sensitive to variation of the cut.

As we wanted to reduce the sensitivity of the search to variations in cut values we

took precaution that:

- For the chosen cut, the double ratio between variable distributions would be close to one and would not fluctuate too much.
- The expression Yield(D_s *Signal*)/ε_{D_s} would be stable when the chosen cut value is varied. This consideration implied that all vertex definition requirements (quality and separation), listed in Table 5.3 and discussed in sec. 5.2, were in the flat region of plots like Fig. 4.6(d).

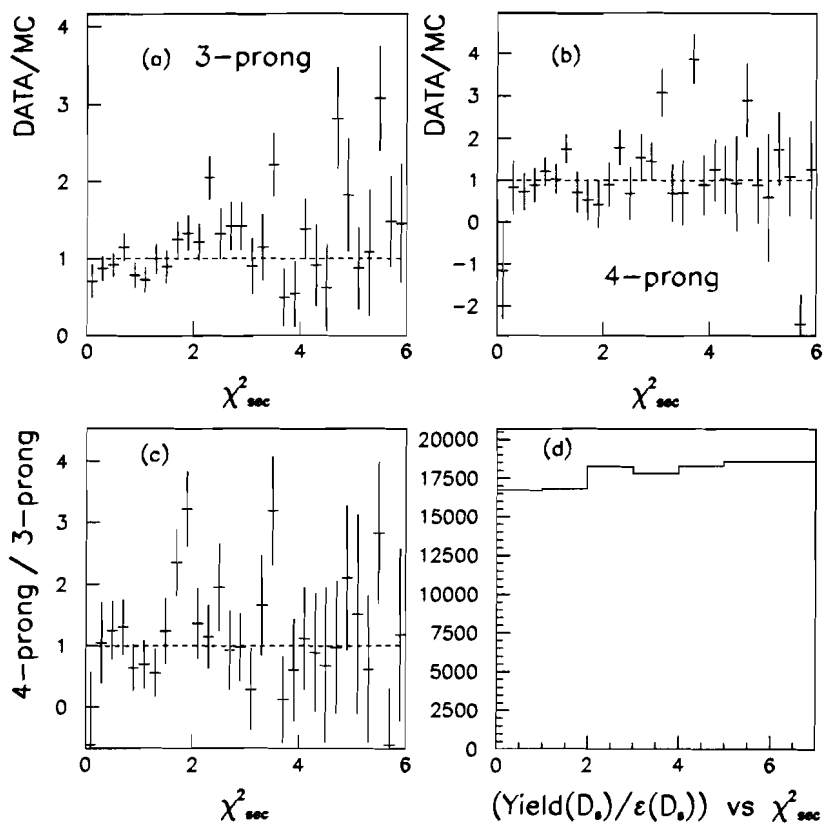

Figure 4.6: Ratios of χ^2_{sec} distributions from the data signal and from the normalized MC signal, for: (a) 3-prong decays of D_s, (b) 4-prong decays. The χ^2_{sec} distribution of the 4-prong decay $D^0 \rightarrow K\pi\pi\pi$ from data is divided by the normalized distribution for the pentaquark MC signal. (c) The double ratio of the distributions in (a) and (b). (d) The Yield(D_s *Signal*)/ε_{D_s} as a function of a "running" cut value on χ^2_{sec}.

Comparison of the kinematic variable: the Pt2dk

The different kinematics of the D_s decay as opposed to the pentaquark decay causes the Pt2dk distributions to be quite different. (see sec. 3.2.1). Pt2dk distributions for D_s signals from MC and data are shown in Fig. 4.7(a) and 4.7(b), respectively. It is noted that the MC(D_s) reproduces the data quite well. A comparison of the

Pt2dk distribution, plotted for D^0 signals from MC and data in Fig. 4.7(c) and 4.7(d), shows that it is reproduced well also by the MC(D^0). The Pt2dk distribution for the pentaquark decay is not expected to be identical to that of a D^0 decay since the Q value of the two decays is different (about 860 MeV/c^2 for the decay $D^0 \to K\pi\pi\pi$, compare to less than 800 MeV/c^2 for the decay $P^0_{\bar{c}s} \to \phi\pi p$.) The Pt2dk distribution of the pentaquark MC signal is shown in Fig. 4.7(e). It can be seen that it is indeed different from the distributions of the D_s and D^0 signals. However, since these are reproduced well by the MC, we believe that the MC simulates well this variable for the pentaquark decay too.

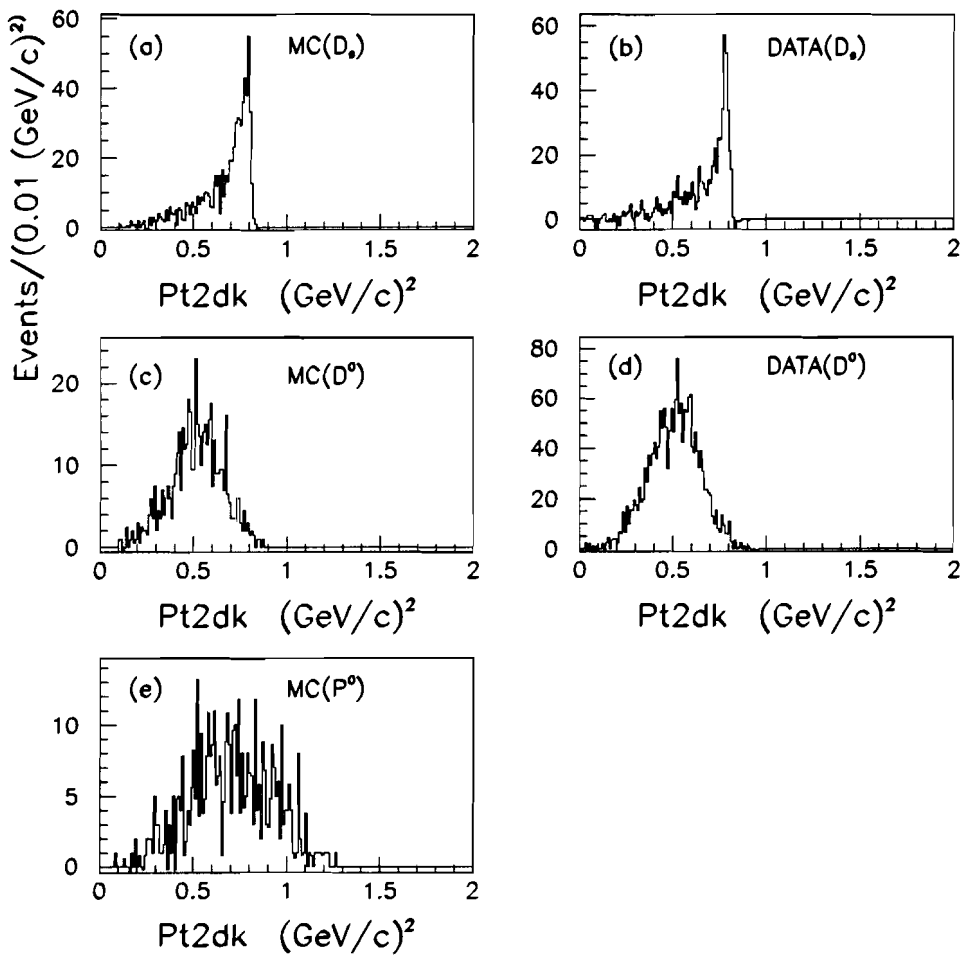

Figure 4.7: Distributions of Pt2dk for: (a) the decay $D_s \to \phi\pi$ from Monte Carlo, (b) the same decay from data, (c) the decay $D^0 \to K\pi\pi\pi$ from Monte Carlo, (d) the same decay from data, (e) the decay $P^0_{\bar{c}s} \to \phi\pi p$ from Monte Carlo.

Comparison of the proton identification variable: C(p)

Another difference between the D_s and pentaquark analyses is the additional proton in the pentaquark decay. The Čerenkov probability function assigned to the proton

track - C(p) - is the tool used for the proton identification. As the Čerenkov counters could identify protons only in a certain momentum region the probability values depended also on the track momentum. I used a sample of $\Lambda \rightarrow \pi p$ as a source for protons from data, and compared the efficiency of the cut on C(p) from MC($P^0_{\bar{c}s}$) and data. The data set included ~57330 Λs. Fig. 4.8 shows proton momentum distributions from the Lambda sample and from the pentaquark MC. The protons from pentaquark decays carry a higher average momentum than the protons from Lambda decays.

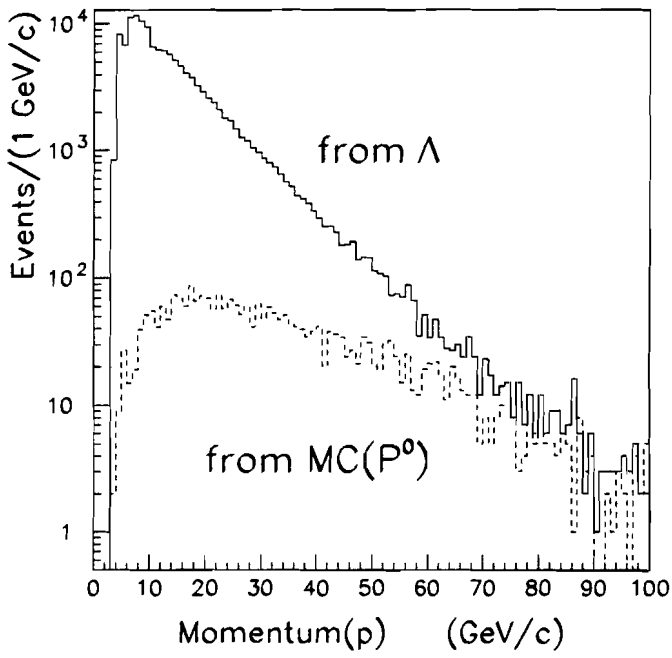

Figure 4.8: Momentum distributions of protons from data ($\Lambda \rightarrow \pi p$ sample) and from MC($P^0_{\bar{c}s}$).

The efficiency of the cuts on C(p) was calculated in momentum bins defined by the sensitivity of the Čerenkov counter. The Čerenkov should identify well protons with momentum between 21 to 75 GeV/c (see Table 2.8 and discussion in sec. 2.1.6). In this region we do not expect to see an ambiguity K/p peak on the C(p) scale. However, such a peak does appear for proton momenta between 21 to 40 GeV/c, both in data and MC. Fig. 4.9(a) shows the distribution of C(p) from data, with the apparent K/p ambiguity peak. Histograms (b) and (c) in this figure show proton momentum distributions from Λ data and pentaquark MC for tracks in the K/p ambiguity peak. Most of the protons in the ambiguity peak carry momenta between 6-21 GeV/c. Nevertheless, protons having momenta between 21-40 GeV/c do not necessarily belong to background events as they produce a good Λ signal, as shown in Fig. 4.10.

The explanation is related to the response of the Čerenkov counters. In the 21-40 GeV/c momentum region the proton was well identified if none of the Čerenkov

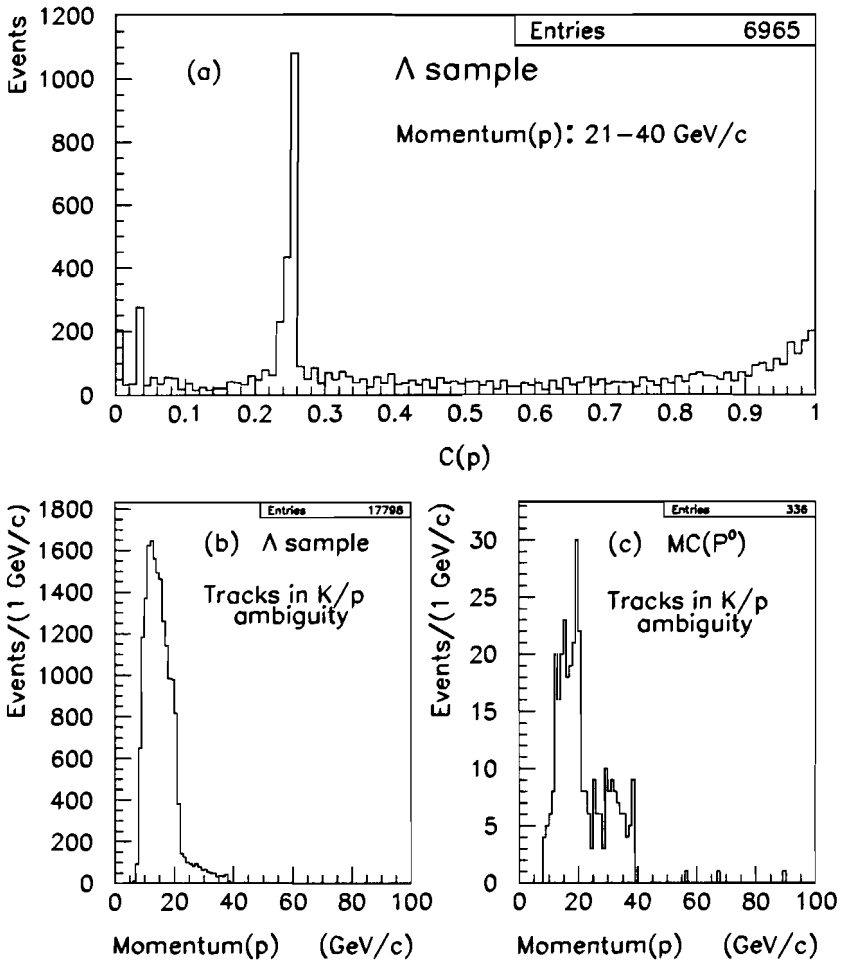

Figure 4.9: (a) A distribution of C(p) that shows an ambiguity peak for protons from data having momenta between 21 to 40 GeV/c. (b) Momentum distribution of proton candidates in the K/p ambiguity peak from data. (c) Momentum distribution of proton candidates in the K/p ambiguity peak from MC.

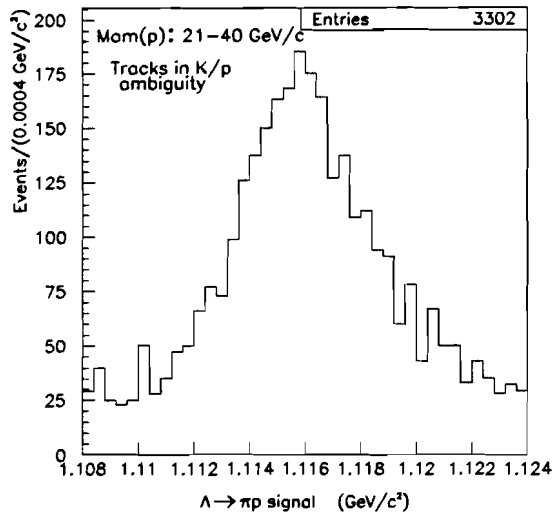

Figure 4.10: A $\Lambda \rightarrow \pi p$ signal from data, for protons in the ambiguity peak having momenta between 21 to 40 GeV/c.

counters gave any light. If Č1 was noisy (could be due to high multiplicity) then the (Č1,Č2) signal looked like that of an expected kaon. However, the amount of light detected did not fit the predicted amount of light produced by a kaon track and the code gave a probability in the K/p ambiguity peak. If both Č1 and Č2 were noisy this particle could be mistaken to be a pion and could show in the π/p ambiguity peak (0.05) or in the a-priori peak on the C(p) scale.

The study was binned in four momentum bins and five cut values on C(p) (see Table 4.2). The cut values used are:

C(p)	> 0.038	- below the a-priori peak
	>0.05	- above the a-priori peak
	>0.2	- below the K/p ambiguity peak
	>0.26	- above the K/p ambiguity peak
	>0.9	- close to definite ID.

This study was done separately for two bins of the decay vertex Z position (Z_{sec}). The efficiencies were calculated for Λs decaying within the first 20cm, and for Λs decaying at a larger distance. The efficiency was calculated as the ratio between the number of events in the Λ signal after and before the cut was applied. Table 4.2 lists efficiencies calculated for the cuts on C(p) relative to a basic cut of C(p)>0.038 which was required in the pentaquark basic analysis program. The efficiency was calculated in four momentum bins, where the fourth was 40-55 GeV/c instead of 40-75 GeV/c, since the high momentum events added mostly to the background and made it difficult to find the Λ events there. The cut efficiency in this momentum bin (40-55 GeV/c) was calculated relative to the C(p)>0.05 cut (above the a-priori). This was done because in that momentum region there was no K/p ambiguity peak, making the calculated efficiency very sensitive to the number of events in the a-priori peak

Momentum (GeV/c) C(p)>	6-11	11-21	21-40	40-55	Z_{sec}
0.038	1639	1571	573		<20cm
	15085	19112	6973		>20cm
	60	291	598		MC
0.05	.77 (.02)	.959(.06)	.92 (.04)	61	<20cm
	.839(.009)	.991(.027)	.982(.015)	587	>20cm
	.7 (.06)	.95 (.01)	.88 (.01)	253	MC
0.2	.46 (.03)	.882(.05)	**.87** (.04)	.9 (.19)	<20cm
	.536(.008)	.913(.024)	.901(.012)	.96(.16)	>20cm
	.4 (.06)	.81 (.02)	**.75** (.02)	.83(.02)	MC
0.26			.54 (.04)	.82(.18)	<20cm
			.626(.013)	.95(.16)	>20cm
			.51 (.02)	.81(.03)	MC
0.9			.18 (.03)	.28(.15)	<20cm
			.196(.009)	.63(.12)	>20cm
			.2 (.02)	.4 (.03)	MC

Table 4.2: Efficiencies and their errors in brackets calculated for different cuts on C(p) in four momentum regions. The numbers listed in the first line are the number of events in the signal with the requirement of C(p)>0.038. The three numbers in each box are related to Λs decaying within 20cm from the targets, in farther location, and to pentaquarks in the MC signal.

and below (a region that contains mostly background events). Three efficiency values are listed in each momentum bin for each cut. The first two are efficiencies calculated from data for Z_{sec} <20cm and Z_{sec} >20cm, and the third is the efficiency calculated from the pentaquark MC. The errors of the efficiency values are listed in brackets. The numbers listed for the C(p)>0.038 cut are the number of events in each momentum region. Again, the first and second ones refer to Z_{sec} <20cm and Z_{sec} >20cm respectively and the third is the number of pentaquark MC events.

Our conclusions from this study were:

1. The efficiencies calculated for Λs decaying closer to the primary (<20cm) are always smaller than those calculated for farther decaying Λs.

2. We expected the efficiency calculated from the pentaquark MC to be more similar to the efficiency calculated for Λs which decayed closer to the primary (<20cm) than to those which decayed farther downstream. This is because the pentaquark is expected to decay close to the primary vertex. The table shows that the efficiencies calculated from MC($P^0_{\bar{c}s}$) are even smaller than those calculated for Λs decaying relatively close to the primary vertex, but in most cases these efficiencies are consistent with each other within errors. The largest difference in efficiencies between MC and data is observed for the cut of C(p)>0.2 in the 21-40 GeV/c momentum region: $\sim$ 14%.

Summary

In conclusion, not all variable distributions were described well by the Monte Carlo. The deviations were usually similar for the pentaquark and D_s decays, reducing the systematic uncertainty in the ratio of efficiencies. Nevertheless, since discrepancies existed, the definition of cut values was not based solely on the MC in variables that were not described well by it (see also sec. 5.2). However, since the efficiencies of cuts were calculated using MC, the discrepancies between MC and data were taken into account in the systematic uncertainty calculations of the final results, as explained in details in section 7.2.

Chapter 5

Analysis

5.1 Method of analysis

Generally, a decay mode is measured by its production cross section (σ) multiplied by the branching fraction (B) of the specific decay. In order to determine the value of $\sigma \cdot B$ it is necessary to know well the flux, the target factors and the detection efficiency. The latter is very sensitive to the reliability of the Monte Carlo simulation used to calculate this efficiency. Many systematic uncertainties can be eliminated or reduced by the evaluation of $\sigma \cdot B$ relative to a $\sigma \cdot B$ of another, well known, decay. Such an evaluation becomes also much less sensitive to the details of the Monte Carlo reliability, in particular if the two considered decay modes have much in common. In the particular case of the pentaquark such an analysis is sensible also since the various predictions of the pentaquark production cross section are relative to that for producing another charm particle, the D_s (see sec. 1.4).

I have searched for the pentaquark via its $P^0_{\bar{c}s} \rightarrow \phi\pi p$ decay, where the ϕ subsequently decays to K^+K^-. The sensitivity of this search was normalized to the similar $D_s^{\pm} \rightarrow \phi\pi^{\pm}$ decay. These are convenient decay modes to detect because all decay products are charged, and because the narrow ϕ signal allows an effective rejection of K^+K^- background. The analysis programs used to select pentaquark and D_s candidates were essentially identical to the sub-sub-stripping routines (see sec. 3.2.3), but they applied two additional mild cuts on topological variables: $SIGMA > 0$. and $ISO > 0.0001$cm and on the kinematic variable: $Pt2dk > 0.2$ (see sec. 3.2.1 for definitions of these variables).

The ratio between $\sigma \cdot B$ for the pentaquark and D_s decays can be expressed in the following way:

$$\frac{\sigma_{P^0_{\bar{c}s}} \cdot B(P^0_{\bar{c}s} \rightarrow \phi\pi p)}{\sigma_{D_s} \cdot B(D_s \rightarrow \phi\pi)} = \frac{\frac{N(\phi\pi p)}{\varepsilon(P^0_{\bar{c}s} \rightarrow \phi\pi p)}}{\frac{N(D_s \rightarrow \phi\pi)}{\varepsilon(D_s \rightarrow \phi\pi)}}, \tag{5.1}$$

where $N(\phi\pi p)$ refers to the number of data events in a potential pentaquark signal or to the 90% confidence level upper limit based on a comparison between the expected background level and the observed number of events [38]. The quantities $N(D_s)$, $\varepsilon(P^0_{\bar{c}s})$ and $\varepsilon(D_s)$ are the D_s yield and the detection efficiencies for $P^0_{\bar{c}s} \rightarrow \phi\pi p$ and $D_s \rightarrow \phi\pi$, respectively. The detection efficiencies for both pentaquark and D_s decays

are defined as:

$$\varepsilon = \frac{S}{N_{generated}}, \tag{5.2}$$

where S is the number of events in the Monte Carlo signal, and $N_{generated}$ is the number of events generated by the Monte Carlo. The yield in the D_s signal and the detection efficiencies are calculated for a chosen set of selection criteria.

In the process of optimizing the selection criteria (cuts) for the pentaquark search we used the Monte Carlo events and two thirds of E791 data. In order to optimize the significance of a potential signal in the $\phi\pi p$ invariant mass spectrum we used a technique which helped to define the best set of cuts without creating an artificial bias. Section 5.2 describes this procedure and how we interpreted its results. We chose the cuts in an iterative process. We first ran the optimization procedure without demanding any cuts except for those already required by the analysis program (analyser), and defined a set of "crude cuts". Then, we made a more delicate choice of cuts. For this purpose we ran the optimization procedure twice more:

1. For each variable subject to check the optimization procedure required the "crude cuts" on variables not belonging to the same "family" (see sec. 4.2.2). This way it could use cleaner signals without the effect of correlations between variables in the same "family".

2. In the next step, the optimization was repeated for each variable with other variables in the same "family" subject to the cut values optimized in the former stage. This way we fine-tuned the cut values while taking into account correlations between variables in the same "family".

In order to make the ratio in equation 5.1 less sensitive to changes in cut values, we took caution to apply selection criteria in stable regions of ratios between pentaquark and D_s efficiencies, and Yield/efficiency of the D_s, as explained in section 4.2.2.

We used the optimization procedure to define selection criteria mainly to be applied on topological variables, but also to define the proton identification criterion and the cut on Pt2dk (kinematic variable). The optimization process of the last two cuts are described in sec. 5.4.2 and 5.5, respectively. The definition of kaon identification criteria was done differently, as described in sec. 5.4.1. The chosen set of cuts received the name "set 1".

The introduction of another topological variable (MAXRAT_i) into the analysis in a later stage made it necessary to re-optimize the cuts on other topological variables as well. Sec. 5.3 describes this process in detail, also as a demonstration of the optimization technique. The modified cuts were the final selection criteria applied to the topological variables. These criteria, together with the other cuts of "set1" (particle ID and kinematic), and background reduction cuts, were named "UL96 set". Background reduction cuts included general cleaning requirements, as described in sec. 5.6, and a removal of misidentified decays (discussed in chapter 6). The selection criteria of "set 1" and the "UL96 set" are listed in Table 5.3. The efficiencies of these criteria and the related systematic uncertainties are discussed in chapter 7.

5.2 The optimization procedure

The optimization procedure examined how selection criteria applied to variables affected the number of signal (S) and background (BG) events. It worked in two stages:

- First, it produced distributions of the tested variables. The distributions were produced for the signal and background regions of the particle being studied, in the same manner as described in sec. 4.2.2.

- In the second stage it deduced the number of signal and background events that survived a "running" cut value applied to the variable being tested. Two quantities were then calculated: *sensitivity* and *efficiency*, defined as:

$$\begin{aligned} \textit{sensitivity} &= \frac{S}{\sqrt{BG}}, \\ \textit{efficiency} &= \frac{S_{cut}}{S_{no\ cut}}, \end{aligned} \tag{5.3}$$

  where S_{cut} and $S_{no\ cut}$ are the number of events in the signal after and before a cut is applied, respectively. The sensitivity and the efficiency were calculated as a function of a "running" cut on each variable, and served as a guidance tool in the definition of selection criteria. we chose cut values that resulted in high sensitivity values, but which did not harm the efficiency too much (see sec. 5.3).

The signals used by the optimization procedure were taken from several sources. The main source was the pentaquark signal from MC. Optimization results obtained with the simulated pentaquark signal were compared to the results obtained using available data signals in order to check consistency. The signals taken from data were:

- A ϕ signal from ϕ-filtered data was used in the optimization of kaon identification criteria. These ϕs were selected independently from the $\phi\pi p$ sample (see sec. 3.2.2).

- A $D^0 \rightarrow K\pi\pi\pi$ signal from data helped in the optimization of parameters defining the 4-prong decay vertex.

When the optimization procedure used the pentaquark signal from MC, background events were taken from the $\phi\pi p$ invariant mass spectrum from data, in a mass region outside the 2.75 to 2.91 GeV/c^2 range. The pentaquark could exist only within this range (see sec. 1.1), hence, the region outside it could serve as a pure background for the pentaquark search. When the optimization procedure used other sources of signals, background events were taken from the mass "wings" of these signals. The "wings" were defined as the range of invariant mass where no signals were observed. The signals of $P^0_{\bar{c}s} \rightarrow \phi\pi p$ from MC and $D^0 \rightarrow K\pi\pi\pi$ from data are shown in Figs. 5.1(a) and 5.1(b), respectively. The D^0 signal consists of events that have been selected by the pentaquark strip and analyser routines, meaning that it contains only a small fraction of D^0 particles detected by E791. Fig. 5.1(d) shows the background spectrum of $\phi\pi p$ from data. The ϕ–signal, from the ϕ–filtered data, is shown in Fig. 5.7 as part of the discussion of optimizing the kaon identification criteria (section 5.4.1).

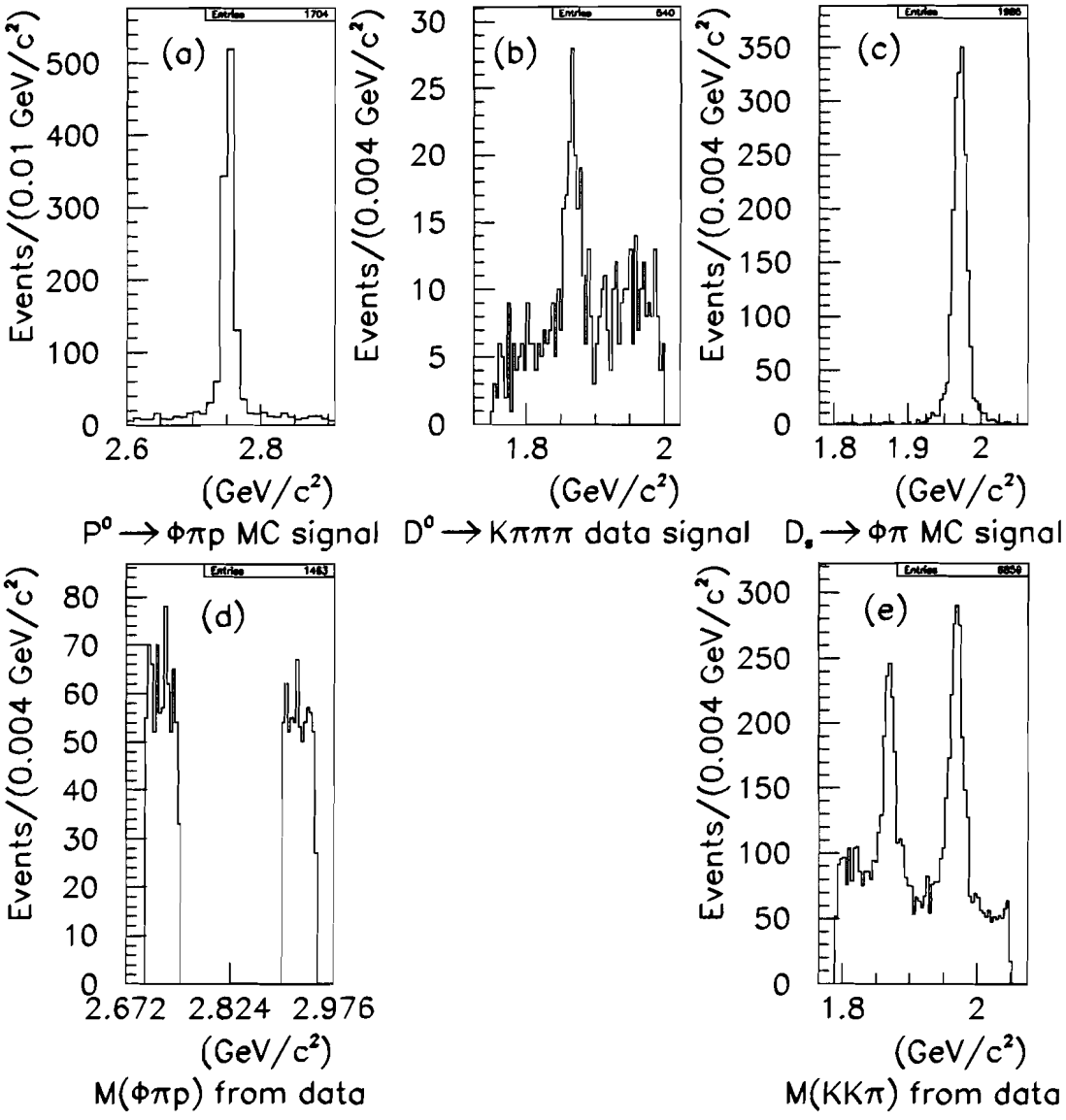

Figure 5.1: (a) The simulated $P^0_{\bar{c}s} \to \phi\pi p$ signal. (b) Invariant mass spectrum of $K\pi\pi\pi$ from data, showing the D^0 signal. (c) The simulated signal of $D_s \to \phi\pi \to K^+K^-\pi$. (d) Invariant mass spectrum of $\phi\pi p$ from data, showing events that are considered as background by the optimization procedure. (e) Invariant mass spectrum of $\phi\pi \to K^+K^-\pi$ from data. The right peak is the $D_s^\pm$ signal. The left peak arises from Cabibbo-suppressed $D^\pm$ decays.

An optimization procedure was activated for the normalization sample of $D_s \rightarrow \phi\pi$ decays as well. The signal events were taken from a Monte Carlo simulation of that D_s decay. The background was taken from the closest bins on both sides of the peak from data, normalized to give the number of background events in the peak region. Fig 5.1(c) and 5.1(e) show the mass spectra of $D_s \rightarrow \phi\pi$ from MC and data, respectively, plotted with the analyser cuts. Eventually, we applied equal selection criteria to the $\phi\pi p$ and $\phi\pi$ data, in the common part of the two analyses, to minimize the systematic uncertainties.

5.3 Four-prong vertex definition cuts

Selection criteria on vertex definition variables were chosen using the optimization procedure and following the considerations discussed in sec. 5.1. They included cuts on the variables: $SIGMA$, SDZ, χ^2_{sec}, χ^2_{pri}, DIP, ISO, RAT and $RAT_i/AVGR$. These cuts, together with cuts on particle ID variables and on the kinematic variable - Pt2dk, are listed in Table 5.3 and named "set 1".

The MAXRAT$_i$ variable was an exception as it was examined in a relatively late stage of the analysis. Nevertheless, the process of optimizing the cut on MAXRAT$_i$ demonstrates the recursive nature of the optimization procedure and as such, I describe it here as an example.

The optimization was done using two signals. One was the pentaquark MC signal (Fig. 5.1(a)) and the other was the $D^0 \rightarrow K\pi\pi\pi$ signal from data (Fig. 5.1(b)). The background for the pentaquark signal was taken from data of $\phi\pi p$ (Fig. 5.1(d)). The background for the D^0 signal was taken from its "wings" in the same mass plot. The optimization procedure examined events with 4-prong decays selected by the vertex-definition cuts of "set 1", except for the cuts on χ^2_{sec}, DIP and RAT. The cuts on these three variables were loosened to the values required by the analyser because they could be correlated with MAXRAT$_i$ and as a consequence a cut applied to them could be an indirect cut on MAXRAT$_i$. At its first stage, the optimization procedure produced distributions of MAXRAT$_i$ from signal and background regions of D^0 and pentaquark decays. Fig. 5.2(a) shows the shapes of MAXRAT$_i$ distributions from the D^0 signal (solid) and its background (dashed). Fig. 5.2(b) shows the MAXRAT$_i$ distributions from the pentaquark MC signal (solid) and its background from data (dashed). It can be seen that the shape of the distributions characterizing the signals is different from the shape of the distributions from background. In the second stage the efficiency and sensitivity were calculated (see Eq. 5.3) for a "running" cut on MAXRAT$_i$.
Figs. 5.2(c) and 5.2(d) show the efficiency plots calculated using signals of D^0 and pentaquark, respectively. Figs. 5.2(e) and 5.2(f) show the sensitivity plots calculated using these signals and their background from $K\pi\pi\pi$ and $KK\pi p$ data, respectively.

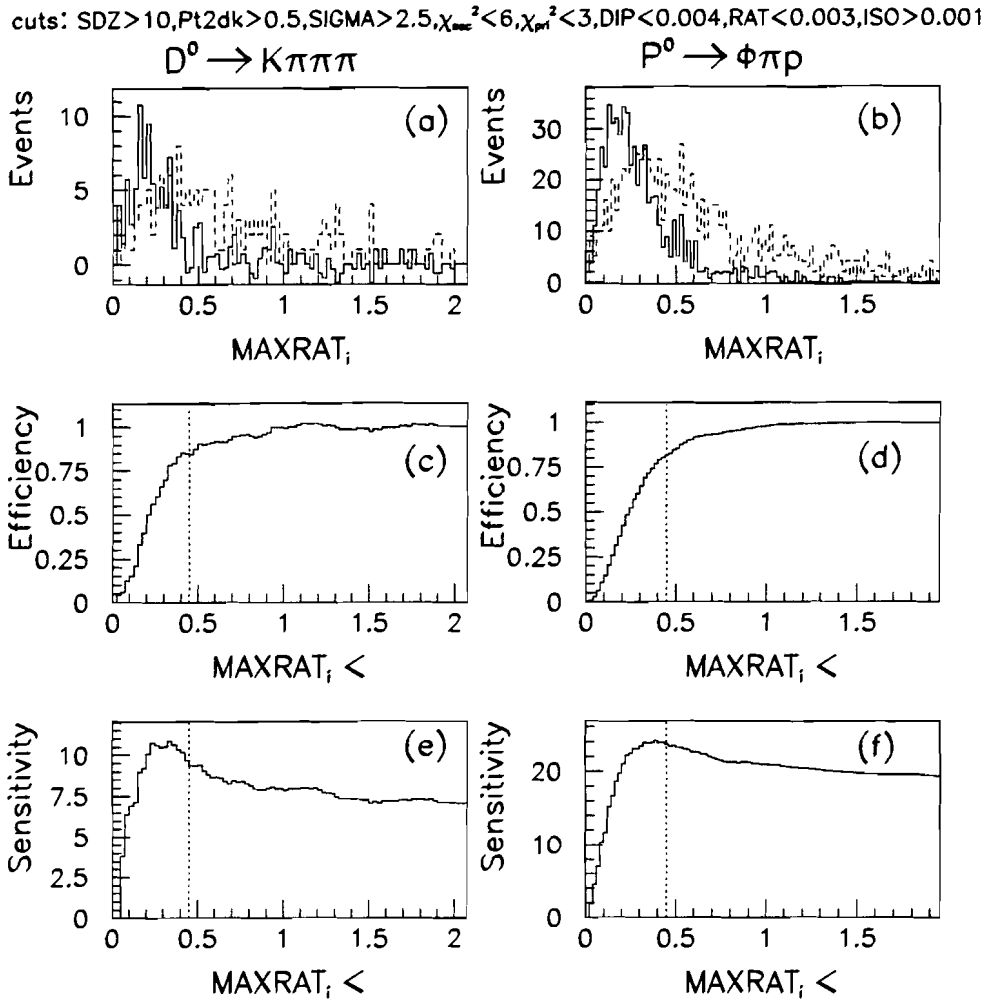

Figure 5.2: (a) Maxrat$_i$ distributions from the $D^0 \rightarrow K\pi\pi\pi$ signal (solid line) and from its background (dashed line). (b) Maxrat$_i$ distributions from the MC signal of $P^0_{\bar{c}s} \rightarrow \phi\pi p \rightarrow KK\pi p$ (solid line) and from the $KK\pi p$ background spectrum (dashed line). The efficiencies as a function of the "running" cut value on MAXRAT$_i$ are shown in (c) for the D^0, and in (d) for the pentaquark. The sensitivities as a function of this "running" cut value are shown in (e) for the D^0 and in (f) for the pentaquark. The dotted lines on histograms (c) to (f) represent the chosen cut value: MAXRAT$_i$ < 0.45.

The cut value on MAXRAT$_i$ was determined to be: <0.45. Applying this selection criterion would improve the sensitivity by $\sim$ 30% in comparison to not requiring it, and would result in a loss of $\sim$ 15% in the efficiency. We chose not to require a tighter cut, of MAXRAT$_i$ < 0.35, even though it would result in a better sensitivity. This is because the efficiency of this cut drops to 75%, and, more crucial - it changes rapidly near MAXRAT$_i$ < 0.35 and could cause the result to be unstable.

The next step was to re-define the selection criteria. We repeated the optimization

process for χ^2_{sec}, DIP and RAT, when an additional cut of MAXRAT$_i$ <0.45 was applied. Efficiencies and sensitivities were calculated again for "running" cut values on these variables. Fig. 5.3 shows the efficiency (left) and sensitivity (right) plots for the χ^2_{sec}, DIP and RAT variables. The required cuts were the same as in the optimization process of MAXRAT$_i$ but with the additional cut of MAXRAT$_i$ <0.45.

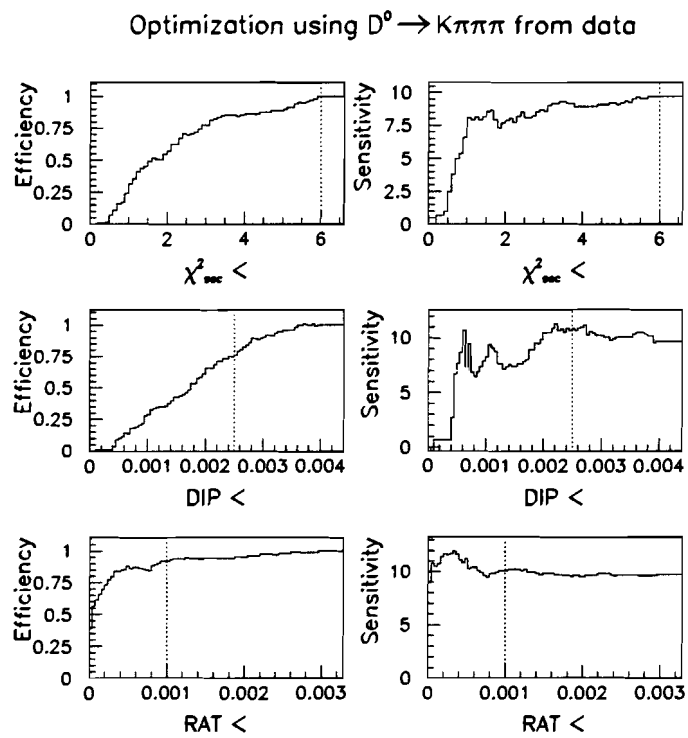

Figure 5.3: Results from a re-optimization process done for the χ^2_{sec}, DIP and RAT parameters, while requiring the additional MAXRAT$_i$ <0.45 cut. On the left: the efficiencies as a function of the "running" cut value on each parameter. On the right: the sensitivities as a function of these "running" cut values. The dashed lines represent the chosen cut values.

Motivated by these efficiency and sensitivity plots, we concluded that:

- A cut on χ^2_{sec}, tighter than the requirement in the analyser program, would not improve the sensitivity. Thus, we decided not to apply a cut on χ^2_{sec}, tighter than $\chi^2_{sec} < 6$.
- The cuts on DIP and RAT should remain as defined within "set 1" ($DIP <$ 0.0025 .and. $RAT < 0.001$). A tighter cut on RAT would improve a little the sensitivity but we felt that it would be too tight.

We called this new set of cuts: "set 4". The only difference between this set and "set 1" is the additional cut on the MAXRAT$_i$ variable and the more open cut on χ^2_{sec}.

Figs. 5.4(a) and 5.4(b) show the D^0 data signal plotted with the requirements of "set 1" and "set 4", respectively.

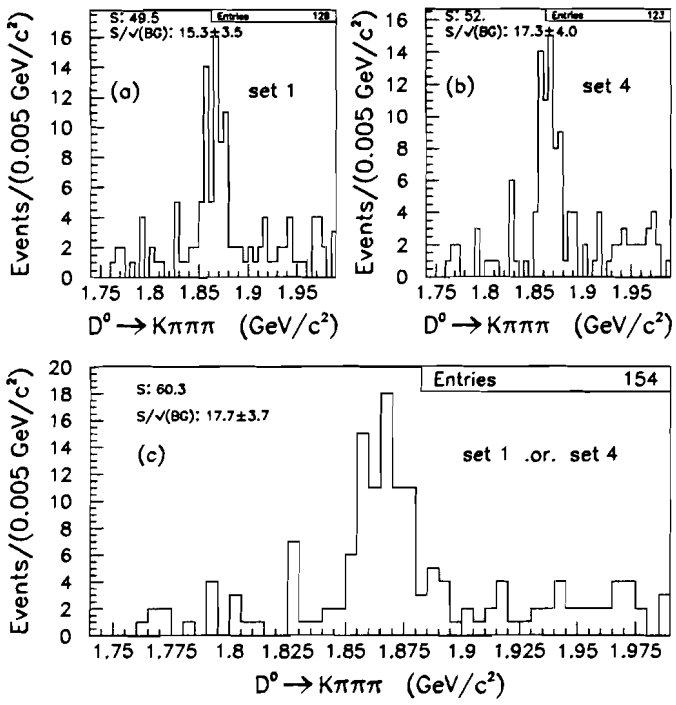

Figure 5.4: D^0 signals from data, plotted with the requirements of (a) "set 1", (b) "set 4" and (c) the combination: "set 1".or."set 4". The yield in the D^0 signal and its sensitivity are printed on each of the histograms.

The sensitivity gained by "set 4" (17.3±4.0) is essentially the same within errors as the one gained by "set 1" (15.3±3.5). The yield in the D^0 signal is about the same (52 with "set 4" compare to $\sim$ 50 with "set 1"). It is interesting to note that the two D^0 signals, plotted with "set 1" or "set 4" requirements, do not consist of the same events necessarily. In fact, $\sim$ 20% of the events are not common. It means that these two sets of cuts choose somewhat different events, both with about the same quality since the sensitivity and the yield are very similar. In order to collect the good events into a combined signal while keeping the sensitivity in its best value we defined a combined cut: "set 1".or."set 4", and applied it to the $K\pi\pi\pi$ data. The resulting spectrum is shown in Fig. 5.4(c). Clearly, there is a gain of $\sim$ 20% in the yield of the D^0 signal, from $\sim$ 50 D^0 events selected by each set of cuts separately, to $\sim$ 60 events selected by the combined cut, while the sensitivity remains the same. Based on this study we decided to apply the "set 1".or."set 4" cut to the $\phi\pi p$ data set. In fact, most of the cuts in the two sets are identical, and the .or. is defined only between the cut on χ^2_{sec} to the cut on MAXRAT$_i$:

$$\chi^2_{sec} < 3 \ \ .or. \ \ MAXRAT_i < 0.45.$$

5.4 Particle identification cuts

5.4.1 Kaon Čerenkov cut optimization

In the analysis of $P^0_{\bar{c}s} \rightarrow \phi\pi p \rightarrow K^+K^-\pi p$ we wanted to identify a ϕ signal with the ϕ decay products identified as kaons. In order to study kaon identification (KID) cuts we used a large sample of ϕ events from a ϕ-filtered run. The ϕ-filtered data were stripped by a ϕ-strip and written to a different output stream than the data used for the pentaquark search. It ensured that the ϕ events in the two data sets were selected independently. In order to get a relatively clean ϕ signal for KID study, a Čerenkov cut of C($K1$) > 0.7 was applied. The resulting ϕ peak was studied in momentum bins of the second kaon. For each momentum region several cuts were tried and the values of efficiency and sensitivity (Eq. 5.3) evaluated. The results are summarized in Table 5.1.

C($K2$)	Momentum($K2$) (GeV/c)				
	< 6	6 - 11	11 - 21	21 - 40	40 - 75
Analyser Cuts	-	40.7±1.2	12±0.4	26.5±0.8	-
> 0.13	-	0.29±0.02	0.9±0.04	0.61±0.03	-
	-	16.5±0.8	15.3±0.6	24.3±1.	-
> 0.2	-	0.29±0.02	0.9±0.04	0.59±0.03	-
	-	20.6±1.1	16.5±0.6	25.1±1.	-
> 0.5	-		0.83±0.04	0.47±0.03	-
	-		18.4±0.7	23.2±1.1	-
> 0.7	-		0.79±0.04	0.36±0.02	-
	-		21.3±0.9	19.9±1.	-
> 0.77	-	-	-	-	-
	-	-	-	-	-

Table 5.1: Efficiencies (upper raws) and sensitivities (lower raws), calculated in momentum bins of $K2$. For the "Analyser cuts" line only the sensitivity is listed.

According to the table, the best sensitivity is obtained for the following combination of cuts on C($K2$):

	MOM($K2$):	6-11 GeV/c	.and.	(no cut on C($K2$))
.or.	MOM($K2$):	11-21 GeV/c	.and.	C($K2$)>0.7
.or.	MOM($K2$):	21-40 GeV/c	.and.	C($K2$)>0.2

However, the strong cut C($K1$)>0.7 applied to one of the kaons for all momenta, defines a limited momentum region for both kaons because the two kaon momenta are correlated. Indeed, from the Table it can be seen that there are no ϕ's constructed from tracks with momenta below 6 GeV/c or above 40 GeV/c. The correlation is seen also in Fig. 5.5, which shows the momentum distribution for each of the kaon candidate tracks and a two dimensional plot of the two kaon momenta.

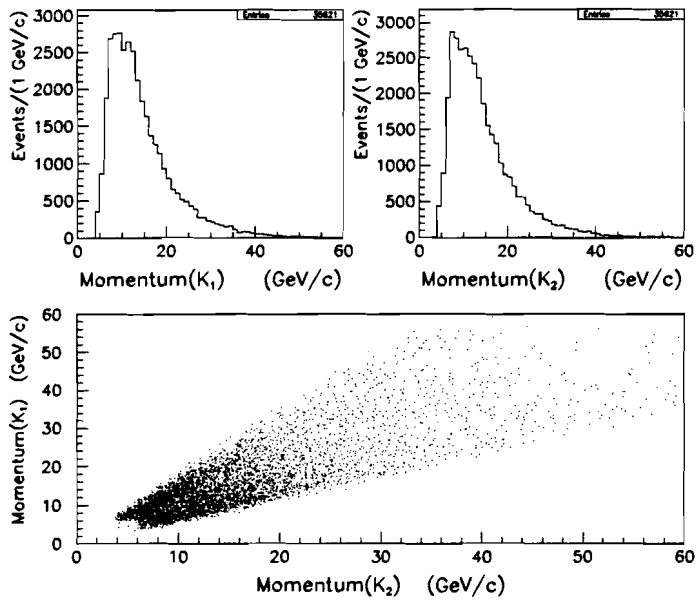

Figure 5.5: Top: Momentum distributions of the two kaon candidate tracks in the ϕ sample. Bottom: the correlation between the momenta of the two kaon candidates.

Thus, the combination of cuts, recommended by Table 5.1, is not necessarily the optimal one to require within the pentaquark analysis in order to get the best sensitivity to the ϕ signal. This consideration led us to require a different and more "simple" momentum dependent cut on the Čerenkov probability of the two kaons:

MOM($K1, K2$): 6-40 GeV/c .and. C($K1, K2$)>0.2,

where MOM($K1, K2$) is the momentum of each of the two kaons and C($K1, K2$) their Čerenkov probabilities. The product of the Čerenkov probabilities: C($K1$)•C($K2$) > 0.05 was required already in the early filter and strip stages of data reduction, and had to be therefore required all along the analysis.

In order to check in a more quantitative way if this KID cut is the optimal cut for the pentaquark analysis, the ϕ's from the $\phi\pi p$ candidate events were plotted with different combinations of momentum dependent cuts on C($K1, K2$). Fig. 5.6 shows five invariant mass spectra of K^+K^-, with the following cut combinations:

(a) The cuts required in the analyser stage.

(b) The suggested "simple" KID cut.

(c) The combination of cuts recommended by Table 5.1.

(d)
MOM($K1, K2$): 6-11 GeV/c .and. C($K1, K2$)>0.2 .or.
MOM($K1, K2$): 11-21 GeV/c .and. C($K1, K2$)>0.7 .or.
MOM($K1, K2$): 21-40 GeV/c .and. C($K1, K2$)>0.2

	MOM($K1, K2$):	6-11 GeV/c	.and.	C($K1, K2$)<0.2	.or.
(e)	MOM($K1, K2$):	11-21 GeV/c	.and.	C($K1, K2$)>0.7	.or.
	MOM($K1, K2$):	21-40 GeV/c	.and.	C($K1, K2$)>0.2	

Table 5.1 suggests not to demand any cut on C(K) for MOM(K) between 6 to 11 GeV/c. Kaon candidate tracks having momenta in this region were divided into two complementary groups: one with C(K)<0.2, and the other with C(K)>0.2. Figs. 5.6(d) and 5.6(e) show these two groups of events, plotted together with the events selected by the cuts on C(K) in other momentum regions. The number of events in the ϕ signal (after background subtraction) within the mass region: 1.016-1.023 GeV/c^2, and the sensitivity, are listed on each one of the histograms in Fig. 5.6. The number of background events was taken from the ϕ wings region (1.01-1.015 GeV/c^2, 1.024-1.029 GeV/c^2) and was normalized to give the number of BG events in the signal region. The error in the sensitivity, listed on the histograms, was calculated based only on statistical error.

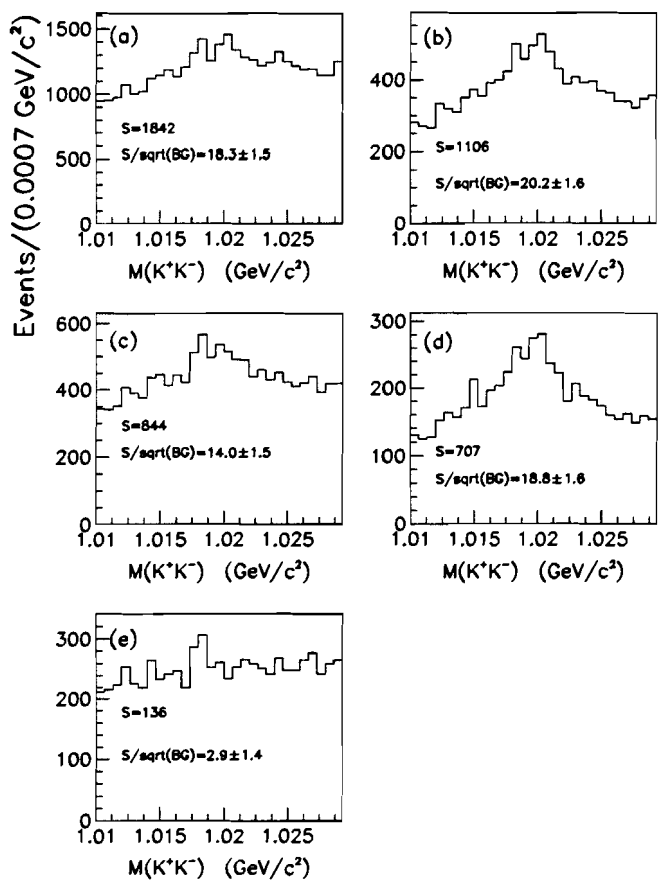

Figure 5.6: Spectra of $\phi \rightarrow K^+K^-$ from the $\phi\pi p$ event sample, with different momentum dependent KID cuts, as described in the text. The number of events in the ϕ signal and its sensitivity are printed on each of the histograms. The statistical error on the sensitivity is printed too.

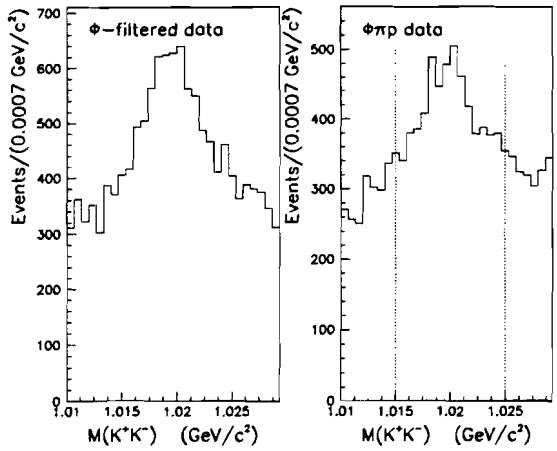

Figure 5.7: Spectra of K^+K^- invariant mass from (a) ϕ–filtered data and (b) $\phi\pi p$ event sample. The histograms are plotted with the optimized KID cut. The dotted lines on (b) demonstrate the ϕ mass cut applied to the $\phi\pi p$ data.

Several observations were made:

- The cuts recommended by Table 5.1 result in the worst sensitivity (Fig. 5.6(c)).
- The requirements in the "simple" KID cut result in the best sensitivity (Fig. 5.6(b)). Also, the number of events in the signal is larger in this histogram than in 5.6(c).
- The cuts with which Fig. 5.6(d) is plotted give somewhat lower sensitivity (but the same within errors) and a lower yield in the ϕ signal in comparison to Fig. 5.6(b).
- Fig. 5.6(e) shows the events selected by the cut C(K)<0.2 in the 6-11 GeV/c momentum region and the cuts recommended by Table 5.1 for tracks having other momenta. Clearly, this spectrum contains mostly background events. It means that a demand of "no C(K) cut" for tracks having momenta between 6 and 11 GeV/c selects only background events if C(K)<0.2 .

In summary, we defined the optimal KID selection criterion to be the suggested "simple" KID cut. Clearly, it gives the best yield and sensitivity compared to other momentum dependent cuts on C(K). This KID cut excluded more than 85% of pions and 60% of protons, while accepting about 70% of kaons. In view of the narrow ϕ peak and in order to better identify the ϕ contribution to the pentaquark analysis we also narrowed the ϕ mass cut to be $\pm$ 5 MeV/c^2 instead of $\pm$ 10 MeV/c^2. Fig. 5.7 shows the ϕ signals from the ϕ-filtered data and from the $\phi\pi p$ sample with the optimal KID cut. It can be seen that these ϕ signals are of the same quality, meaning that the optimal KID cut selects equally well ϕs from the two samples that were selected independently.

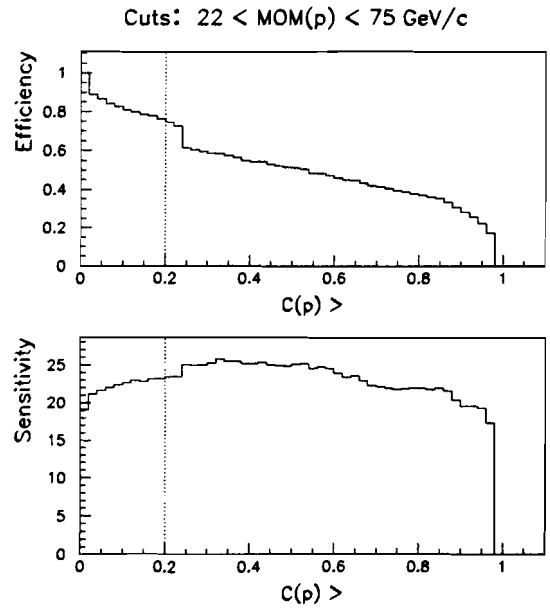

Figure 5.8: The efficiency (top) and sensitivity (bottom) plotted as a function of a "running" cut on the C(p) variable, where a momentum cut of 22<MOM(p)<75 GeV/c is required. The dotted line represent the chosen cut value.

5.4.2 Proton Čerenkov cut optimization

As we know from the Čerenkov performance, it can identify protons unambiguously only if their momentum is between ~22 and 75 GeV/c (see section 4.2.2). Thus, we activated the optimization procedure to define the cut on C(p) with the demand that the proton candidate tracks have momenta in this range. Fig. 5.8 shows the results of this momentum-dependent optimization. The top and bottom plots show the efficiency and sensitivity versus a "running" cut value on C(p), respectively. The signal events were taken from the simulated pentaquark and the background was taken from the data.

The efficiency of the cut applied to the momentum of the proton is approximately 70% and a cut on C(p) further reduces the efficiency. Therefore, applying a proton identification cut is worthwhile only if there is a drastic improvement in the sensitivity. Such an improvement is not seen in the sensitivity plot of Fig. 5.8. In fact, the sensitivity does not vary rapidly as a function of the cut on C(p). For that reason we choose not to demand any cut on the C(p) variable, except for the mild cut required in early stages of the analysis, of C(p)>0.038 (with no momentum cut). This was defined as the optimal proton identification cut that is listed in Table 5.3 as part of "set 1". This proton identification cut excluded more than 35% of pions, while accepting more than 90% of protons and kaons.

However, for test purposes we defined additional cuts using the efficiency and sensitivity plots of Fig. 5.8. According to the sensitivity plot the milder cut value which results in the largest sensitivity is: C(p)>0.25. However, since this is the K/p ambiguity value, it is possible to cut only on a somewhat smaller or larger C(p) value. A

cut on C(p) above the ambiguity peak results in efficiency which is smaller by $\sim$ 15% than the efficiency for a cut applied below it. The gain in sensitivity does not even reach 10%. It is preferable therefore to require a cut on C(p) just below the ambiguity peak. Finally, we defined the following cuts:

1. Require that the proton track has a momentum in the range of 22–75 GeV/c and for these tracks demand C(p) > 0.2 (the optimization results).

2. For the same momentum region require C(p) > 0.9, as it identifies extremely well the protons (at a cost in efficiency).

These selection criteria are listed in Table 5.3 as part of "set 2" and "set 3". In fact, the only difference between the three sets of selection criteria are the cuts applied to the proton candidate track.

5.4.3 Pion Čerenkov cut

Since most of the particles emerging from the interaction and the downstream decays were pions we did not optimize a cut on C(π). Instead, we rejected tracks having Čerenkov probabilities less than the a-priori to be pions (C(π) < 0.78) . The pion Čerenkov identification requirement excluded about 75% of protons and kaons, while accepting about 70% of pions.

5.5 The Pt2dk kinematical cut

The Pt2dk is a kinematical variable, well described by the MC, as shown in section 4.2.2. It is very sensitive to the mass because it depends on the Q value of a decay, increasing as the Q value rises. For example, when a cut on Pt2dk, derived from optimization for the D_s, was applied to $\phi\pi$ invariant mass spectrum, it completely eliminated the $D^{\pm}$ peak that comes in the same mass plot. This can be seen in Fig. 5.9 where we show the $K^+K^-\pi$ mass plot for a range of Pt2dk cuts. In order to avoid this sensitivity we required looser cuts on the Pt2dk variable than recommended by the optimization procedure sensitivity plots.

In the pentaquark analysis, the optimization procedure used the two pentaquark MC samples, with M($P^0_{\bar{c}s}$) of 2.75 and 2.83 GeV/c^2. A pentaquark mass of 2.75 GeV/c^2 corresponds to a binding energy of 150 MeV/c^2, the maximum possible value for a pentaquark binding potential (see sec. 1.1). In practice, one should expect a much smaller binding energy and therefore larger Q value.

The optimization results are shown in Fig. 5.10. The sensitivity and efficiency calculated as a function of a "running" cut value on Pt2dk. The results using the two MC samples are shown one on top of the other, where the solid and dashed lines refer to a pentaquark simulated mass of 2.83 and 2.75 GeV/c^2, respectively. The selection criterion suggested by the solid lines is: Pt2dk> 0.5 - 0.6, and by the dashed: Pt2dk> 0.4 - 0.5. We therefore chose to apply the cut: Pt2dk > 0.5.

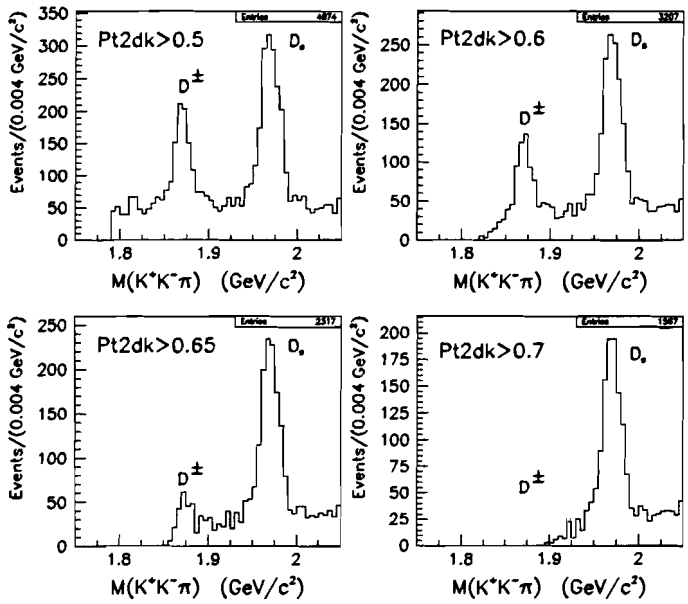

Figure 5.9: The $K^+K^-\pi$ invariant mass spectrum, showing $D^{\pm}$ and $D_s^{\pm}$ signals, with various Pt2dk cuts. We note the disappearance of the $D^{\pm}$ peak for tight cuts.

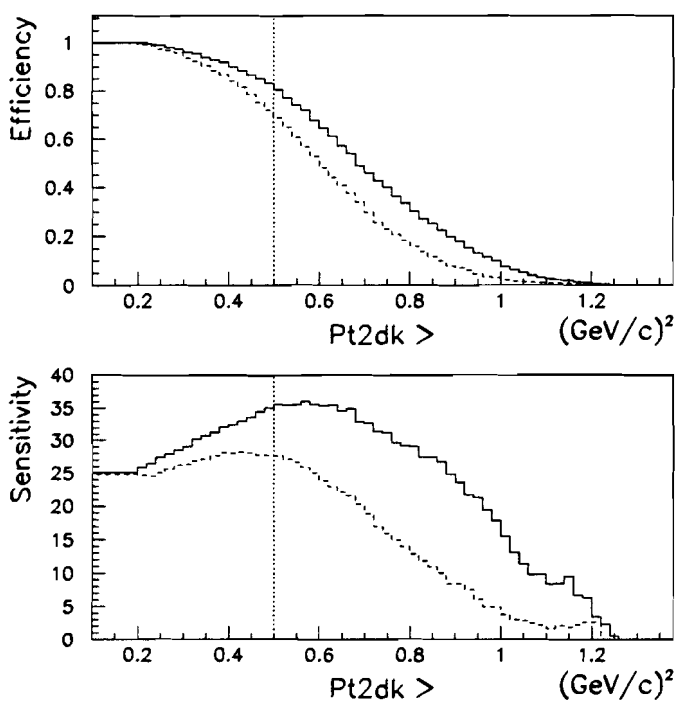

Figure 5.10: Efficiencies (top) and sensitivities (bottom) plotted as a function of a "running" cut on Pt2dk. The solid and dashed lines represent optimization results using pentaquarks simulated with a mass of 2.83 and 2.75 GeV/c^2, respectively.

5.6 General cleaning cuts

5.6.1 Secondary interactions

Secondary interactions occur when particles emerging from the π-nucleus interaction (the primary interaction) interact with nuclei from the downstream targets. The reconstruction program that produced a list of good vertices (the "vertex list") could find a vertex of secondary interaction and call it a decay vertex as it was located downstream to the primary vertex (see sec. 3.1.2).

In the pentaquark (and D_s) analyses we did not use the list of good vertices. Instead, we reconstructed secondary vertices only for the chosen $KK\pi p$ (and $KK\pi$) candidate tracks and checked that these decay vertices were located outside of any target foil ($SIGMA > 2.5$). If one of the four (or three) tracks belonged also to a decay vertex from the "vertex list" we demanded that this vertex was located also outside any of the target foils. This requirement prevented false reconstruction of vertices from products of secondary interaction processes. Indeed, events containing such shared tracks contributed only to the background spectrum of the decay $D_s \to K^*K$ [39].

5.6.2 Ghost tracks

Noise in the Drift Chambers (DCs) produced pulses on the wires and could appear as false hits. As a result, false ("ghost") tracks were reconstructed, made of true and false hits together, especially if the DC information was limited to DCs from stations 1 and 2 only (CAT=3). Thus, sometimes two or more tracks from the DC region were matched with a single track from the Silicon Microstrip Detector (SMD) region and were packed as separate tracks (see sec. 3.1). One way to eliminate ghosts was to find those tracks which have the same slope in the SMD region.

We tested for ghost tracks among the four candidate tracks in the decay vertex by calculating the sine of the angle between two tracks in each of the six possible combinations: $\sin(\theta_{ij})$. The indices i and j are 1,2,3,4 and refer to the K, K, π, p candidates, in that order. The angle between two ghost tracks in the SMD region should be zero. Thus, the $\sin(\theta_{ij})$ parameter was calculated using the slopes of tracks in the SMD region only. We used two thirds of E791 data and examined the $KK\pi p$ combinations selected by the pentaquark analyser cuts and by the cuts of "set 1". Fig. 5.11 shows distributions of $\sin(\theta_{ij})$ for all track combinations, plotted with the pentaquark analyser cuts. It can be seen that the angle between the two kaon tracks (tracks 1,2) is the smallest compared with angles between other pairs of tracks. This is because the ϕ mass is just above the two kaon threshold. The kaons emerging from a ϕ decay have almost no transverse momentum relative to the ϕ momentum direction and hence, they move almost in the same direction.

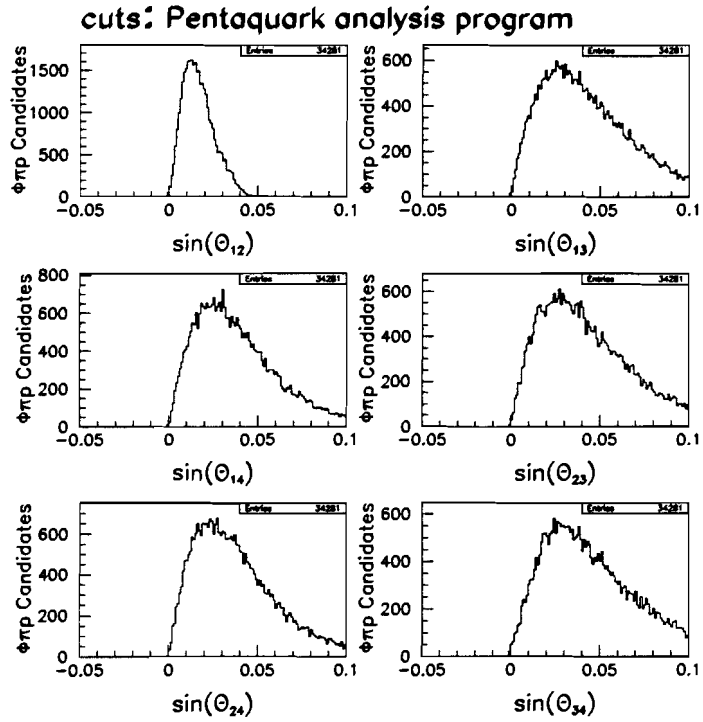

Figure 5.11: Distributions of $\sin(\theta_{ij})$ between each two tracks among the candidate K, K, π, p tracks, plotted with the pentaquark analyser cuts.

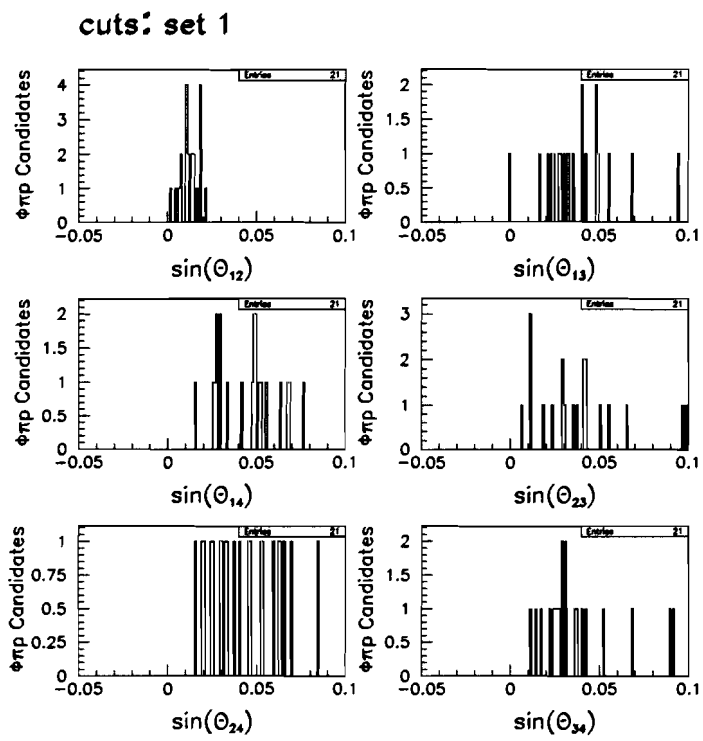

Figure 5.12: Distributions of $\sin(\theta_{ij})$ between each two tracks among the candidate tracks K, K, π, p, plotted with "set1" cuts.

Fig. 5.12 shows the same distributions, plotted with the cuts of "set 1". Here, it can be seen that there is one combination for which $\sin(\theta_{13}) = 0$. Tracks 1 and 3 (which refer to K and π) in this combination are therefore considered as ghost tracks and should be removed. The cut required following this study was:

$$(\sin(\theta_{12}).and.\sin(\theta_{13}).and.\sin(\theta_{14}).and.\sin(\theta_{23}).and.\sin(\theta_{24}).and.\sin(\theta_{34})) > 0.00001 \tag{5.4}$$

5.6.3 The "mirror gap" cut

A series of baffles were placed in the horizontal midplane of the two Čerenkov counters (see sec. 2.1.6). Therefore, the mirror planes in the two counters were divided to upper and lower parts, separated by a physical gap. As a result, the light being emitted from particles hitting this gap was not detected. The lack of light in the gap region could cause to misidentification of light hadrons (like π) as heavier hadrons (like K or p). It could happen in momentum ranges where the heavy hadrons do not emit Čerenkov radiation.

To check tracks that were pointing to the gap region we examined Y-slopes of tracks (dY/dZ). Tracks that hit the gap between mirrors had very small slope in the Y-direction, which was not affected by the magnetic field (acting in the X-direction). Again, we used two thirds of E791 data and examined the distributions of dY/dZ of the candidate tracks K, K, π, p, selected by the pentaquark analyser. Fig. 5.13 shows distributions of dY/dZ for the proton candidate tracks, plotted with the pentaquark analyser cuts (top) and with the cuts of "set 2" that include a tight proton identification cut (bottom). Indeed, an artificial enhancement of proton candidate tracks is seen near $dY/dZ = 0.0$ in both distributions. The distributions of dY/dZ for the two kaon candidate tracks show a similar behaviour when the pentaquark analyser cuts are required, but the enhancement of events near $dY/dZ = 0.$ is not apparent with the tighter selection criteria. Nevertheless, we removed events with either proton or kaon candidates pointing to the gap region since in the pentaquark analysis we rely extensively on the information from the Čerenkov counters for the K and p identification. We defined the "mirror gap" cut in the following way:

$$\begin{aligned} .\text{not.}\quad & (-0.0025 < dY/dZ(K1) < 0. \quad .\text{or.} \\ & -0.0025 < dY/dZ(K2) < 0. \quad .\text{or.} \\ & -0.0025 < dY/dZ(p) < 0.) \end{aligned}$$

5.6.4 Double entries

We checked that events were not selected more than once into the final sample of candidate events. However, in some events five tracks were selected and formed two acceptable 4-prong decay vertices. This caused more than one entry from the same event in the invariant mass spectrum. We examined the events selected by the optimal selection criteria and found that two of these events contributed such double entries to the final $K^+K^-\pi p$ spectrum (plotted with "UL96" set of cuts, as listed in table 5.3, from the full data set). In both events the accepted combinations of four tracks consisted of the same two kaons and proton candidate tracks, and of a different pion candidate track in each entry. In order to decide which combination to keep in each of the two events, we scanned over all variables characterizing the pion

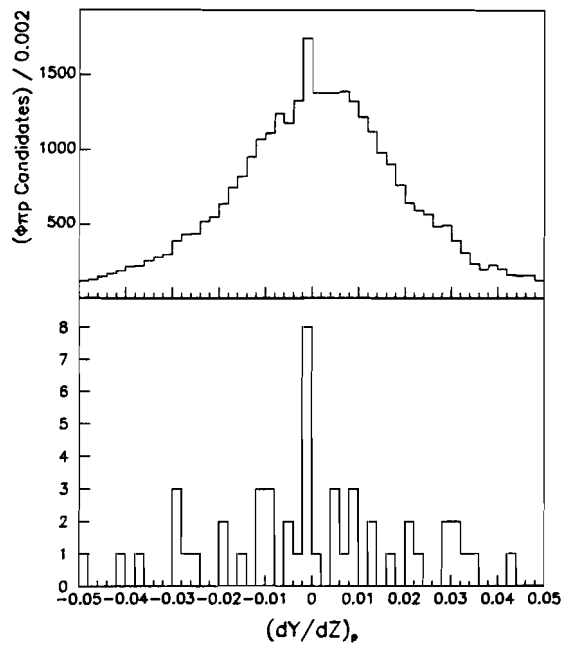

Figure 5.13: Slopes of proton candidate tracks in the Y-direction. The top histogram is plotted with the pentaquark analyser cuts. The bottom histogram is plotted with the cuts of "set 2".

track: MOM(π), χ^2_{track}, CAT(π), NCAT(π), C(π), RAT$_\pi$ (for definition of variables see section 3.2.1). We also scanned the variables which helped to define the secondary vertex, constructed of this pion and the other three tracks (χ^2_{pri}, χ^2_{sec}, SDZ, RAT, ISO, SIGMA). Table 5.2 lists the values of the scanned variables for each of the entries in the two events found. It can be seen that for the first event the pion in the first entry is better defined. Its momentum is higher, it has a better category, a higher C(π) and a smaller RAT$_\pi$ value, meaning that it passes closer to the reconstructed secondary vertex. The secondary vertex that includes this track has a smaller χ^2_{sec} and it is better isolated from surrounding tracks than the vertex reconstructed with the other pion. We therefore chose to include the first entry of this event in the final $\phi\pi p$ spectrum. The decision was more complex for the second event. There, the values of all variables are very similar. The main difference is the value of CAT(π), which is 15 for the first entry and 3 for the second one. Since the category of the pion in the second combination had been changed to NCAT=28 by the neural network routine we considered it as a bad track and kept the other entry.

		MOM(π) (GeV/c)	$\chi^2_{track}(\pi)$	CAT(π)	NCAT(π)	C(π)	RAT$_\pi$
1st event	1st entry	17.646	2.25	15	15	0.941	0.3166
	2nd entry	1.093	2.125	3	3	0.808	1.1863
2nd event	1st entry	2.926	0.875	15	15	0.828	0.4124
	2nd entry	2.779	0.75	3	28	0.828	0.4194
		χ^2_{sec}	χ^2_{pri}	SDZ	RAT	ISO (cm)	SIGMA
1st event	1st entry	0.568	1.464	12.532	0.0002	0.0092	14.13
	2nd entry	2.04	1.533	12.305	0.0007	0.0022	13.642
2nd event	1st entry	1.967	2.846	12.854	0.0006	0.0043	10.467
	2nd entry	1.747	2.664	12.655	0.0007	0.0041	10.231

Table 5.2: Values of parameters related to two combinations of four tracks (entries) in two events. All four entries were selected by the optimal set of selection criteria ("UL96"). The variables characterizing the pion candidate track are listed in the top part of the table, and those characterizing the four-prong decay vertex are listed in its bottom part.

5.7 Summary: The chosen set of cuts, "UL96"

Table 5.3 lists the variables calculated in the $\phi\pi p$ analysis, together with the optimal selection criteria defined for them. The set of cuts marked as "UL96 set" includes the combined cut: "set 1".or."set 4", and the general cleaning cuts and misidentification cuts, discussed in section 5.6 and in chapter 6, respectively. The sets of cuts, marked as "set 2" and "set 3", are identical to the cuts in "set 1", except for the proton identification criteria.

We used the "UL96" set of selection criteria to obtain the final results as it contains the optimal cuts we chose for the pentaquark search. The proton identification requirements defined in "set 2" and "set 3" were used for consistency test purposes. The results are discussed in chapter 8.

	Variables	Selection criteria	
		pentaquark	D_s
"set 1":	SIGMA >	2.5	2.5
	SDZ >	10	10
	ISO >	0.001 cm	0.001 cm
	DIP <	0.0025 cm	0.0025 cm
	RAT <	0.001	0.001
	RAT(i)/AVGR <	3	3
	χ^2_{pri} <	3	3
	χ^2_{sec} <	3	3
	DSTMIN <	0.005 cm	0.005 cm
	$C(K1, K2)$ >	0.2	0.2
	MOM(K1,K2)	6 - 40 GeV/c	6 - 40 GeV/c
	$C(\pi)$ >	0.78	0.78
	$C(p)$ >	0.038	-
	Pt2dk >	0.5 (GeV/c)^2	0.5 (GeV/c)^2
	ϕ MASS	$\pm$ 5 MeV/c^2	$\pm$ 5 MeV/c^2
	INV. MASS	2.4-3.1 GeV/c^2	1.75-2.05 GeV/c^2
"set 2":	"set 1" .and.		
	$C(p)$ >	0.2	-
	MOM(p)	22 - 75 GeV/c	-
"set 3":	"set 1" .and.		
	$C(p)$ >	0.9	-
	MOM(p)	22 - 75 GeV/c	-
"set 4":	"set 1"		
	.or. χ^2_{sec} <	6	6
	.and. MAXRAT$_i$ <	0.45	0.45
"UL96 set"	"set 1" .or. "set 4" .and.		
	General cleaning cuts		
	No secondary interactions		
	No ghost tracks		
	No K, p tracks in "mirror gap"		
	No double entries		
	Misidentification cuts		
	No $D^0 \to K\pi\pi\pi$ candidates	+	-
	No $\Lambda \to \pi p$ candidates	+	-
	DIP(ϕ) >	0.0045 cm	0.0045 cm

Table 5.3: Selection criteria applied in the pentaquark and D_s analyses. $C(K1, K2)$ stands for the cuts applied to the Čerenkov probabilities of each of the kaons. "set 1" includes the originally optimized selection criteria. "Set 2" and "set 3" are identical to "set 1" except for the additional requirement of proton ID cut. "Set 4" is a result of the re-optimization process, and the "UL96 set" is the final set used. It results from combining "set 1" and "set 4" and includes all general cleaning and misidentification cuts.

Chapter 6

Misidentification Studies

In the pentaquark analysis, the four tracks emerging from the decay vertex were identified as $K\ K\ \pi\ p$, using mainly information from the Čerenkov counters. These counters could, in principle, identify electrons, muons, pions, kaons and protons ($e/\mu/\pi/K/p$) in the proper momentum regions, as discussed in detail in section 2.1.6. However, the mass assignment to tracks could be wrong. As a result it could be that known neutral particles with four-prong decays would show up as narrow "reflections" or as rather flat distributions in the $\phi\pi p$ invariant mass spectrum. This misidentification of a particle could contribute background events to the $\phi\pi p$ spectrum, that should be removed.

For misidentification studies we used the events selected by the requirements of "set 1" (listed in Table 5.3) from two thirds of E791 data. Fig. 6.1 shows the invariant mass spectrum of $\phi\pi p \rightarrow KK\pi p$ from this data set, with the cuts of "set 1". An accumulation of events is seen in this spectrum near 2.86 GeV/c^2. One of the purposes in the misidentification study was to find out whether the accumulation of events was a reflected signal of a known particle. In sections 6.1.1 and 6.1.2 I discuss the possibilities for particle misidentification, when different hadron masses ($m(\pi)$, $m(K)$, $m(p)$) are assigned to the four tracks forming the secondary vertex. The electron mass was not taken into account since the very mild Čerenkov ID requirements applied to the four candidate tracks rejected electrons. The pion candidate could be also a misidentified muon. However, using the information of the "muon wall" detector (see sec. 2.1.8), we found that none of the pion candidates that were selected by the cuts of "set 1" (or the cuts of the "UL96" set), was potentially a muon.

It could be also that the 4-prong decay vertex consisted of a combination of a 2- or 3-prong vertex with other two or one nearby tracks, respectively. These possibilities are discussed in section 6.2.

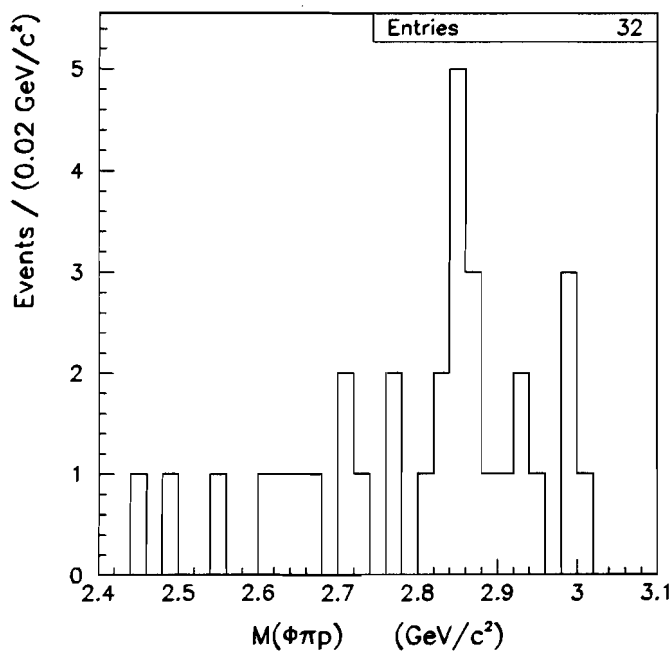

Figure 6.1: The $\phi\pi p$ invariant mass plotted from two thirds of E791 data, with the cuts of "set 1".

6.1 Misidentification of particles

In studying the misidentification of particles it was useful to determine the conditions under which we could expect a narrow "reflection". These could be derived from the energy-mass relation in Eq. 3.5. Its derivative relative to the mass of the jth track is:

$$\begin{aligned} \frac{\partial(M^2)}{\partial(m_j)} = 2M\frac{\partial M}{\partial(m_j)} &= 2\sum_i \sqrt{\vec{p}_i{}^{\,2} + m_i^2} \cdot \frac{m_j}{\sqrt{\vec{p}_j{}^{\,2} + m_j^2}} = \frac{2 \cdot E \cdot m_j}{E_j}, \\ \frac{\partial M}{\partial(m_j)} &= \frac{E}{E_j} \cdot \frac{m_j}{M}, \end{aligned} \tag{6.1}$$

where M and E are the mass and energy of the particle which decays, and m_i, $\vec{p}_i$ and E_i are the mass, momentum and energy of its ith decay product. The first order change in the mass of a particle (M) due to the change in the mass of the jth track is:

$$\Delta M = \frac{\partial M}{\partial(m_j)}\Delta m_j = \frac{E}{E_j} \cdot \frac{m_j}{M} \cdot (m_j - m_j') \simeq \frac{|\vec{P}|}{|\vec{p}_j|} \cdot \frac{m_j}{M} \cdot (m_j - m_j'). \tag{6.2}$$

Here, m_j and m_j' are the correct and the misidentified masses of the jth track. Since the track momenta are usually significantly larger than the particle masses we could approximate that: $\frac{E}{E_j} \simeq \frac{|\vec{P}|}{|\vec{p}_j|}$. Eq. 6.2 is valid only if the change in masses is not too

large. In general, we can expect Eq. 6.2 to work when there are several tracks and the fractional changes in mass are not too large.

As an example, we analysed the paper of the ARGUS collaboration with data on e^+e^- production of Ω_c [40]. The authors saw that if in the decay $\Xi_c \to \Xi\pi^+\pi^+\pi^-$ the π^- was assigned a mass of K^- it resulted in a narrow peak, about 120 MeV/c^2 higher than the mass of Ξ_c. If we use eq. 6.2 with the assumptions that $\frac{|\vec{P}|}{|\vec{p}_j|} \simeq 5$, $m_j = 0.14$, $m'_j = 0.49$ and $M = 2.47$ GeV/c^2, we get $\Delta M \simeq 0.1$. The variations in $\frac{|\vec{P}|}{|\vec{p}_j|}$ were of the order of 20% to 30% so that the misidentified events clustered in a relatively narrow peak shifted by about 100 MeV/c^2.

Fig. 6.2 shows distributions of the ratio $\frac{|\vec{p}_j|}{|\vec{P}|}$ for each of the four tracks in the pentaquark candidate decay. We used these distributions to predict what reflections we could expect if one of the tracks was misidentified. The distributions of $\frac{|\vec{p}_j|}{|\vec{P}|}$ for the two kaon candidates (tracks 1 and 2) are relatively narrow with a mean of 0.23. If we misidentified either of these tracks as a kaon while it was really a pion, we could expect to have the misidentified decays: $K\pi\pi p$ or $\pi K\pi p$, from a particle having the mass:

$$\Delta M = M - 2.86 = 4 \cdot \frac{0.14}{M} \cdot (0.49 - 0.14) \quad \Rightarrow M \simeq 2.6\ GeV/c^2. \qquad (6.3)$$

The variation in the ratio $\frac{|\vec{p}_j|}{|\vec{P}|}$ is about 40% for these two tracks, and the KID cuts and the narrow ϕ mass cut can further reduce this variation. The accumulation of events near 2.86 GeV/c^2 could be in principle a narrow reflection of a particle with a mass of ~ 2.6 GeV/c^2, which decays to $K\pi\pi p$ or $\pi K\pi p$. This mass, however, does not correspond to any of the known bound hadrons.

The distributions of $\frac{|\vec{p}_j|}{|\vec{P}|}$ for the pion and proton candidate tracks are broader than those of the kaons. If we use Eq. 6.2 and check what happens if we assign a pion or a kaon mass to the proton candidate track, we get $\frac{|\vec{P}|}{|\vec{p}_4|} \sim 2 - 7$ leading to $\Delta M = 0.1$ - 0.3 GeV/c^2 or 0.2 - 0.7 GeV/c^2, respectively. These are broad reflections. For the pion candidates $\frac{|\vec{P}|}{|\vec{p}_3|} \sim 3 - 20$. A replacement of the pion mass by the mass of a kaon or a proton leads to $\Delta M = 0.2$ - 0.9 GeV/c^2 or 0.6 - 2.7 GeV/c^2, respectively. These reflections are so broad that they appear as a flat background on the $\phi\pi p$ mass scale.

Our conclusion was that a narrow reflection could result only from $\pi \leftrightarrow K$ misidentification in one of the kaon candidates. In all other cases the result of misidentification would be a broad reflection or a flat distribution.

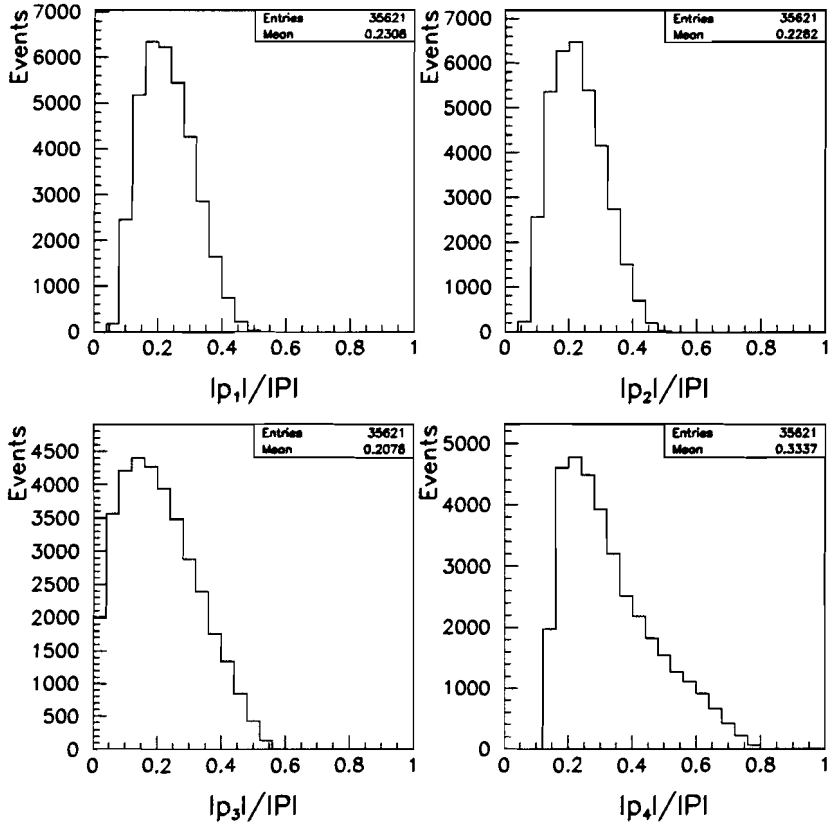

Figure 6.2: Ratios of track momenta to total pentaquark momentum, plotted with the pentaquark analyser cuts.

6.1.1 A reflection as a peak

If either of the two kaons (which makes the ϕ) was a misidentified pion, the $KK\pi p$ decay was a misidentified $K\pi\pi p$ or $\pi K\pi p$ decay. Fig. 6.3(a) is a two-dimensional plot of the mass of $K\pi\pi p$ or $\pi K\pi p$ versus the mass of $\phi\pi p \rightarrow KK\pi p$. Indeed, this plot shows that a correlation exists between the masses when one of the kaon tracks changes its identity. Hence, the observed accumulation of events in the $\phi\pi p$ spectrum could be associated with a structure or peak in the other decays. Fig. 6.3(b) is a y-projection of Fig. 6.3(a), namely, the invariant mass of $K\pi\pi p$ or $\pi K\pi p$. For these mass combinations we checked whether the tracks could emerge from the decay: $\Sigma_c \rightarrow \Lambda_c\pi \rightarrow (pk\pi)\pi$. However, the broad "reflection" at ~ 2.65 GeV/c^2, seen in Fig. 6.3(b), does not correspond to the Σ_c mass. Moreover, we did not observe any 3-prong subgroup of tracks in these events, with assigned masses of (p, K, π), that would reconstruct to the Λ_c mass. As a matter of fact, this is a broad reflection of the peak at 2.86 GeV/c^2, seen in the $KK\pi p$ spectrum, when one of the kaons changes its identity (based on Eq. 6.2: $\Delta M = 4 \cdot \frac{0.49}{2.86} \cdot (0.49 - 0.14) = 0.24$ GeV/c^2).

If the π was a misidentified kaon we could have background events from a misidentified $KKKp$ decay. Fig. 6.3(c) is a two-dimensional plot of the $KKKp$ mass versus

the mass of $\phi\pi p \rightarrow KK\pi p$. Fig. 6.3(d) is its projection on the y axis. A peak is seen in the $KKKp$ mass spectrum at 3.1 GeV/c^2, but from Fig. 6.3(c) it can be seen that this peak does not relate to the peak in the $KK\pi p$ mass spectrum. Still, it was interesting to understand the $KKKp$ spectrum. The $KKKp$ decay could be thought of as a $D_s \rightarrow \phi K$ (branching fraction $< 2.5 \cdot 10^{-3}$ at 90% C.L.) with an accidental proton passing near the vertex. We searched for $D_s \rightarrow \phi K$ decays in the data sample but did not observe any such decay. Another alternative could be a $\Lambda_c \rightarrow \phi p$ with an accidental kaon passing near the vertex. Again, we did not observe any three-prong subgroup of tracks in these events that would reconstruct to the $\Lambda_c \rightarrow \phi p$ mass.

We concluded that the accumulation of events, seen in the $\phi\pi p$ invariant mass spectrum near 2.86 GeV/c^2, was not a narrow reflection of a known decay.

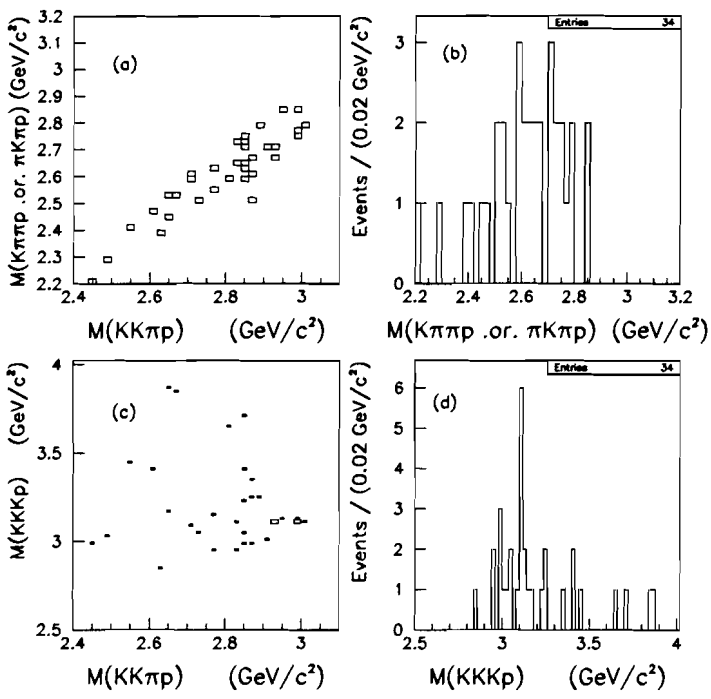

Figure 6.3: (a) M($K\pi\pi p$) or M($\pi K\pi p$) plotted versus M($\phi\pi p \rightarrow KK\pi p$), as a search for the reflected decay $\Sigma_c \rightarrow \Lambda_c\pi \rightarrow (pK\pi)\pi$. The K and p in the Λ_c candidate decay have opposite charges. (b) An invariant mass distribution of the track combinations ($K\pi\pi p$) or ($\pi K\pi p$), projected from (a). (c) M($KKKp$) plotted versus M($KK\pi p$). (d) One dimensional plot of M($KKKp$). All four histograms are plotted with the cuts of "set 1".

6.1.2 A flat reflection of a known particle

A known neutral charm particle, which decays to four charged daughter particles, could pass the pentaquark analysis selection criteria and form background events on the $\phi\pi p$ invariant mass scale. We wanted to remove such background events. For that purpose we looked for known neutral particles with 4-prong decays that could

pass the analysis cuts. We required that the lifetime of the neutral particle would be consistent with the SDZ cut, practically meaning that it would be a charm meson or baryon.

$$\underline{D^0 \rightarrow K\pi\pi\pi}$$

This required a misidentification of $K \rightarrow \pi$ and a $p \rightarrow \pi$, or $2K \rightarrow 2\pi$ and $p \rightarrow K$, and was therefore expected to display a flat distribution in the $\phi\pi p$ spectrum. In order to enhance the yield of the decay $D^0 \rightarrow K\pi\pi\pi$ we first relaxed the ϕ ID cuts (C($K1, K2$) and ϕ mass cut). The results are seen in Fig. 6.4, where the masses of all combinations of K and 3π tracks are plotted. An enhancement is seen for some of these combinations at the D^0 mass. The events left after requiring "set 1" cuts in the D^0 mass window (1.84 - 1.89 GeV/c^2) are potentially misidentified D^0s. In order to remove them from the $\phi\pi p$ invariant mass spectrum we rejected events with:

$$1.84\ GeV/c^2 \ < \ M(K\pi\pi\pi).or.M(\pi K\pi\pi).or.M(\pi\pi K\pi).or.M(\pi\pi\pi K) \ < \ 1.89\ GeV/c^2 \tag{6.4}$$

Fig. 6.5 shows the events rejected by this cut from the $\phi\pi p \rightarrow KK\pi p$ invariant mass spectrum. It can be seen that these events form a flat background.

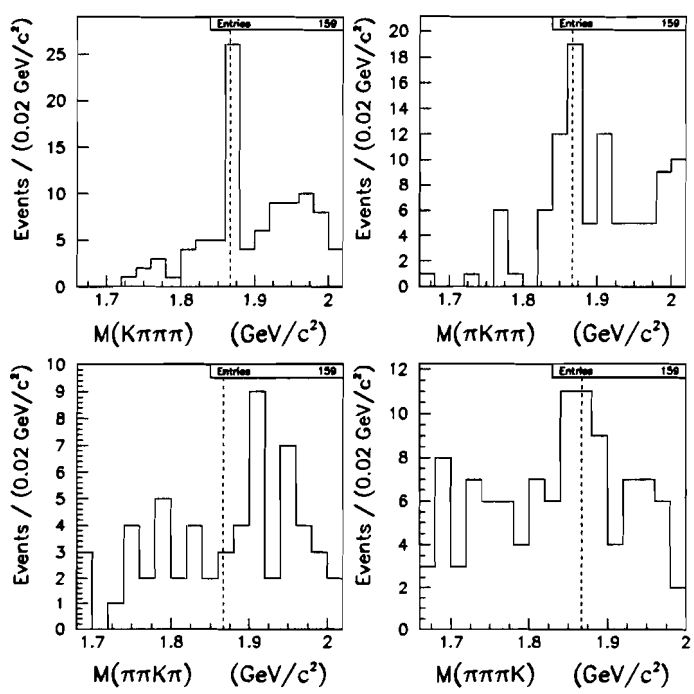

Figure 6.4: Histograms of M($K\pi\pi\pi$) of the four possible combinations, where $m(K)$ is assigned to different tracks in a cyclic permutation. The cuts are those in "set 1" with the KID and ϕID cuts relaxed. The dashed lines mark the D^0 mass, 1.865 GeV/c^2.

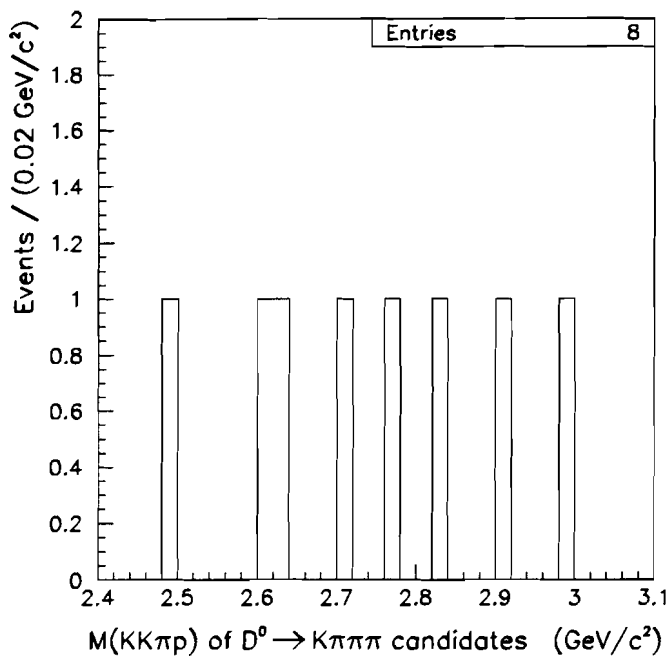

Figure 6.5: M($\phi\pi p \rightarrow KK\pi p$), plotted with "set 1" cuts for events that are also consistent with M($D^0 \rightarrow K\pi\pi\pi$) in all four possible combinations of tracks. The mass range taken for D^0 is: 1.84 - 1.89 GeV/c^2.

$\underline{D^0 \rightarrow KK\pi\pi}$

This required only a misidentification of $p \rightarrow \pi$. Even though the branching fraction for the decay $D^0 \rightarrow KK\pi\pi$ is more than an order of magnitude weaker than for the decay $D^0 \rightarrow K\pi\pi\pi$, the pentaquark analysis procedure selects better 4-prong decays with two kaons than decays with only one kaon. Nevertheless, since the mass sum of $2m(K)$ and $2m(\pi)$ is bigger than that of $m(K)$ and $3m(\pi)$, the Q value of the D^0 decay to $KK\pi\pi$ is smaller than for the $K\pi\pi\pi$ decay. Hence, the optimal selection criterion, applied to the Pt2dk variable in the pentaquark analysis, passed $D^0 \rightarrow K\pi\pi\pi$ candidates, but removed $D^0 \rightarrow KK\pi\pi$ candidates. In Fig. 6.6(a) we show M($KK\pi\pi$) with the optimal cuts of "set 1", but with the cut on Pt2dk relaxed to: Pt2dk > 0.2. The D^0 peak is clearly observed. The shaded area shows the events left after applying the optimal cut: Pt2dk > 0.5. As can be seen, no events are left in the D^0 mass region.

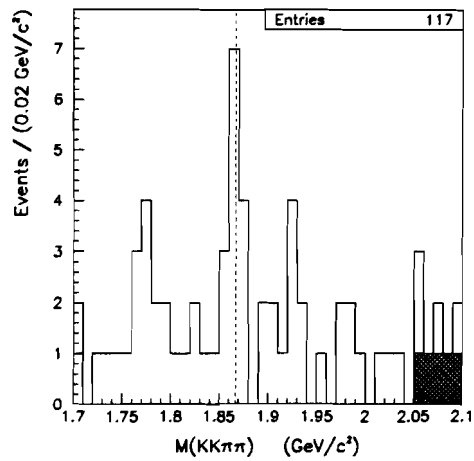

Figure 6.6: The $KK\pi\pi$ invariant mass, plotted with "set 1" cuts, but with Pt2dk > 0.2. The shaded area shows the events for which Pt2dk > 0.5. The dashed line marks the D^0 mass.

$$\underline{\Xi_c^0 \to K^- K^- \pi^+ p}$$

This would result from the decay $\Xi_c^0 \to K^- \bar{K}^*(892)^0 p \to K^- K^- \pi^+ p$. A misidentification of this decay required an exchange of $\pi \leftrightarrow K$ (to get $K^- K^- \pi^+ p$ from $K^- K^+ \pi^- p$ combination). The results are shown in Fig. 6.7. No Ξ_c^0 peak is observed and, as for the previous case, the Pt2dk cut eliminates the Ξ_c^0 mass range ($M(\Xi_c^0)$=2.47 GeV/c^2 [41]).

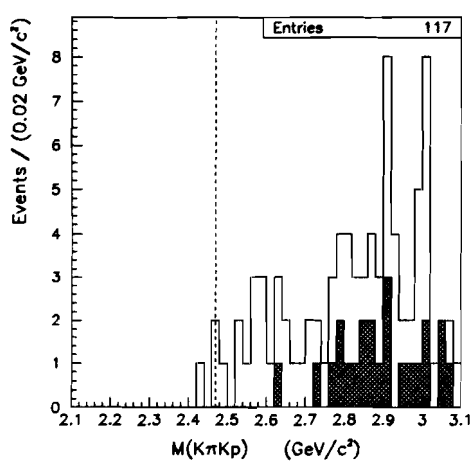

Figure 6.7: M($K^\mp \pi^\pm K^\mp p^\pm$) plotted as a search for the reflected decay $\Xi_c^0 \to K^\mp \pi^\pm K^\mp p^\pm$. The histogram is plotted with the cuts of "set 1", but with Pt2dk > 0.2. The shaded area shows the events selected by the Pt2dk > 0.5 cut. The dashed line marks the Ξ_c mass.

6.2 Misidentification of vertices

6.2.1 The subgroup of ϕs - Do they point back to the primary vertex?

We wanted to check whether the ϕs in the $\phi\pi p$ vertices really belonged to these vertices, or whether some ϕs were actually coming from the primary vertex, forming background events. For this purpose we defined a variable, called DIP(ϕ): the impact parameter of the the resultant of the two kaon tracks and the refitted primary vertex location. We used a sample of ϕ-filtered data (see sec. 3.2.2) to get the shape of the DIP(ϕ) distribution for ϕs emerging from primary interactions. Fig. 6.8 shows the DIP(ϕ) distribution for ϕs from this sample emerging from primary vertices in the target ($SIGMA < 2.5$).

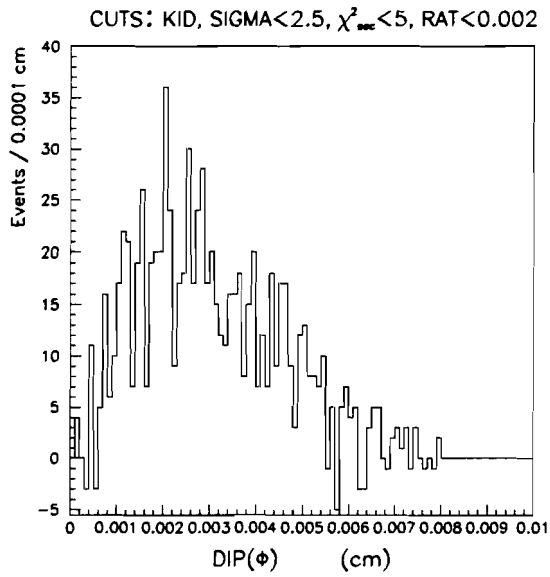

Figure 6.8: The DIP(ϕ) distribution, calculated for ϕs from ϕ–filtered data that emerged from primary vertices in the target.

To get the shape of the DIP(ϕ) distribution for ϕs emerging from a decay vertex, we plotted it from data and MC signals of the decay $D_s \rightarrow \phi\pi$. Fig. 6.9 shows distributions of DIP(ϕ) from D_s signals from data (top) and Monte Carlo (bottom). The left histograms were plotted with the analyser cuts and without a requirement on M($\phi\pi$) to be within the D_s mass window. These conditions pass many background events to the DIP(ϕ) distribution from data. The right histograms were plotted with the requirements of "set1" and the D_s mass window (1.94 GeV/c^2 < M($\phi\pi$) < 1.99 GeV/c^2), and should be therefore clean from background events. We note that the shape of the DIP(ϕ) distribution from MC remained the same after applying the cuts in "set1", while the shape of the DIP(ϕ) distribution from data changed and became similar to that from MC. Thus, we concluded that most of the events from data, having low values of DIP(ϕ), were indeed background events. Taking into account the shape of the DIP(ϕ) distribution of ϕs that emerged from the primary vertex, and

the fact the the events with low DIP(ϕ) in the D_s sample were actually background events, we defined a selection criterion of DIP(ϕ)>0.0045.

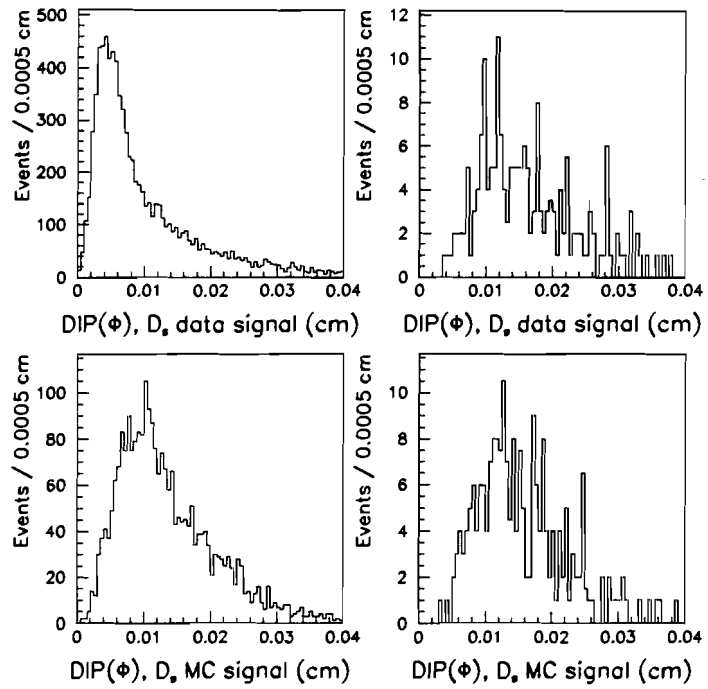

Figure 6.9: Distributions of DIP(ϕ), calculated for D_s signals from data (top) and MC (bottom). The histograms on the left are plotted with the D_s analyser cuts. The histograms on the right are plotted with the cuts of "set 1" and with an additional D_s mass window cut: 1.95 GeV/c^2 < M($\phi\pi$) < 1.99 GeV/c^2.

6.2.2 The πp subgroup - Is it a $\Lambda \rightarrow \pi p$ decay?

The πp subgroup in the $\phi\pi p$ decay could be a Λ particle passing near a ϕ. In order to check if there were such events within our data sample, we calculated the πp invariant mass. Fig. 6.10(a) shows the πp invariant mass distribution, plotted with "set1" cuts. Three events are peaked above background and have a mass within the Λ mass boundaries of 1.1115-1.1195 GeV/c^2. Fig. 6.10(b) shows the invariant mass of $\phi\pi p$, calculated for these three events.

As a result of this study we decided to remove candidate $\phi\pi p$ combinations with:

$$1.1115\ GeV/c^2 \ < \ M(\pi p) \ < \ 1.1195\ GeV/c^2.$$

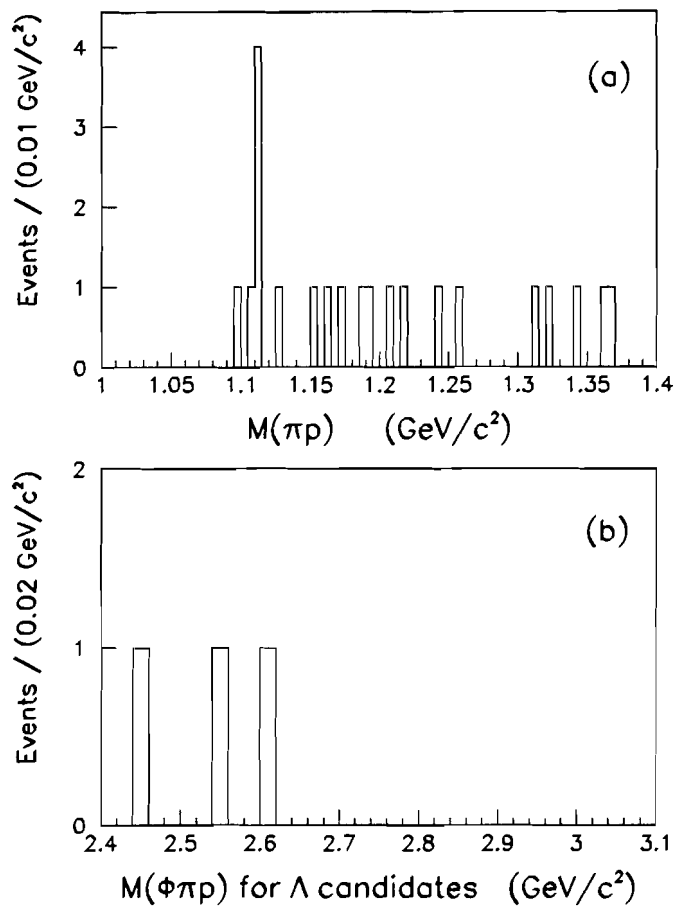

Figure 6.10: (a) The invariant mass of the πp subgroup of the $\phi\pi p$ candidates, plotted with the cuts of "set 1". (b) The $\phi\pi p$ invariant mass of the events, in which M(πp) is consistent with the Λ mass.

6.2.3 Phase space and thresholds

$\underline{Ds - p \text{ and } D - p}$

The observed accumulation of events in the $\phi\pi p$ invariant mass spectrum is very close to the threshold for the decays $D_s \rightarrow \phi\pi$ and $D \rightarrow \phi\pi$ with a proton: 2.9 and 2.8 GeV/c^2, respectively. We studied these thresholds and the possibility that some of the observed events were $D - p$ or $D_s - p$ combinations. In order to see the threshold behaviour of these events we analysed the data requiring $D \rightarrow \phi\pi$ or $D_s \rightarrow \phi\pi$ decays, with a proton coming from the primary vertex. The $\phi\pi + p$ invariant mass distributions are shown in Fig. 6.11, where the solid and dashed lines represent combinations with D_s and D masses, respectively. As can be seen, the accumulation of events near 2.86 GeV/c^2, lies between the threshold masses for the $D - p$ and $D_s - p$ particle combinations. We then checked if the requirements in the pentaquark analysis could select such events. First, in order to enhance the observed yield we relaxed

the 4-prong vertex definition cuts. The top plot in Fig. 6.12 shows a two-dimensional plot of M($\phi\pi$) versus M($\phi\pi p$) with the relaxed cuts. The enhancements at the D and D_s masses can be seen well. The D and D_s signals are seen well also in the bottom histogram, which shows the projected $\phi\pi$ invariant mass. Finally, we applied the cuts of "set 1" to the $\phi\pi p$ candidates, with an additional demand that the mass of $\phi\pi$ would be that of the D or D_s particles. Two events were selected from two thirds of E791 data, both lying above the threshold mass for $D_s - p$. We did not remove them from the spectrum of $\phi\pi p$ and did not include them either in the background events because we understood their source. Their effect on the final result is described in chapter 8.

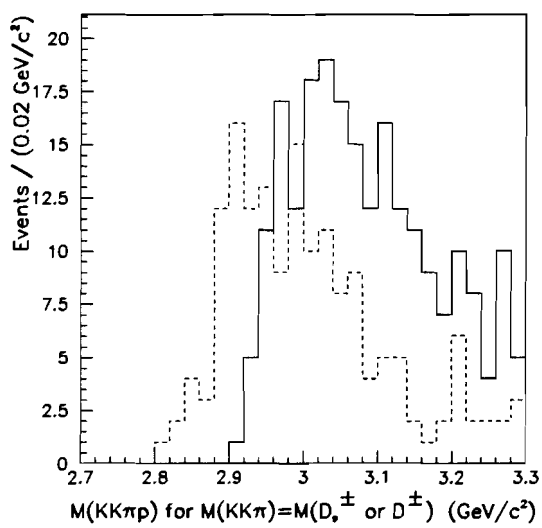

Figure 6.11: Phase-space distributions of M($D_s^{\pm}$ - p) (solid line) and M($D^{\pm}$ - p) (dashed line), where the $D_s^{\pm}$ and $D^{\pm}$ decay to $\phi\pi$ and the proton originates in the primary vertex.

$\Lambda_c - \pi$

The decay of $\Lambda_c \rightarrow \phi p$ could be another possible contribution to phase-space events. The top plot in Fig. 6.13 shows a two dimensional plot of M(ϕp) versus M($\phi\pi p$), with relaxed 4-prong vertex definition cuts but with the optimal KID and pID cuts. The optimal KID cuts include the cuts on the kaon momenta and on their Čerenkov probabilities, and the ϕ mass cut. The pID cuts include the cuts on the proton momentum and on its Čerenkov probability, as listed in "set 2" (see Table 5.3). Relaxing the 4-prong vertex cuts and requiring well defined ϕs and protons should enhance the yield in a potential $\Lambda_c \rightarrow \phi p$ signal. However, such an enhancement is not seen in this plot. The bottom plot in Fig. 6.13 shows a two dimensional histogram of M(ϕp) versus M($\phi\pi p$), with the selection criteria of "set 2". It can be seen that none of the events left are near the Λ_c mass (M(Λ_c)=2.285 GeV/c^2). We concluded that there is no contribution from $\Lambda_c - \pi$ events to our data sample.

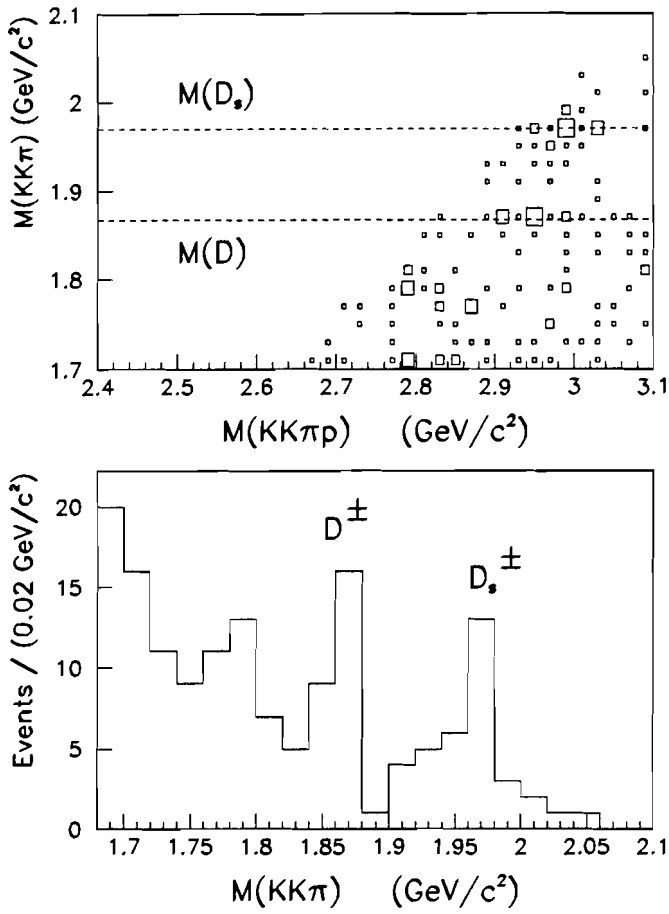

Figure 6.12: The top plot is a two dimensional histogram of M($\phi\pi \rightarrow KK\pi$) versus M($\phi\pi p \rightarrow KK\pi p$), with loose 4-prong vertex definition cuts and the KID and ϕID cuts of "set 1". The dashed lines show the masses of $D^{\pm}$ and $D_s^{\pm}$. The bottom plot is the projection of the top histogram on the M($KK\pi$) scale.

6.3 Generic Monte Carlo

The E791 Generic Monte Carlo is a sample of MC events, in which the production and decays of all known charm particles are simulated. The rate of particle productions and their decay processes were determined by cross sections and branching fractions as assigned to them by the LUND tables of particles [36]. The purpose in examining the Generic MC data was to check whether there were decays that had not been thought of, which could pass the pentaquark analysis cuts and get into the $\phi\pi p$ invariant mass spectrum. Since the number of charm decays simulated by the Generic MC, was not equal to the number of charm decays collected during the E791 run, we had to find the ratio between these two numbers. This ratio would be a normalization factor, by which the number of generic MC events selected by the pentaquark analysis should be multiplied, to give the expected number of background events from data. For deducing this normalization factor I compared the yield in signals of known decays:

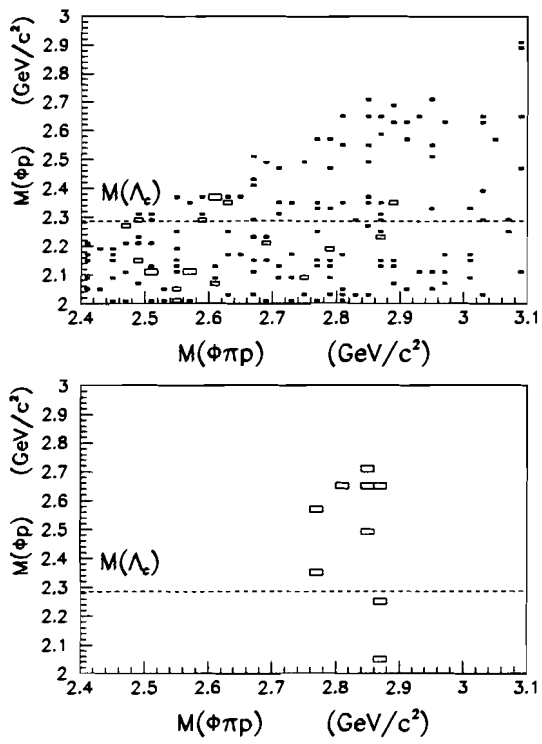

Figure 6.13: Two dimensional plots of M(ϕp) versus M($\phi\pi p$). The top histogram shows the distribution with loose 4-prong vertex definition cuts and with the optimal KID cuts of "set 1" and the pID cuts of "set 2". The bottom histogram shows the same distribution, plotted with the cuts of "set 2". The dashed lines mark the Λ_c mass.

$D^{\pm}, D_s^{\pm} \rightarrow \phi\pi^{\pm} \rightarrow KK\pi^{\pm}$ and $D^0 \rightarrow K\pi\pi\pi$, from Generic MC and two thirds of E791 data. The spectra of M($KK\pi$) and M($K\pi\pi\pi$) from Generic MC and data are shown in Fig. 6.14, both selected with the cuts of "set 1". Table 6.1 lists the ratios between the number of signal events in Generic MC and in the two thirds of E791 data. It can be seen from the table that these ratios are not consistent. Their weighted average is:

$$\bar{R} = 0.25 \pm 0.06$$

The ratio calculated from the $D^{\pm}$ signal is very close to this average value, while the ratios calculated for $D_s^{\pm}$ and D^0 signals are quite different, but overlap with it within errors. The differences may depend upon the values of production cross sections used to simulate these particles. Based on this averaged ratio we expected to see in the data about four times the number of events that were generated by the Generic MC and were selected by the cuts of the pentaquark analysis. In order to compare spectra of $\phi\pi p$ that were "clean" of background events we applied the cuts of "set 1" together with further background reduction cuts. These cuts included rejection of the misidentified decays $D^0 \rightarrow K\pi\pi\pi$, candidates of $\Lambda \rightarrow \pi p$, ϕs which pointed back to the primary vertex, and events with secondary interactions. Fig. 6.15 shows the $\phi\pi p$ invariant mass spectra from Generic MC (top) and from data (bottom), plotted

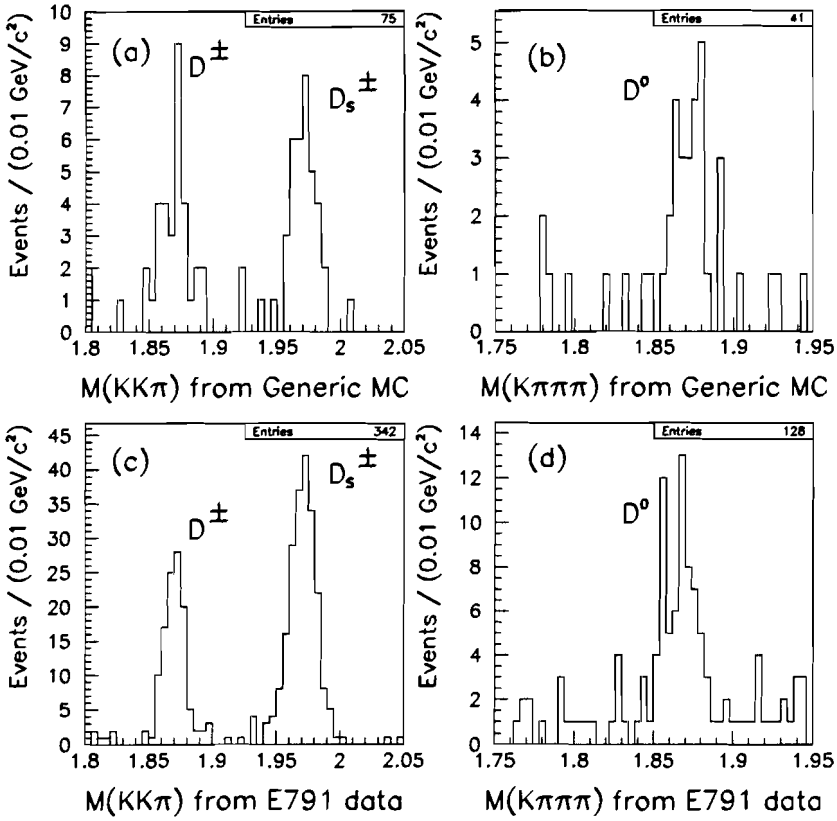

Figure 6.14: Invariant mass distributions of $\phi\pi \rightarrow KK\pi$ and $K\pi\pi\pi$, plotted from Generic MC (top) and from two thirds of E791 data (bottom). The histograms were plotted with those cuts of "set 1" common to the D_s and pentaquark analyses (left) or those common to the D^0 and pentaquark analyses (right).

with these requirements. It can be seen that only two Generic MC events survived the cuts of "set 1" after background subtraction. A demand of "set 2" or "set 3" cuts (the same as "set 1" but with additional proton ID cuts) leaves no Generic MC events in the $\phi\pi p$ spectrum. A prediction of the background level, based on the observed 2 events, would be $2 \cdot 4 = 8$ background events. There are 15 events in the $\phi\pi p$ spectrum from data, with the cuts of "set 1". If we treat the accumulation of events seen near 2.86 GeV/c^2 as a potential signal, then the rest $\sim$ 10 events could be considered background events, similar to the 8 events predicted by the Generic MC background study. Even if all 15 events are considered to be background, still this number is consistent with the prediction because of the statistical errors.

	Generic MC signal	DATA signal	Ratio
$D^{\pm} \to \phi\pi^{\pm} \to KK\pi^{\pm}$	28.5	103	0.28 (0.06)
$D_s^{\pm} \to \phi\pi^{\pm} \to KK\pi^{\pm}$	32.4	192	0.17 (0.03)
$D^0 \to K\pi\pi\pi$	21	50.5	$\sim$ 0.42 (0.12)

Table 6.1: Ratios between the yield in $D^{\pm}$, $D_s^{\pm}$ and D^0 signals from Generic MC and two thirds of E791 data.

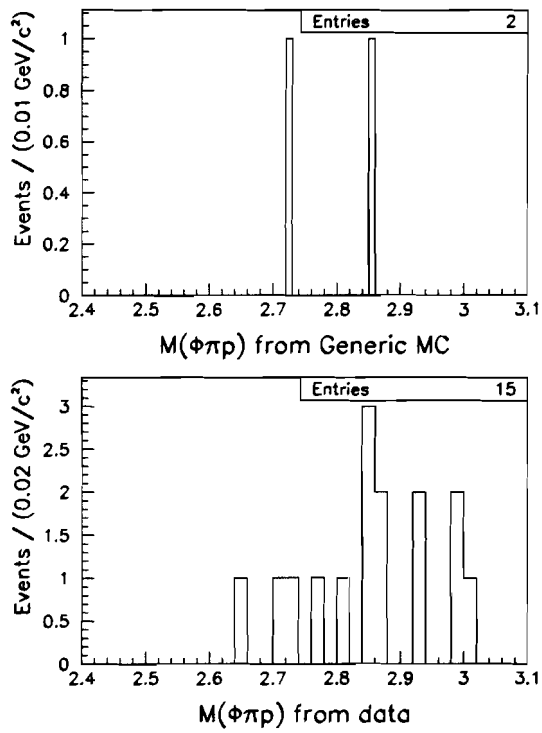

Figure 6.15: Invariant mass distributions of $\phi\pi p$, plotted from generic MC (top) and two thirds of E791 data (bottom). The histograms are plotted with the requirements of "set 1" and further background reduction criteria, as described in the text.

The next step was to understand the origin of the two Generic MC events left in the $\phi\pi p$ invariant mass spectrum. For that purpose I used the truth table of the Monte Carlo which lists all the particles produced by the simulation for each event, their masses, momenta, energies, lifetimes, and mother and daughter particles.

The truth-table information, which was related to the two Generic MC events left in the $\phi\pi p$ invariant mass spectrum, suggested that:

1. The first combination was: $KK\pi\pi$, where the two kaons originated from a ϕ decay and the two pions came each from a decay of a different particle (K^{0*}, $D_s^{\pm}$).

2. The second combination was: 4π, all of them originated in the decay $D^0 \to \pi\pi\pi\pi$

(with no additional particle).

The second combination showed another source for potential background events. I therefore calculated the invariant mass of the track combinations from data, selected by the pentaquark analysis, when the pion mass was assigned to all of them. Fig. 6.16 shows the $\pi\pi\pi\pi$ invariant mass spectra from data, plotted with 4-prong vertex definition cuts only. The shaded area shows the events selected by the cuts of "set 1". As can be seen, there is no D^0 peak seen, and no event is left in the D^0 mass window (1.84-1.89 GeV/c^2) after applying the cuts of "set 1". We therefore concluded that our data sample did not include any $D^0 \rightarrow \pi\pi\pi\pi$ candidates that could pass the pentaquark selection criteria.

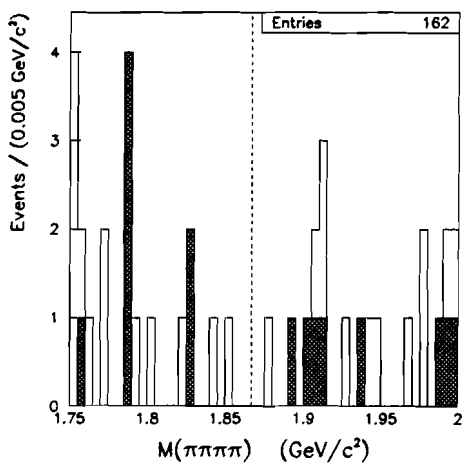

Figure 6.16: An invariant mass distribution of $\pi\pi\pi\pi$ from two thirds of E791 data, plotted with 4-prong vertex definition cuts. The shaded area refers to the events selected by the rest of the cuts in "set 1". The dashed line marks the D^0 mass.

6.4 Summary: Understood background

Among the events selected by the optimal selection criteria of the pentaquark analysis, we could find background events originating from misidentification of particles or vertices. We eliminated $\phi\pi p$ vertices that contain either $\Lambda \rightarrow \pi p$ candidates or a ϕ that points back within 45 μm of the production vertex. We identified no known particles that, if we misidentified their decay products, would form a peak in the $\phi\pi p$ mass window. The only source for flat background due to misidentification of particles was from the decay $D^0 \rightarrow K\pi\pi\pi$. Candidate $KK\pi p$ events with a $K\pi\pi\pi$ invariant mass consistent with the D^0 mass were removed. Above the appropriate thresholds, candidate $\phi\pi p$ events could be due to the combinations $(\Lambda_c \rightarrow \phi p) + \pi$ or $(D_s^{\pm}, D^{\pm} \rightarrow \phi\pi^{\pm}) + p$. No $\Lambda_c \rightarrow \phi p$ candidates were found within the $\phi\pi p$ sample, but three events from the full E791 data, for which the $\phi\pi$ invariant mass is consistent with the $D_s^{\pm}$ or $D^{\pm}$ masses, passed all the analysis cuts.

Fig 6.17(a) shows a spectrum of M($\phi\pi p$), plotted for two thirds of E791 data, with the optimal cuts of "UL96", before the various misidentification sources of background are removed. The shaded events constitute the misidentified background. Fig 6.17(b),(c),(d) show the events identified as $D^{\pm}$,$D_s^{\pm}$ - p phase-space events, the $D^0 \rightarrow K\pi\pi\pi$ or $\Lambda \rightarrow \pi p$ candidates, and the ϕs which point back to the primary vertex, in that order. We note that the shape of background events, that are shaded in Fig 6.17(a), is rather flat. The accumulation of events near 2.86 GeV/c^2 seen among the accepted events is not common to the spectrum of rejected events. The spectra of events rejected by each of the cuts exclusively (Fig 6.17(b),(c),(d)) show that none of them has any particular shape either.

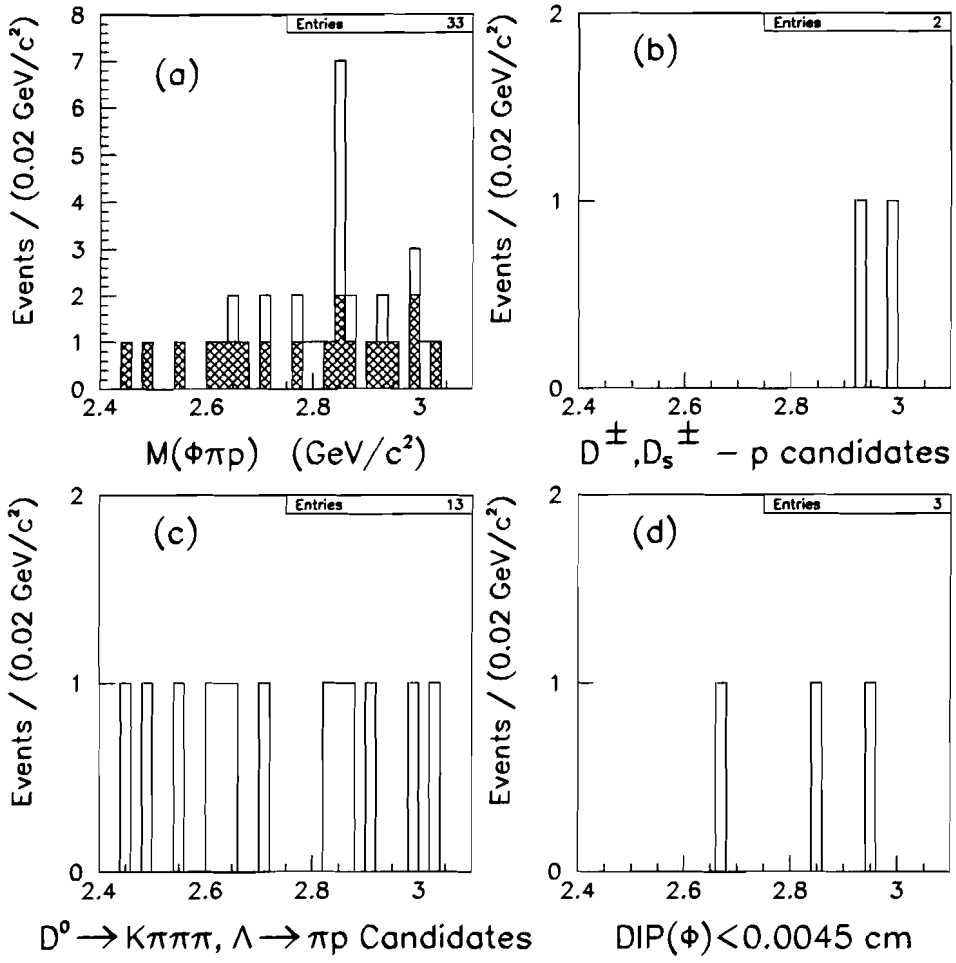

Figure 6.17: (a) M($\phi\pi p$), plotted from two thirds of E791 data, with the "UL96" cuts but before rejection of misidentified events. These background events (due to misidentification) are shaded. (b) M($\phi\pi p$) of events for which the invariant mass of $\phi\pi$ is consistent with the mass of $D_s^{\pm}$ or $D^{\pm}$. (c) M($\phi\pi p$) of misidentified $D^0 \to K\pi\pi\pi$ decays, or decays for which the πp invariant mass is consistent with the Λ mass. (d) M($\phi\pi p$) of events in which the ϕ points back to the primary vertex.

Chapter 7

Efficiencies of Selection Criteria and their Systematic Uncertainties

A particle that was produced in the interaction and decayed, does not always appear in the final signal. The reasons are either inefficiency of the detector or rejection of that specific decay by the cuts because its features are similar to the characteristics of background events. Therefore, the number of decays of a certain type that occurred during the experiment depends upon the detection efficiency and the selection criteria. The number of decays is then the yield in the signal of that decay mode divided by the efficiency of the selection criteria used to produce it. In section 7.1 I describe how we have used the Monte Carlo (MC) to measure by how much each cut reduces the detection efficiency and to define the total efficiency of all cuts.

In the pentaquark analysis we calculate the ratio of cross section times branching fraction of the decay $P^0_{\bar{c}s} \to \phi\pi p$ to the similar decay $D_s^\pm \to \phi\pi^\pm$, using the expression in Eq. 5.1. This expression contains the ratio of efficiencies calculated from cuts on pentaquark and D_s MC samples. A major consideration in selecting the final cuts was to minimize the systematic uncertainties in the ratio of pentaquark and D_s efficiencies (see sec. 4.2.2 and 5.3). In spite of these efforts some residual systematic uncertainties are left. In sec. 7.2 I describe how we estimated the systematic uncertainty in the ratio of efficiencies.

7.1 Efficiencies

The efficiency of a given cut was named "a reduction factor". It is the ratio of the yield in the pentaquark MC signal after applying a given cut and the yield observed with only the basic analyser cuts (see sec. 5.1). Table 7.1 lists the reduction factors of the cuts in the "UL96" set. For comparison, the table lists also the reduction factors derived for the $D_s \to \phi\pi$ decay from both MC and data.

Reduction factors of the cuts in the "UL96" set			
Cut	D_s from DATA	D_s from Monte Carlo	P^0 from Monte Carlo
SIGMA > 2.5	0.95 (0.01)	0.96 (0.01)	0.97 (0.01)
SDZ > 10	0.89 (0.01)	0.85 (0.01)	0.90 (0.01)
ISO > 0.001 cm	0.95 (0.01)	0.90 (0.01)	0.86 (0.01)
DIP < 0.0025 cm	0.77 (0.01)	0.85 (0.01)	0.89 (0.01)
RAT < 0.001	0.74 (0.01)	0.76 (0.01)	0.79 (0.01)
$RAT_i/AVGR < 3$	1. (0.01)	1. (0.01)	0.94 (0.01)
$\chi^2_{pri} < 3$	0.80 (0.01)	0.89 (0.01)	0.88 (0.01)
$\chi^2_{sec} < 3$	0.81 (0.01)	0.85 (0.01)	0.78 (0.01)
$\chi^2_{sec} < 3$ .or. $MAXRAT_i < 0.45$	0.99 (0.002)	0.99 (0.002)	0.93 (0.01)
All VTX Cuts ("UL96")	0.42 (0.02)	0.47 (0.02)	0.43 (0.02)
$C(K1, K2) > 0.2$	0.64 (0.02)	0.65 (0.01)	0.65 (0.02)
$MOM(K1, K2)$ 6 - 40 GeV/c			
$C(\pi) > 0.78$	0.85 (0.01)	0.67 (0.01)	0.74 (0.02)
Pt2dk > 0.5 $(GeV/c)^2$	0.87 (0.01)	0.83 (0.01)	0.83 (0.01)
$M(\phi) \pm 5$ MeV/c^2	0.8 (0.01)	0.84 (0.01)	0.85 (0.01)
set1: $C(p) > 0.0038$			1.
set2: $C(p) > 0.2$, MOM(p) 22 - 75 GeV/c			0.53(0.02)
set3: $C(p) > 0.9$, MOM(p) 22 - 75 GeV/c			0.21(0.03)
		General cleaning cuts	
No secondary interactions	0.94 (0.01)	0.95 (0.01)	0.95 (0.01)
No ghost tracks	1. (0.001)	1. (0.001)	1. (0.001)
No K, p tracks in "mirror gap"	0.94 (0.01)	0.92 (0.01)	0.86 (0.01)
		Misidentification cuts	
No D^0 or Λ candidates	-	-	0.87 (0.01)
$DIP(\phi) > 0.0045$ cm	0.97 (0.01)	0.97 (0.004)	0.90 (0.01)

Table 7.1: The reduction factors caused by each of the "UL96" cuts, calculated as the ratio between the yield in a peak after a cut is applied and the yield in the peak produced by the analyser. These reduction factors were calculated using signals of the decays $D_s^{\pm} \rightarrow \phi\pi^{\pm} \rightarrow K^+K^-\pi^{\pm}$ from Monte Carlo and data, and the Monte Carlo signal of the decay $P^0_{\bar{c}s} \rightarrow \phi\pi p \rightarrow K^+K^-\pi p$. The numbers in parentheses are the statistical errors.

From the table one can see which cuts have more drastic effect and for which we see significant difference between the MC and data. Clearly, the Čerenkov cuts are causing the largest reduction. However, if we combine all the vertex cuts (SDZ, ISO, DIP, RAT, $RAT_i/AVGR$, χ^2_{pri} and χ^2_{sec}.or.$MAXRAT_i$) their effect is about the same as that of all particle ID cuts (KID and πID), approximately 0.4.

The inconsistency seen between the reduction factors, measured using D_s signals from MC and data, show that the Monte Carlo does not simulate well some of the variables characterizing the decay $D_s^{\pm} \rightarrow \phi\pi^{\pm} \rightarrow K^+K^-\pi^{\pm}$. These differences in efficiency are taken into account in the evaluation of the systematic error.

A comparison between the reduction factors of the same cuts, when applied to the events in the simulated signals of the decays $D_s^{\pm} \rightarrow \phi\pi^{\pm} \rightarrow K^+K^-\pi^{\pm}$ and $P_{\bar{c}s}^0 \rightarrow \phi\pi p \rightarrow K^+K^-\pi p$, show that usually they are similar. The variables for which the cuts give different reduction factors are those related to the vertex being constructed of three tracks rather than four tracks. These variables are: χ^2_{sec} .or. $MAXRAT_i$, DIP, ISO and $RAT_i/AVGR$. The reduction factors calculated for the DIP(ϕ) and Pt2dk variables are different because of the different characteristics of the decay. While the Q value of the decay $D_s^{\pm} \rightarrow \phi\pi^{\pm}$ is similar to the pentaquark decay with M($P_{\bar{c}s}^0$)=2.83 GeV/c^2, the $D_s^{\pm}$ decays into two products and the pentaquark into three products. The momentum division among the product particles is therefore different and the shapes of the distributions of the momentum dependent variables are different as well (see Fig. 4.7). The cut on C(π) results in different reduction factors for each of the tested signals. Again, these differences are taken into account in the evaluation of the systematic uncertainty contributed by this cut.

The overall efficiencies of the pentaquark or D_s detection are the yields in the final signals from MC, divided by the number of pentaquark or D_s events produced by the simulation. These efficiencies include the reduction factors of the selection criteria and the acceptance of the detector. Table 7.2 lists the efficiencies measured for the optimal cuts of "UL96" set, using the three MC samples: the D_s, and the pentaquark produced with masses of 2.75 and 2.83 GeV/c^2. The difference seen in the table between the efficiencies calculated from the two pentaquark Monte Carlo samples needs to be understood.

Cuts	$\varepsilon_{P_{\bar{c}s}^0}$		ε_{D_s}
	M($P_{\bar{c}s}^0$)=2.75 GeV/c^2	M($P_{\bar{c}s}^0$)=2.83 GeV/c^2	
"UL96" set	0.0008±0.0001	0.0013±0.0001	0.0021±0.0001

Table 7.2: Efficiencies of the optimal cuts ("UL96" set), calculated from the Monte Carlo samples of pentaquarks with M($P_{\bar{c}s}^0$)=2.75 and 2.83 GeV/c^2, and from the Monte Carlo sample of D_s.

I therefore calculated the ratio of reduction factors between the two pentaquark MC samples for the cuts in the "UL96" set. Table 7.3 lists these ratios.
It can be seen that for most of the cuts the calculated ratio of reduction factors is $\sim$ 1 (within errors). The main contributions to the difference are coming from the cut on Pt2dk ($\sim$ 16%), the "no D0 candidates" cut ($\sim$ 13%) and from the cut on DIP(ϕ) ($\sim$ 5%). An additional $\sim$ 7% originates from the Pt2dk>0.2 and SIGMA>0.0 cuts that were required in the analyser stage. The Pt2dk distributions from the two pentaquark Monte Carlo samples are plotted in Fig. 7.1. The solid and dashed lines represent the pentaquarks simulated with a mass of 2.83 GeV/c^2 and 2.75 GeV/c^2, respectively. The difference in shape, seen in this figure, is the cause to the difference in efficiency. These differences are due to the dependence of Pt2dk upon the Q value of the decay (see sec. 3.2.1). Fig. 7.2 shows invariant mass distributions of the four tracks emerging from the pentaquark decay when all possible combinations of K and 3π masses are assigned to the tracks. Again, The solid and dashed lines represent pentaquarks simulated with a mass of 2.83 GeV/c^2 and 2.75 GeV/c^2, respectively. In three of the four plots it can be seen that there are more events in the D^0 mass

CUTS	$(\varepsilon_{P^0_{\bar{c}s}}, \mathrm{M}(P^0_{\bar{c}s})=2.83)\ /(\varepsilon_{P^0_{\bar{c}s}}, \mathrm{M}(P^0_{\bar{c}s})=2.75)$
Analyser cuts	1.066(0.046)
SIGMA > 2.5	0.998(0.008)
SDZ > 10.	1.015(0.024)
ISO > 0.001 cm	0.991(0.018)
DIP < 0.0025 cm	1.029(0.017)
RAT < 0.001	0.999(0.024)
$\mathrm{RAT}_i/\mathrm{AVGR} < 3$	0.996(0.01)
$\chi^2_{pri} < 3$	0.98(0.015)
$\chi^2_{sec} < 3$ .or. MAXRAT_i <0.45	1.02(0.013)
$\mathrm{M}(\phi) \pm 5$ MeV/c^2	1.011(0.02)
$\mathrm{C}(K1, K2) > 0.2$	0.978(0.034)
$\mathrm{MOM}(K1, K2)$ 6-40 GeV/c	0.986(0.011)
$\mathrm{C}(\pi) > 0.78$	1.016(0.03)
Pt2dk > 0.5 (GeV/c)^2	1.156(0.03)
$\mathrm{DIP}(\phi) > 0.0045$	1.054(0.018)
No secondary interactions	0.989(0.009)
No ghost tracks	0.999(0.001)
No $D^0 \to K\pi\pi\pi$ candidates	1.125(0.025)
No $\Lambda \to \pi p$ candidates	1.004(0.003)
All cuts	1.5(0.2)

Table 7.3: Ratios between efficiencies calculated from the two pentaquark Monte Carlo samples, with $\mathrm{M}(P^0_{\bar{c}s})$=2.83 and 2.75 GeV/$c^2$, for the optimal cut values of the "UL96" set. The numbers is parentheses are the statistical errors.

window of 1.84-1.89 GeV/c^2 from the sample of pentaquarks simulated with a mass equal to 2.75 GeV/c^2 than there are from those with a mass of 2.83 GeV/c^2. Since the misidentification cut on the D^0 requires no $D^0 \to K\pi\pi\pi$ candidates within the 1.84-1.89 GeV/c^2 mass region, in any of the four combinations, it rejects more events from the Monte Carlo sample with $\mathrm{M}(P^0_{\bar{c}s})$=2.75 GeV/$c^2$ than it does from the sample with $\mathrm{M}(P^0_{\bar{c}s})$=2.83 GeV/$c^2$.

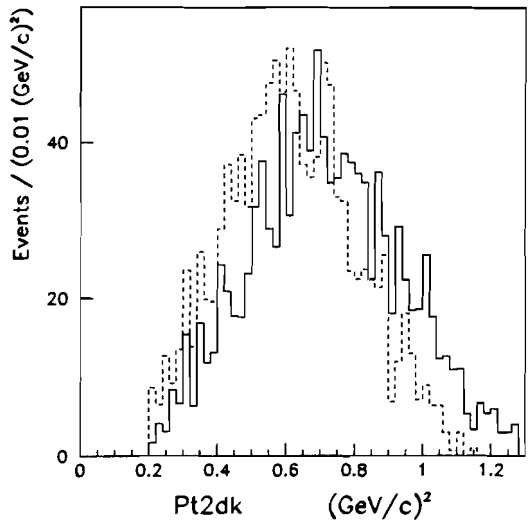

Figure 7.1: Distributions of Pt2dk, plotted from pentaquark Monte Carlo samples with $M(P^0_{\bar{c}s})$ equals to 2.83 GeV/c^2 (solid line) and 2.75 GeV/c^2 (dashed line).

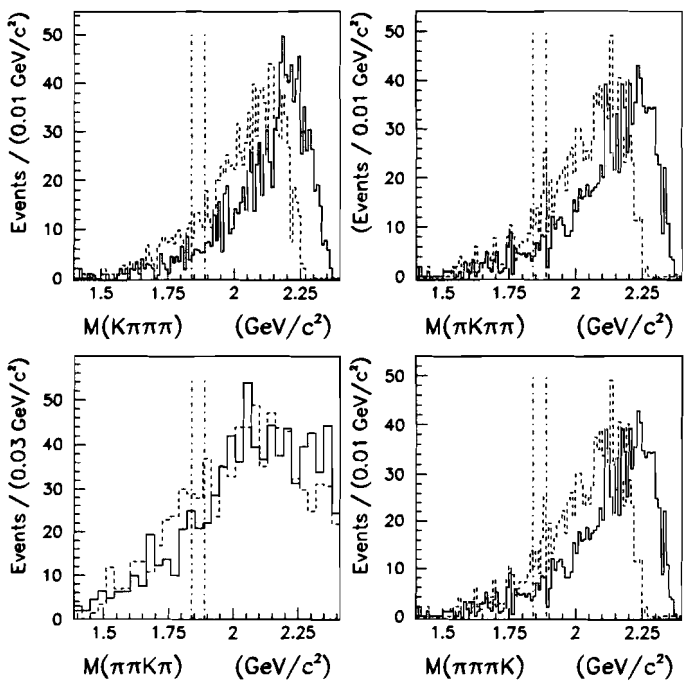

Figure 7.2: All $(K, 3\pi)$ invariant mass combinations calculated for the four tracks in the pentaquark decay vertex from Monte Carlo. The solid and dashed lines are for $M(P^0_{\bar{c}s})$ equals to 2.83 and 2.75 GeV/c^2, respectively. The dotted-dashed lines mark the D^0 mass window of the "No D^0 candidates" cut: 1.84-1.89 GeV/c^2.

In summary, some of the variables do depend on the pentaquark mass. The efficiencies of selection criteria applied to these variables are rising monotonically with the mass. Therefore, these selection criteria are not expected to form any artificial enhancement in the $\phi\pi p$ invariant mass scale. In order to check what is the effect of the mass dependent cuts on the invariant mass of $KK\pi p$, we studied a background spectrum of $\phi_{wings}\pi p$, where ϕ_{wings} refers to K^+K^- candidates with invariant mass in a range outside the required ϕ mass window (between 5 and 10 MeV/c^2 below and above the ϕ mass). Fig. 7.3 shows this spectrum with the "UL96" cuts. It can be seen that the distribution is rather flat, with somewhat more events with larger masses.

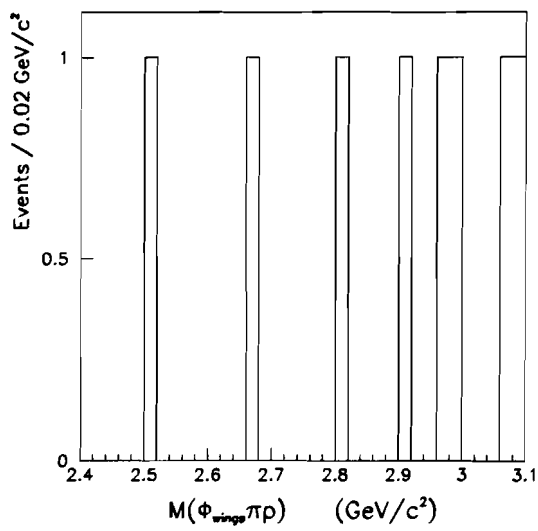

Figure 7.3: An invariant mass distribution of ($\phi_{wings}\pi p$), plotted with the optimal cuts of the pentaquark analysis ("UL96").

The top plots in Fig. 7.4 show $\phi_{wings}\pi p$ invariant mass distributions when each of the mass dependent cuts is released. The events rejected from the $\phi_{wings}\pi p$ distribution by the mass dependent cuts are shown in the bottom plots of that figure. It can be seen that these spectra are quite flat and do not show any particular shape. Thus, we concluded that the mass dependent cuts did not cause any artificial enhancement in the $\phi\pi p$ invariant mass spectrum.

7.2 Systematic uncertainties

Systematic errors could come from imperfect calibrations or from erroneous Monte Carlo simulation of the real data, which result in errors in the calculated variables that are subject to cuts. As a result, the efficiencies calculated for cuts on the simulated variable distributions would not measure the actual amount of signal rejected by the cuts in data.

For estimating the systematic uncertainties in the ratio of pentaquark and D_s efficiencies we first determined the differences between variable distributions from Monte

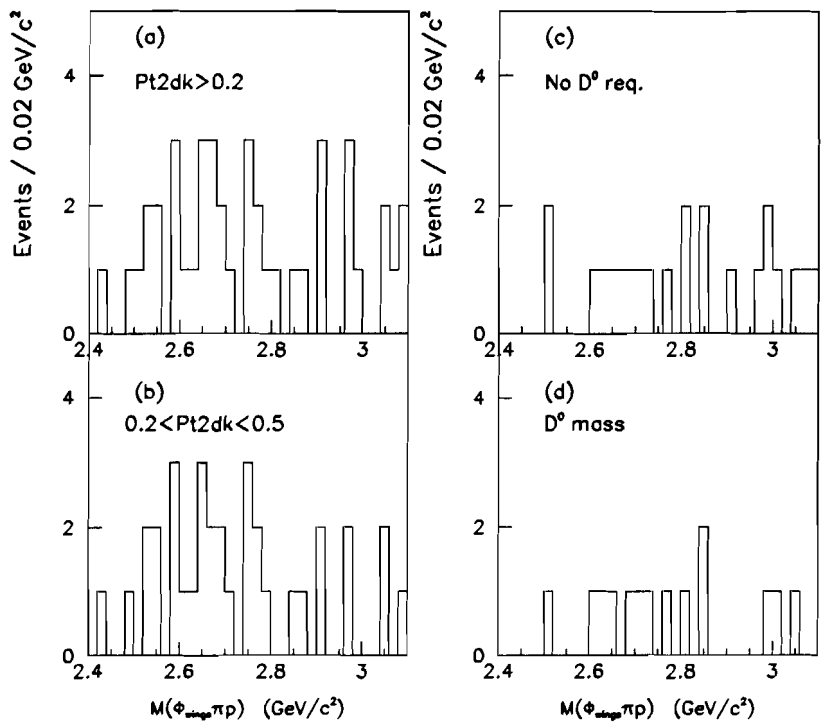

Figure 7.4: (a) The ($\phi_{wings}\pi p$) invariant mass distribution, plotted with the optimal cuts ("UL96") when the criterion on the Pt2dk is released. (b) The events rejected by the Pt2dk>0.5 cut. (c) The ($\phi_{wings}\pi p$) invariant mass distribution, plotted with the cuts of "UL96", but when the criterion "no $D^0 \to K\pi\pi\pi$ candidates" is not required. (d) The events rejected by the "no $D^0 \to K\pi\pi\pi$ candidates" cut.

Carlo and data by using the differences between their mean values. Then we calculated by how much these differences affected the ratio of efficiencies. In sections 7.2.1-7.2.4 I describe how it was done specifically for each of the variables. Some of the requirements, like the misidentification cuts, were applied only in the pentaquark analysis but not in the D_s analysis. Section 7.2.5 discusses the possible contribution of these requirements to the systematic uncertainty. Imperfect simulation of the production mechanism of the pentaquark could contribute also a systematic error. Section 7.2.6 discusses this contribution. Finally, Table 7.5 lists the evaluated systematic uncertainties and the total systematic error for each of the MC samples (with M($P^0_{\bar{c}s}$)=2.75 and 2.83 GeV/c^2).

7.2.1 Vertex definition variables

We compared distributions of variables defining 3- and 4-prong vertices. To compare between variables characterizing 3-prong vertices we used signals of the decay $D_s^{\pm} \to \phi\pi^{\pm} \to K^+K^-\pi^{\pm}$ from Monte Carlo and data. To compare between variables characterizing 4-prong vertices we used the pentaquark signal from Monte Carlo and the signal of the decay $D^0 \to K\pi\pi\pi$ from data. An example can be seen in Fig. 7.5, which shows the χ^2_{sec} distributions plotted for these signals, with all vertex definition cuts applied except for the cut on χ^2_{sec}.

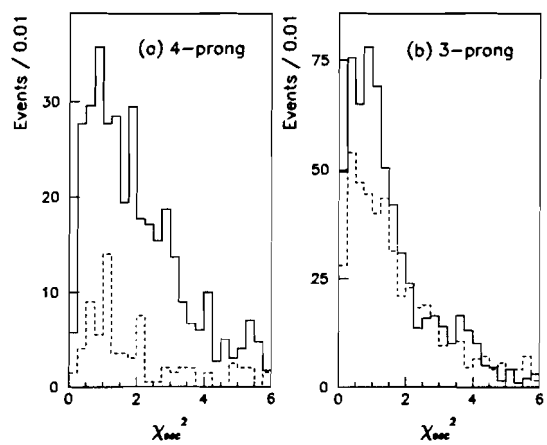

Figure 7.5: Distributions of χ^2_{sec} for 4- and 3-prong decays ((a) and (b), respectively). The solid and dashed lines in (a) represent the distributions from pentaquark MC and D^0 signal from data, respectively. The solid and dashed lines in (b) represent the distributions for D_s signals from MC and data, respectively.

The mean value of the χ^2_{sec} distribution plotted for pentaquark MC signal (2.01) differs from the one for the D^0 signal from data (1.98) by +0.03. The mean value of the χ^2_{sec} distribution for the D_s MC signal (1.50) differs from the one for D_s signal from data (1.71) by -0.21. These differences show that the χ^2_{sec} distribution for simulated pentaquarks is slightly wider than the one from D^0 from data, and that the χ^2_{sec} distribution for simulated D_s s is narrower than the one from data. The meaning is that a certain cut value applied to χ^2_{sec}, when calculated for 4-prong vertices, rejects somewhat more events in Monte Carlo than in data. Thus, the efficiency of this cut is smaller than it should be. The opposite is true for the D_s, where the efficiency is larger than it should be since the χ^2_{sec} distribution from Monte Carlo is narrower than the one from data.

Using the pentaquark and D_s signals from MC we calculated the ratio of efficiencies for the selection criteria in the "UL96" set (R_0). We then calculated the ratio of efficiencies again with cuts which differ from the cuts in "UL96" by the difference seen between the mean values of the variable distributions (R_1). In the example of χ^2_{sec} we calculated R_0 for the cut $\chi^2_{sec} < 3$, and for R_1 we varied the cut by +0.03 and

by -0.21 when we calculated its efficiency using pentaquark and D_s MC, respectively:

$$R_0 = \frac{\varepsilon_{P^0}}{\varepsilon_{D_s}}\Big|_{\chi^2_{sec}<3} \quad ; \quad R_1 = \frac{\varepsilon_{P^0}\,|_{\chi^2_{sec}<3.03}}{\varepsilon_{D_s}\,|_{\chi^2_{sec}<2.79}} \tag{7.1}$$

The systematic uncertainty for the cut $\chi^2_{sec} < 3$ was then defined as:

$$\sigma_{sys}(\chi^2_{sec}) = \frac{|R_1 - R_0|}{R_0} \tag{7.2}$$

The systematic uncertainty was calculated in the same way for all vertex definition variables, including: χ^2_{pri}, DIP, RAT, ISO, $RAT_i/AVGR$ and $MAXRAT_i$. The systematic uncertainty for the SDZ and $SIGMA$ variables was calculated using the same procedure but by modifying the cut value on SDZ and $SIGMA$ by ± 1 since these parameters were already given in units of errors on the reconstructed vertex locations.

7.2.2 Kinematical variable - the Pt2dk

The systematic uncertainty of the cut on the Pt2dk parameter was evaluated using the same method. However, since the Pt2dk is a kinematical variable and its distribution from the pentaquark decay is not similar to that from the D^0 decay, we compared between Pt2dk distributions characterizing D^0 signals from data and MC. It allowed a check of how well the Monte Carlo simulated the Pt2dk parameter for a decay which included more than two emerging particles (not like that of the D_s). The difference in the mean values of the Pt2dk distributions from D^0 Monte Carlo and data was observed to be +0.1. There was no difference seen between the Pt2dk distributions from D_s signals from Monte Carlo and data.

7.2.3 Particle identification cuts

The systematic uncertainties of the particle identification cuts were calculated using the following method:

<u>KID</u>

The KID selection criteria include a requirement that the momenta of the two kaon candidate tracks would be between 6 and 40 GeV/c, that their Čerenkov probabilities would be above 0.2 and that the product of these probabilities would be above 0.05. We applied the momentum cuts and the cuts on the product of Čerenkov probabilities, together with the ϕ window mass cut of ± 5 MeV/c^2, and calculated the ratio of efficiencies for different cut values on C($K1, K2$), from C($K1, K2$)>0.15 to C($K1, K2$)>0.4. Table 7.4 lists the changes in the ratio of efficiencies for the different cut values, relative to the original ratio. since the ratio of efficiencies is quite stable in the vicinity of the cut in use (>0.2), the most conservative estimate of the systematic uncertainty would be in this case: $\sim 3.5\%$.

Cut: C($K1, K2$) >	$(R_1 - R_0)/R_0$
0.15	+ 2.9%
0.16	+ 2.3%
0.17	+ 2.3%
0.18	- 0.2%
0.19	+ 2.5%
0.2	0% (original cut)
0.4	+ 3.5%

Table 7.4: Cut values applied to C($K1, K2$) together with the difference between the ratio $R_1 = \frac{\epsilon_{P^0}}{\epsilon_{D_s}}$ and the value of this ratio for the optimal cut value: C($K1, K2$) > 0.2 (R_0).

π ID

The π identification cut of "UL96" is: C(π) > 0.78. It rejects all tracks below the a priori peak on the C(π) scale. Since the value of 0.78 is very close to the a priori peak, the systematic uncertainty of this cut has been estimated in two ways:

1. The cut value was changed to a looser cut on C(π) and the change in the ratio of efficiencies was calculated. The resulting systematic uncertainty is listed in Table 7.5.

2. In order to check how sensitive would the result be to a more drastic change in the cut on C(π), the expression in Eq. 5.1 was calculated using two cut values: C(π)>0.78 and C(π)>0.815 (above the a priori peak). The number used for $N(P^0_{\bar{c}s} \rightarrow \phi\pi p)$ was the number of ($\phi\pi p$) events in the background region, outside 2.75 to 2.91 GeV/c^2 on the invariant mass scale. The change in the two expressions was of $\sim$ 1%. We concluded that even a drastic change in the cut on C(π) would not change the final result by more than $\sim$ 1%.

pID

The optimal cuts of the "UL96" set do not include a requirement on the Čerenkov probability of the proton track, or its momentum, other than the requirement in the analyser. We therefore did not include any systematic uncertainty due to this cut.

7.2.4 DIP(ϕ)

Evaluating the systematic uncertainty for the DIP(ϕ) cut was more problematic. We could compare the DIP(ϕ) distributions from signals of D_s from Monte Carlo and data, but we could not compare the DIP(ϕ) distribution from the Monte Carlo signal of pentaquarks to any other distribution from data. We assumed that the difference between DIP(ϕ) distributions from signals of D_s from Monte Carlo and data characterized also the difference between Monte Carlo and data of the pentaquark decay.

7.2.5 The effect of General cleaning and Misidentification cuts

The "no $D^0 \to K\pi\pi\pi$ candidates" and "no $\Lambda \to \pi p$ candidates" requirements reject events only from Monte Carlo samples of the pentaquark, and not from that of D_s. In order to check what could be the maximal error in the efficiency calculated for these cuts, we calculated their reduction factors relative to the efficiency of all other cuts when applied together. Using the same method we calculated the reduction factors of the "no ghost tracks" and "no secondary interaction" requirements, both from the pentaquark and D_s Monte Carlo samples. These reduction factors are listed as part of Table 7.5.

To evaluate the systematic uncertainty due to the "no mirror gap" we compared the reduction factors calculated from MC and data, both in the D_s and pentaquark analyses. The reduction factors calculated using D_s signal events from MC and data were equal: 0.95 ± 0.01. For estimating the reduction factor from $\phi\pi p$ data we used the Y-slope histograms of the $2K$ and p candidates (see sec. 5.6.3 and Fig. 5.13). We interpolated the number of kaons and protons that were rejected by the cut from the distributions outside the cut (gap) region, and divided these numbers by the total number of events in the Y-slope histograms. Since the three reduction factors (for the two kaons and the proton) were not correlated they were multiplied to give the total reduction factor of the "no mirror gap" cut. The reduction factor from the pentaquark MC was calculated in the same manner as described above for other cuts. Again, the comparison between the reduction factors calculated using $\phi\pi p$ data or the pentaquark MC gave the same result: 0.87 ± 0.02 and 0.87 ± 0.03 from data and Monte Carlo, respectively. We concluded that since the same reduction factors were calculated from Monte Carlo and data, both in the D_s and pentaquark analyses, this cut would not contribute to the systematic uncertainty of the result.

7.2.6 The effect of erroneous production characteristics

In section 4.2.1 we showed that the x_F distribution characterizing the production of D_s was simulated well by the MC. As the production mechanism of the pentaquark was unknown we assumed that its characteristics were similar to those of other charm particles. Originally, the simulation produced a Ξ_c, which was later given the features of the pentaquark (see sec. 4.1). The x_F distribution characterizing the production of Ξ_c was not necessarily exactly the same distribution we should expect for the pentaquark. In sec. 4.2.1 we fit the x_F distribution to $\mathcal{F}(x_F) = A_0(1 - x_F)^{n_0}$. Since this distribution could be erroneous for the pentaquark we checked by how much a change of ± 1 in n_0 (an error of $\sim 20\%$ in n_0) could affect the pentaquark search results. For that purpose we adopted the procedure used to define the efficiency dependence upon the unknown pentaquark lifetime, that is described in detail in sec. 8.2.2.

First, the acceptance of the pentaquark analysis was calculated as a function of x_F. It was the ratio between the x_F distributions with the cuts of "UL96" applied and at production (without any cuts):

$$Acc(x_F) = \frac{x_F \ dist. \ after \ cuts}{x_F \ dist. \ at \ production}. \tag{7.3}$$

For the bin i in the x_F distribution after cuts it should be true that:

$$[Acc(x_F) \cdot \mathcal{F}(x_F)\ ]\ |_i = N_i, \tag{7.4}$$

where N_i is the number of events in that bin. After summing over all bins we could define an acceptance function that depends on n, the parameter of production:

$$ACC(n) \equiv \frac{\sum_{bins}[\ Acc(x_F) \cdot A'(1 - x_F)^n\ ]}{\sum_{bins} N_i}, \tag{7.5}$$

where $ACC(n_0) \sim 1$. The coefficient A' was adjusted such that the number of generated events was not changed. The efficiency dependence upon n was calculated using the expression:

$$\varepsilon_n = \frac{ACC(n)}{ACC(n_0)} \cdot \varepsilon_{n_0} \tag{7.6}$$

A conservative change of ± 1 in n_0 resulted in a change of approximately $\pm 10\%$ in the efficiency. Hence, we estimated the systematic uncertainty due to erroneous production by 10%.

7.2.7 Summary

Table 7.5 summarizes the systematic uncertainties, which appear with + or − signs, indicating whether the error in the simulation of data is suspected to enlarge the final result or to reduce it, respectively. We assumed that the variables were not correlated and added the systematic uncertainties quadratically. The resulted total systematic errors for the two pentaquark masses, including the uncertainty due to the error in the parameter of production, n, are listed also in Table 7.5.

The bottom lines of Table 7.5 list the maximum effect on the ratio of efficiencies, which could be contributed from the "no D^0 or Λ candidates", "no ghost tracks" and "no secondary interaction" requirements. The largest contribution is expected from the "no D^0 candidates" requirement. However, since it is a kinematical effect and we have proved that the Monte Carlo has simulated well the kinematics (sec. 4.2.2), we decide not to include it in the evaluation of systematic uncertainty. The maximal contributions from the other requirements are small.

Variable	$(R_1 - R_0)/R_0$	
	$M(P^0_{\bar{c}s}) = 2.75$ GeV/c^2	$M(P^0_{\bar{c}s}) = 2.83$ GeV/c^2
SIGMA	+1.2%	+2.%
SDZ	−1.4%	+4.4%
ISO	+4.3%	+5.5%
DIP	+3.9%	+4.2%
RAT	+4.5%	+5.5%
RAT_i/AVGR	−0.7%	+2.7%
χ^2_{pri}	+6.3%	+2.9%
χ^2_{sec}	−2.4%	−2.7%
$MAXRAT_i$	+2.4%	+2.2%
KID	+5%	+4.5%
$C(\pi)$	+1.2%	−0.9%
Pt2dk	+1.2%	+1.3%
$DIP(\phi)$	−3.%	−0.5%
$\sqrt{\Sigma\sigma^2_{sys}(param)}$	11.8%	12.2%
$n \pm 1$	10%	10%
Total systematic uncertainty	15.5%	15.8%
No secondary interactions	1.3%	1.2%
No ghost tracks	0%	0%
No $D^0 \to K\pi\pi\pi$ or $\Lambda \to \pi p$ candidates	13%	7.2%
No $\Lambda \to \pi p$ candidates	0.7%	0.6%

Table 7.5: Systematic uncertainties in the ratio of pentaquark and D_s efficiencies. The total systematic uncertainty is taken as the square root of the quadratic sum of these contributions. The maximal possible systematic effects expected due to the general cleaning and misidentification cuts are listed in the lower part of the table.

Chapter 8

Results and Conclusions

8.1 Final spectra of $\phi\pi p$ and $\phi\pi$

The optimal analysis cuts are listed in table 5.3, with the title "UL96" cuts. Their selection procedure is described in detail in chapters 5 and 6. In Fig. 8.1(a), we show the final $\phi\pi p$ invariant mass spectrum for the optimal analysis cuts. The three events which could be described as $(D_s^{\pm}, D^{\pm} \rightarrow \phi\pi^{\pm}) + p$ are shaded. In Fig. 8.1(b), we show the $\phi_{wings}\pi p$ invariant mass spectrum where ϕ_{wings} refers to K^+K^- candidates with invariant mass in a range outside the required ϕ mass window (between 5 and 10 MeV/c^2 below and above the ϕ mass, see Fig. 5.7). This spectrum contains almost only non-ϕ background events.

The $\phi\pi p$ invariant mass spectrum (Fig. 8.1(a)) shows a concentration of seven events near 2.86 GeV/c^2 which is absent in the background spectrum of Fig. 8.1(b). The flat shape of this spectrum indicates that the selection criteria did not create an artificial peak (see also sec. 7.1). We estimate the probability that the group of events near 2.86 GeV/c^2 consists of background events. The binomial probability to have 7 or more events out of 24 grouped in any 40 MeV/c^2 (4 bins) out of 700 MeV/c^2 (70 bins) is:

$$\sum_{i>7}^{24} \binom{24}{i} \cdot \left(\frac{4}{70}\right)^i \cdot 66 \;=\; 0.05 \tag{8.1}$$

where $\binom{24}{i}$ is the number of possibilities to choose i events out of 24, $\left(\frac{4}{70}\right)^i$ is the probability to put the i events in one specific group of four bins, and 66 is the number of possibilities to have 4 adjacent bins in a histogram defined with 70 bins. The 5% probability is reduced to $\sim$ 1% if the four bins must be within the mass region of 2.75 to 2.91 GeV/c^2 - the region in which the pentaquark is predicted to exist. Figures 8.1(a),(b) show events with masses only above 2.5 GeV/c^2. For completeness I calculate also the probability to have the same group of events in a narrower mass region, between 2.5 to 3.1 GeV/c^2. This probability is $\sim$ 13% and reduces to $\sim$ 3.5% in the mass region of 2.75 to 2.91 GeV/c^2.

The optimal selection criteria include a quite loose proton identification criterion. It excludes more than 35% of pions, while accepting more than 90% of protons and kaons. As a result, the $KK\pi p$ invariant mass spectrum in Fig. 8.1(a) can be contam-

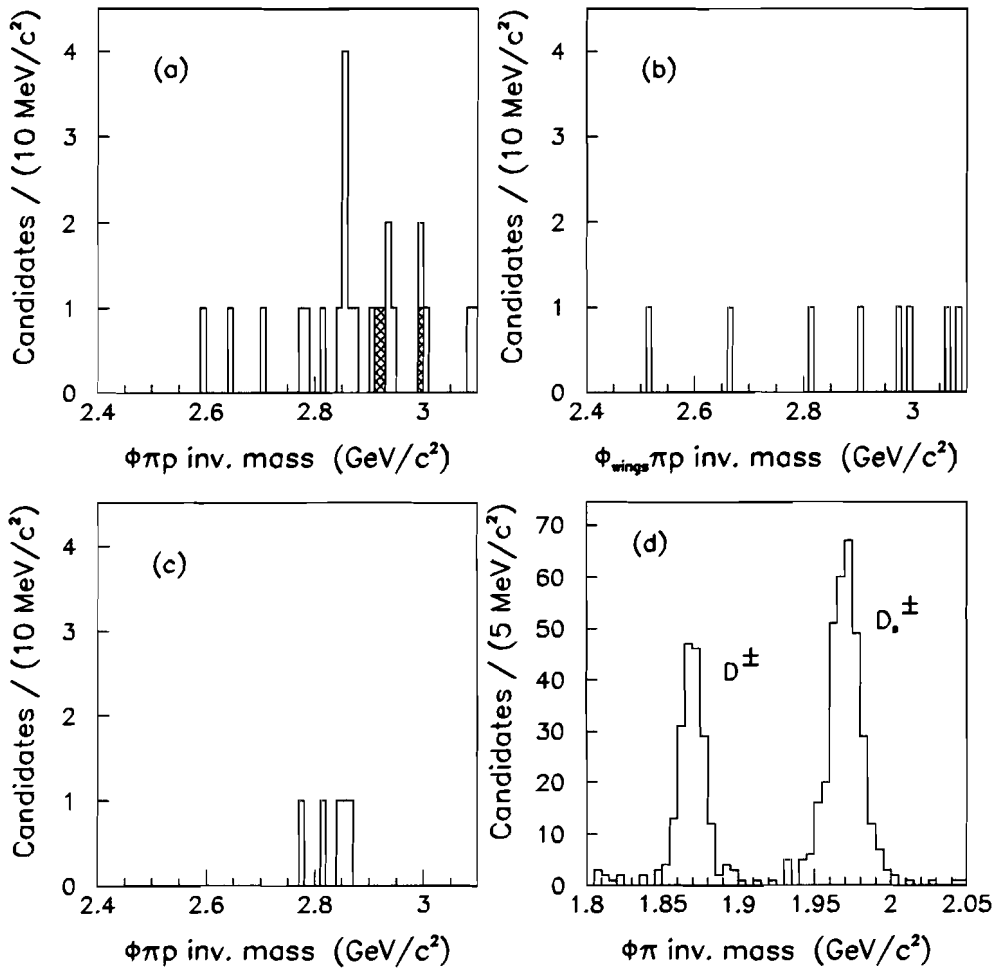

Figure 8.1: (a) The $\phi\pi p$ invariant mass spectrum from the E791 data for the optimized selection criteria. Events in which the $\phi\pi$ invariant mass is consistent with the $D^{\pm}$ or $D_s^{\pm}$ masses are shaded. (b) Spectrum of $\phi_{wings}\pi p$ for the optimized selection criteria; see text for a full description. (c) The same spectrum as in (a), with a tighter proton identification criterion. (d) $\phi\pi$ invariant mass spectrum for the $D_s^{\pm}$ normalization sample. The left peak arises from Cabibbo-suppressed $D^{\pm}$ decays.

inated with combinations of four tracks that include a kaon or a pion instead of the assumed proton track. In Fig. 8.1(c), we show the $\phi\pi p$ invariant mass spectrum with a tighter cut on the proton Čerenkov probability, together with a requirement that the track momentum be between 22 and 75 GeV/c (the pID cut of "set 2", see sec. 5.4.2). This selection criterion excludes 95% of pions and more than 80% of kaons. It gives essentially the same sensitivity for a pentaquark signal but with half the efficiency (see Table 7.1). Because of the very low efficiency of this tighter criterion we did not choose it as the optimal proton ID cut. If applied, three of the seven events that are grouped near 2.86 GeV/c^2 (Fig. 8.1(a)) survive the tighter proton Čerenkov selection criterion (Fig. 8.1(c)), consistent with the expected efficiency of this criterion. Only two out of the 17 events outside the concentration survive this requirement. Thus, we conclude that there are more protons in the group of events near 2.86 GeV/c^2 than elsewhere on the invariant mass scale.

However, because the number of events in our final sample is so small, we can not conclude that there is a convincing evidence for $P^0_{\bar{c}s} \to \phi\pi p$ decays in our data.

In Fig. 8.1(d), we show the $\phi\pi$ invariant mass spectrum for the $D_s^\pm \to \phi\pi^\pm$ normalization sample. This sample was selected using the same selection criteria (where relevant) as were used to select pentaquark candidates. In this manner the systematic error on the ratio of efficiencies for the two decay modes was minimized.

8.2 Results

8.2.1 A mass dependent upper-limit for the decay $P^0_{\bar{c}s} \to \phi\pi p$

We use the spectrum of Fig. 8.1(a) to obtain 90% C.L. upper-limits on the product of the pentaquark production cross section and the pentaquark branching fraction to $\phi\pi p$, relative to that for $D_s^\pm \to \phi\pi^\pm$. For a particular $\phi\pi p$ invariant mass, our limit is:

$$UL\left(\frac{\sigma_P \cdot B_{P\to\phi\pi p}}{\sigma_{D_s} \cdot B_{D_s\to\phi\pi}}\right) = \frac{UL(N_{P\to\phi\pi p})/\varepsilon_{P\to\phi\pi p}}{N_{D_s\to\phi\pi}/\varepsilon_{D_s\to\phi\pi}}, \tag{8.2}$$

where $UL(N_{P\to\phi\pi p})$ is the 90% C.L. upper-limit on the number of signal events in a mass window centered on the invariant mass of interest, given the number of events observed in the window and the expected number of background events [38]. The quantity $N_{D_s\to\phi\pi}$ is the number of $D_s^\pm \to \phi\pi^\pm$ decays obtained from the normalization sample (Fig. 8.1(d)), and the quantities $\varepsilon_{P\to\phi\pi p}$ and $\varepsilon_{D_s\to\phi\pi}$ are the detection efficiencies for $P^0_{\bar{c}s} \to \phi\pi p$ and $D_s^\pm \to \phi\pi^\pm$, respectively. These efficiencies were calculated using Monte Carlo simulations (sec. 7.1). The background spectrum — for lack of more information — is assumed to be flat as indicated by Fig. 8.1(b). The level of background expected is obtained from Fig. 8.1(a) by matching the flat spectrum to the number of events between 2.4 and 3.1 GeV/c^2, excluding the shaded events.

We present limits for four pentaquark masses in the range between 2.75 GeV/c^2 and 2.91 GeV/c^2, where the pentaquark is predicted to exist. We consider mass windows of width 40 MeV/c^2 which, based on the experimental resolution, should contain more than 90% of true signal events. Since we produced only pentaquarks with

M($P^0_{\bar{c}s}$)=2.75 or 2.83 GeV/c^2, we used the efficiencies calculated for them to extract the efficiencies for pentaquarks with other masses. Table 8.1 lists the numbers used in Eq. 8.2 and the resulting upper-limits. These limits include a correction factor f_{SYS} to account for systematic uncertainties [42]:

$$UL' = UL \cdot f_{SYS}. \tag{8.3}$$

Here, UL is the values resulting from Eq. 8.2, and UL' is the corrected upper-limits. The correction f_{SYS} includes the measured upper-limit and its statistical and systematic errors:

$$f_{SYS} = 1 + (UL - n) \cdot \frac{\sigma^2}{2}, \tag{8.4}$$

where n is the number of events above the background level, and σ^2 is the relative error of the measurement, which incorporates the relative statistical and systematic errors: $\sigma^2 = \sigma^2_{stat} + \sigma^2_{sys}$.

M($P^0_{\bar{c}s}$) GeV/c^2	2.75	2.79	2.83	2.87
$UL(N_{P\to\phi\pi p})$	2.3	4.3	4.3	9.3
$\varepsilon_{P\to\phi\pi p}/\varepsilon_{D_s\to\phi\pi}$	0.38	0.5	0.62	0.74
$N_{D_s\to\phi\pi}$	293±18			
σ	22%	20%	19%	18%
f_{SYS}	1.05	1.07	1.07	1.08
90% C.L. upper-limit	0.022	0.032	0.025	0.046

Table 8.1: Values of $UL(N_{P\to\phi\pi p})$, ratio of efficiencies for $P \to \phi\pi p$ and $D_s \to \phi\pi$, and $N_{D_s\to\phi\pi}$ used to calculate the upper-limit on the ratio of cross section times branching fraction for the decays $P^0 \to \phi\pi p$ and $D_s^\pm \to \phi\pi^\pm$, as defined in Eq. 8.2. The relative error σ and the correction factor f_{SYS} are listed too. Four values of pentaquark mass are used. The pentaquark lifetime used to calculate efficiencies is 0.4 ps.

Assuming that the branching fractions of the $D_s^\pm \to \phi\pi^\pm$ and $P^0_{\bar{c}s} \to \phi\pi p$ decays are similar, the resulting upper-limits approach the range of the estimated ratio between the pentaquark and $D_s^\pm$ production cross sections.

8.2.2 Upper-limit dependence on the pentaquark lifetime

The value of the upper-limit depends upon the pentaquark lifetime due to dependence of the efficiency on lifetime. To get the efficiency dependence upon pentaquark lifetime I developed the following procedure:

- The decay time of pentaquarks was defined as:

$$Decay\ time = \frac{(Z_{sec} - Z_{pri}) \cdot M(P^0_{\bar{c}s})}{MOM(P^0_{\bar{c}s}) \cdot 3 \times 10^{-2}}, \tag{8.5}$$

  Where Z_{pri} and Z_{sec} are the Z positions of the pentaquark production and decay vertices, respectively, $M(P^0_{\bar{c}s})$ and $MOM(P^0_{\bar{c}s})$ are its mass and momentum, and 3×10^{-2} is the velocity of light in cm/ps. The decay time was calculated from the Monte Carlo simulations and was plotted in two distributions:

1. For all pentaquarks produced in the production stage, before any cuts were applied.
2. For pentaquark accepted events, with the optimal cuts applied.

These two distributions are shown in Fig. 8.2 for pentaquarks simulated with M($P^0_{\bar{c}s}$)=2.83 GeV/c^2. The ratio between them is the acceptance of the pentaquark analysis as a function of decay time:

$$Acc(t) = \frac{decay\ time\ dist.\ after\ cuts}{decay\ time\ dist.\ at\ production} \tag{8.6}$$

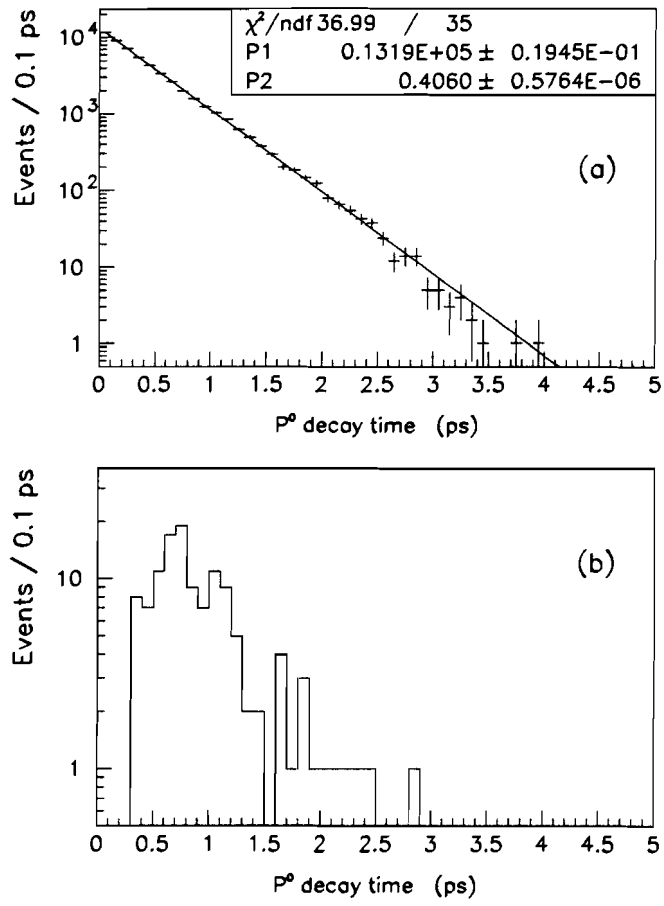

Figure 8.2: (a) Decay time distribution of all simulated pentaquarks with M($P^0_{\bar{c}s}$)=2.83 GeV/c^2. The solid line is the function fitted to the distribution: $\mathcal{F}(t) = C_0 \cdot e^{-t/\tau_0}$. The fitted parameters, C_0 (P1) and τ_0 (P2), and the χ^2 of the fit are listed in the top right corner of the histogram. (b) Decay time distribution of pentaquarks with M($P^0_{\bar{c}s}$)=2.83 GeV/c^2, plotted with the final cuts ("UL96").

- The decay time distribution at production was fitted to the function:

$$\mathcal{F}(t) = C_0 \cdot e^{-t/\tau_0}, \tag{8.7}$$

where C_0 is the function value at $t = 0.0$ ps, and τ_0 is the fitted lifetime. The resulted function, $\mathcal{F}(t)$, is shown in Fig. 8.2(a). The fit parameters are listed in its top right corner. It can be seen that $\tau_0 = 0.4$ ps, the value that was defined in the simulation.

- For a bin i in the decay time distribution of Fig. 8.2(b) it should be true that:

$$[Acc(t) \cdot \mathcal{F}(t)\ ]\ |_i = N_i, \tag{8.8}$$

where N_i is the number of events in that bin. The equation is valid also if we sum over all bins. We defined an acceptance function which depends on the lifetime (τ):

$$ACC(\tau) \equiv \frac{\sum_{bins}[\ Acc(t) \cdot C' e^{-t/\tau}\ ]}{\sum_{bins} N_i}, \tag{8.9}$$

where $ACC(\tau_0) \sim 1$. The coefficient C' is adjusted such that the integral of the function, representing the number of produced events, is fixed (100,000 events): $C' = C_0 \cdot \frac{\tau_0}{\tau}$. The efficiency dependence upon pentaquark lifetime was calculated using the expression:

$$\varepsilon_\tau = \frac{ACC(\tau)}{ACC(\tau_0)} \cdot \varepsilon_{\tau_0} = \frac{\sum_{bins}[\ Acc(t) \cdot C' e^{-t/\tau}\ ]}{\sum_{bins}[\ Acc(t) \cdot C_0 e^{-t/\tau_0}\ ]} \cdot \varepsilon_{\tau_0} \tag{8.10}$$

Fig. 8.3(a) shows ε_τ as a function of the varying lifetime τ of pentaquarks simulated with two masses: 2.75 and 2.83 GeV/c^2. It can be seen that the efficiency is very small for small values of τ, meaning that the detector acceptance or pentaquark analysis (or both) are not sensitive for pentaquarks with short lifetimes.

The upper-limit values are inversely proportional to the efficiency. Fig. 8.3(b) shows the dependence of the upper-limit value on the pentaquark lifetime, calculated for pentaquarks simulated with $M(P^0_{\bar{c}s}) = 2.75$ and 2.83 GeV/c^2. It can be seen that for the two masses the upper-limit is a rapidly decreasing function of lifetime, from an upper-limit close to 1 for 0.1 ps, to the values listed in Table 8.1 for 0.4 ps, and remaining about the same for larger lifetime values. The similarity between these functions indicates that their shape is mass independent.

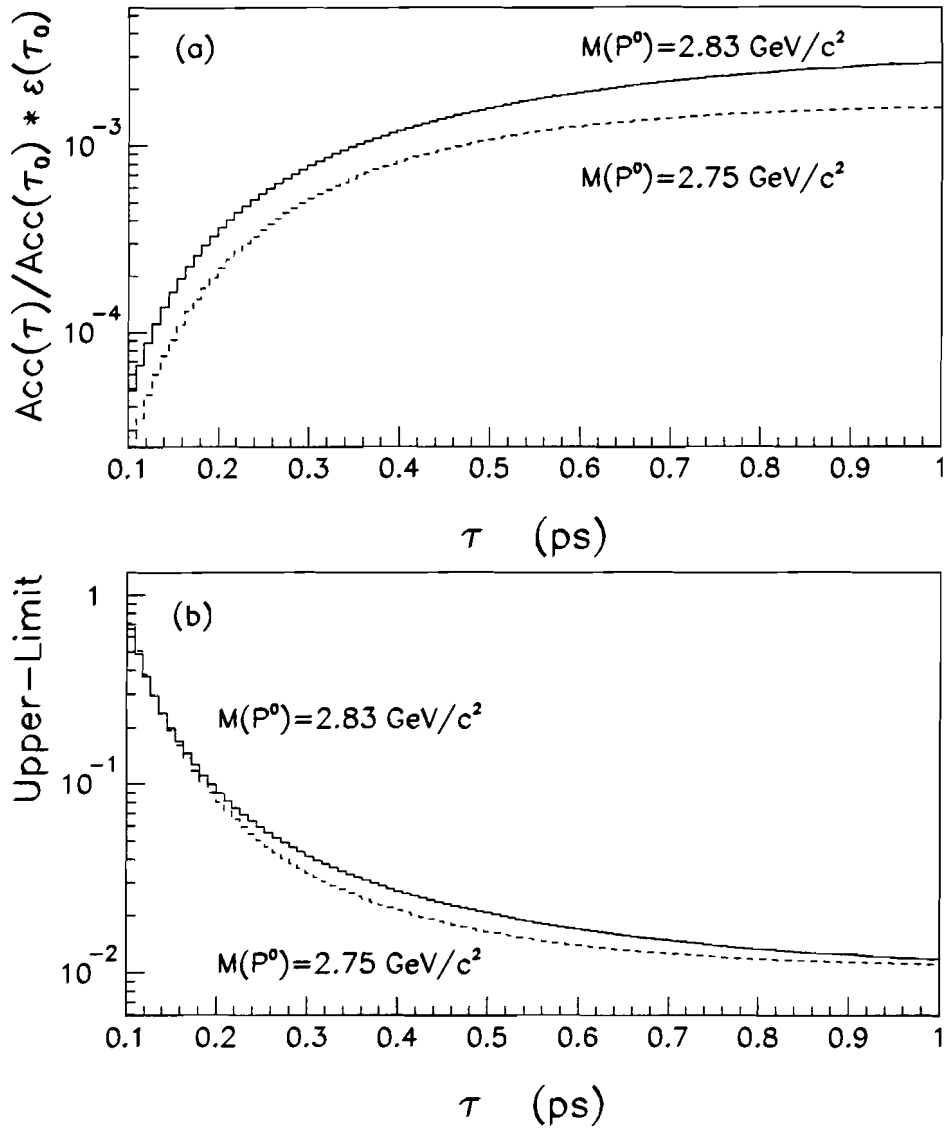

Figure 8.3: (a) The acceptance as a function of the pentaquark simulated lifetime. (b) The resulted upper-limit dependence upon pentaquark lifetime. The solid and dashed lines refer to a pentaquark mass of 2.83 and 2.75 GeV/c^2, respectively.

8.3 Summary

This thesis presents results of the first search for the pentaquark particle. We searched for the pentaquark via its expected decay to $\phi\pi p$ and normalized the analysis to the similar decay $D_s \rightarrow \phi\pi$.

We reached the goal of being sensitive to a few percent of the D_s production cross section. This was the desired sensitivity as the various predictions of the pentaquark production were made relative to the D_s and the estimated ratio between them was of the order of 1% (sec. 1.4).

However, only 24 events were selected by the optimal analysis cuts (Fig. 8.1(a)), and only 5 survived the proton ID requirement. Due to the low statistics in the final spectra we do not have a convincing evidence for pentaquarks decaying to $\phi\pi p$ in Fermilab E791 data.

Upper-limits are presented for the ratio of $\sigma \cdot B$ for $P^0_{\bar{c}s} \rightarrow \phi\pi p$ and $D_s^{\pm} \rightarrow \phi\pi^{\pm}$ for four different values of pentaquark mass, in the range 2.75-2.91 GeV/c^2. The upper-limits are approaching the theoretically estimated ratio of production cross-sections if we assume the same branching fraction for the two decays and a pentaquark lifetime of 0.4 ps or greater. For lifetimes short compared to 0.4 ps the poorer efficiency of the detector results in larger upper limits. Consequently, our results also do not rule out the existence of the pentaquark.

This work provides a good starting point for future experimental searches in the frame work of high statistics charm experiments.

Bibliography

[1] An introduction to Quarks and Partons/ F.E. Close, Academic Press.

[2] R.L. Jaffe Phys. Rev. Lett. **38**, 195 (1977).

[3] J. Belz *et al.*, Phys. Rev. Lett. **76**, 3277 (1996);
R.W. Stotzer *et al.*, Phys. Rev. Lett. **78**, 3646 (1997);
D. Ashery, Proceedings of the Hadron '97 conference, BNL (1997), and references therein.

[4] H.J. Lipkin, Proceedings of the *XXIInd* Rencontre de Moriond, France, J. Tran Thanh Van *ed.* , Editions Frontieres (1987), p. 691.;
H.J. Lipkin, Phys. Lett. **B195**, 484 (1987).

[5] C. Gignoux *et al.*, Phys. Lett. **B193**, 323 (1987).

[6] S. Fleck *et al.*, Phys. Lett. **B220**, 616 (1989).

[7] S. Zouzou and J.M. Richard, *Few-Body Systems* **16**, 1 (1994).

[8] S. Takeuchi, S. Nussinov, and K. Kubodera, Phys. Lett. **B318**, 1 (1993).

[9] D.O. Riska and N.N. Scoccola, Phys. Lett. **B299**, 338 (1993);
Y. Oh *et al.*, Phys. Rev. **D50**, 3350 (1994);
Y. Oh *et al.*, Phys. Lett. **B331**, 362 (1994).

[10] C.K. Chow, Phys. Rev. **D51**, 6327 (1995);
C.K. Chow, Phys. Rev. **D53**, 5108 (1996).

[11] Quarks and Leptons/ F. Halzen, A.d. Martin, John Wiley & Sons.

[12] B. Quinn *et al.*, Proceedings of Baryon 92 Int. Conf., Yale University, M Gai *ed.*, World Scientific (1992), p. 278.

[13] Models of the Nucleon/ R.K. Bhaduri, Addison-Wesley publishing Company, and references therein.

[14] H.J. Lipkin, private communication.

[15] Particle Data Group, Phys. Rev. **D54**, 31 (1996).

[16] H.J. Lipkin, Nucl. Phys. **B21**, 258 (1991).

[17] D. Ashery, Hyperfine Interactions **103**, 253 (1996).

[18] M. A. Moinester, D. Ashery, L. G. Landsberg, and H. J. Lipkin, Z. Phys. **A356**, 207 (1996), and references therein.

[19] S. MayTal-Beck *et al.*, Proc. of the 8th Meeting, Div. of Particles and Fields of the Am. Phys. Soc., S. Seidel *ed.*, World Scientific (1994), p. 1177.

[20] J.I. Kapusta, Phys. Rev. **C21**, 1301 (1980);
C.B. Dover *et al*, Phys. Rev. **C44**, 1636 (1991).

[21] A. Casher, H. Neuberger and S. Nussinov, Phys. Rev. **D20**, 179 (1979).

[22] W. Bozzoli *et al.*, Nucl. Phys. **B144**, 317 (1978).

[23] J.L. Thron *et al.*, Phys. Rev. **31**, 451 (1985).

[24] Particle Data Group, Phys. Rev. **D54**, 473 (1996).

[25] T. Carter, E791 Offline Document Number 162, (1994).

[26] M. Purohit *et al.*, The Princeton Scanner / Controller Manual.

[27] K. Kodama *et al.* Nucl. Instr. and Meth. **A289**, 146 (1990).

[28] J.S. Wiener, Ph.D. thesis, Princeton University, unpublished (1994).

[29] J. Raab, Ph.D. thesis, UCSB, unpublished (1987).

[30] Introduction to experimental particle physics / R.C. Fernow, Cambridge university press.

[31] D. Bartlett *et al.*, Nucl. Instr. and Meth. **A260**, 55-75 (1987).

[32] V.K. Bharadwaj *et al.*, Nucl. Instr. and Meth. **228**, 283 (1984).

[33] J.A. Appel *et al.*, Nucl. Instr. and Meth. **A243**, 361 (1986).

[34] N.J. Witchey, Ph.D. thesis, Ohio State University, unpublished (1996).

[35] S. Amato *et al.*, Nucl. Inst. and Meth. **A324**, 535 (1993).

[36] T. Sjöstrand, Computer Physics Commun. **82**, 74 (1994).

[37] J.A. Appel, Ann. Rev. Nucl. Part. Sci. **42**, 367 (1992).

[38] Particle Data Group, Phys. Rev. **D54**, 166 (1996).

[39] G. Hurvits, E791 Offline Document Number 294, (1996).

[40] A. Albrecht *et al.*, Phys. Lett. **B317**, 227 (1993).

[41] Particle Data Group, Phys. Rev. **D54**, 56 (1996).

[42] R.D. Cousins and V.L. Highland, Nucl. Instr. and Meth. **A320**, 331 (1992).

תקציר

בעבודת מחקר זו מתואר החיפוש אחר הפנטקוורק, $P_{\bar{c}s}$, המורכב מחמישה קוורקים ויכול להופיע בשני מצבים: $P_{\bar{c}s}^{\,0} = |\bar{c}suud\rangle$ ו- $P_{\bar{c}s}^{\,0} = |\bar{c}sddu\rangle$. אינטראקצית ה- Color-Hyperfine בין הקוורקים מנבאת פוטנציאל קשר מקסימלי של 150 MeV עבור הפנטקוורק. מודלים אחרים מנבאים כי לפנטקוורק אנרגית קשר נמוכה או שהוא רזוננס ומאסתו קרובה לאנרגית הסף. אם הפנטקוורק הנו חלקיק קשור אזי מאסתו נמוכה מ - $2.907\ GeV/c^2$ וזמן החיים שלו הנו מסדר גודל של $10^{-13}\ s$. בשל המבנה יוצא הדופן של הפנטקוורק החיפוש אחריו חשוב ועשוי לעזור בהבנת QCD ותהליך ה- confinement של הקוורקים.

החיפוש אחר הפנטקוורק נערך במסגרת ניסוי E791 במעבדת המאיץ Fermilab. בניסוי זה הופצצו מטרות דקות של פלטינה ופחמן בקרן של π^- באנרגיה של $500\ GeV/c$. באינטראקציה נוצרו הדרונים ותוצרי התפרקותם נמדדו בעזרת ספקטרומטר שאפשר מדידה של צמתי יצירה והתפרקות בדיוק מאוד גבוה וכן אפשר זיהוי טוב של חלקיקים טעונים. במהלך הניסוי הוקלטו 2×10^{10} מאורעות ובמהלך אנליזה של כלל הניסיון זוהו 200,000 הדרונים המכילים את הקוורק הקסום (c).

אנו חיפשנו אחר תהליך ההתפרקות $P_{\bar{c}s}^{\,0} \to \phi\pi p$, כאשר ה- ϕ מתפרק ל K^+K^- ונרמלנו את רגישות תהליך החיפוש למדידת תהליך ההתפרקות הדומה $D_s \to \phi\pi$. הדמיון בין שני תהליכי ההתפרקות אפשר ביטול של שגיאות סיסטמתיות המשותפות להם. מספרם הרב של המאורעות שנאספו בניסוי אפשר לנו להגיע לדמת הרגישות שנדרשה לעבודת מחקר זו.

קריטריונים טופולוגיים, קינמטיים ואחרים הופעלו על מנת להוריד את רמת הרקע ולשפר רגישות סטטיסטית של סיגנל אפשרי של הפנטקוורק בספקטרום ה- $\phi\pi p$. לאחר הפעלת הקריטריונים האופטימליים נבחרו 24 מאורעות. המסה האינווריאנטית של $\phi\pi p$ ב- 11 מהם היתה בתחום של $2.75-2.91\ GeV/c^2$, התחום בו אפשרי קיום של הפנטקוורק. שבעה מתוך אחד עשר מאורעות אלה הנם מרוכזים סביב $2.86\ GeV/c^2$. עם זאת, מפני מיעוט מספר המאורעות בספקטרום הסופי, אנו מסיקים כי אין בידינו הוכחה חותכת לקיום הפנטקוורק בקרב הנתונים שנאספו. על כן אנו מציגים גבול עליון בדרגת מובהקות של 90% ליחס:

$$\frac{\sigma_P \cdot B_{P\to\phi\pi p}}{\sigma_{D_s} \cdot B_{D_s\to\phi\pi}}$$

כאשר σ הוא חתך הפעולה ליצירה ו- B הנו הסיכוי להתפרקות החלקיק הנוצר באופן ההתפרקות הרשום.

גבול עליון זה תלוי במסה. ערכיו הנם: 0.022, 0.032, 0.025 ו- 0.046 עבור ערכי מסה של: 2.75, 2.79, 2.83 ו- 2.87 GeV/c^2, בהתאמה, בהנחה שלפנטקוורק זמן חיים של 0.4 ps. ערכי הגבול העליון תלויים גם בזמן החיים של הפנטקוורק עקב תלותה של יעילות החיפוש בזמן החיים. עבור $M(P_{\bar{c}s}^{\,0}) = 2.83\ GeV/c^2$, תלות הגבול העליון בזמן החיים הנה פונקציה היורדת בתלילות מערך קרוב ל- 1 עבור זמן חיים של 0.1 ps לערך הנקוב למעלה עבור 0.4 ps, ונשארת כמעט ללא שינוי עבור זמני חיים ארוכים יותר.

לסיכום, ערכי הגבול העליון הנם מאותו סדר גודל של היחס הצפוי בין חתכי הפעולה ליצירת הפנטקוורק וה- D_s, בהנחה שלאופני ההתפרקות הדומים של שני החלקיקים אותו סיכוי, ובהנחה שזמן החיים של הפנטקוורק הנו לפחות 0.4 ps. עבודה זו מהווה נקודת מוצא טובה עבור חיפושים עתידיים אחר הפנטקוורק, בניסיונות שיאספו מספר רב יותר של חלקיקים קסומים.

חיפוש אחר הפנטקוורק בערוץ ההתפרקות

$$P_{\bar{c}s}^{0} \rightarrow \phi \pi p$$

חיבור לשם קבלת התואר "דוקטור לפילוסופיה"

מאת

שרון מי-טל בק

הוגש לסנאט של אוניברסיטת תל-אביב

דצמבר, 1997